



**UNIVERSIDADE ESTADUAL DE CAMPINAS**  
**Instituto de Geociências**

**LUCIANO POGGI**

**THE AU-CU-MO PARAÍBA DEPOSIT (MT): INTEGRATION OF SPECTRAL AND  
CONVENTIONAL TECHNIQUES FOR MINERAL EXPLORATION**

**O DEPÓSITO DE AU-CU-MO PARAÍBA (MT): INTEGRAÇÃO DE TÉCNICAS  
ESPECTRAIS E CONVENCIONAIS PARA A EXPLORAÇÃO MINERAL**

**CAMPINAS**

**2019**

**LUCIANO POGGI**

**THE AU-CU-MO PARAÍBA DEPOSIT (MT): INTEGRATION OF SPECTRAL AND  
CONVENTIONAL TECHNIQUES FOR MINERAL EXPLORATION**

**O DEPÓSITO DE AU-CU-MO PARAÍBA (MT): INTEGRAÇÃO DE TÉCNICAS  
ESPECTRAIS E CONVENCIONAIS PARA A EXPLORAÇÃO MINERAL**

DISSERTATION PRESENTED TO THE INSTITUTE OF  
GEOSCIENCES OF THE UNIVERSITY OF CAMPINAS TO  
OBTAIN THE DEGREE OF MASTER IN GEOSCIENCES  
IN THE AREA OF GEOLOGY AND NATURAL  
RESOURCES

DISSERTAÇÃO DE MESTRADO APRESENTADA AO  
INSTITUTO DE GEOCIÊNCIAS DA UNICAMP PARA  
OBTENÇÃO DO TÍTULO DE MESTRE EM  
GEOCIÊNCIAS NA ÁREA DE GEOCIÊNCIAS E  
RECURSOS NATURAIS

**ORIENTADOR: PROF. DR. DIEGO FERNANDO DUCART**

ESTE EXEMPLAR CORRESPONDE À VERSÃO FINAL  
DA DISSERTAÇÃO DEFENDIDA PELO ALUNO  
LUCIANO POGGI E ORIENTADA PELO PROFESSOR DR.  
DIEGO FERNANDO DUCART

CAMPINAS

2019

**Agência(s) de fomento e nº(s) de processo(s):** CAPES; FAPESP, 2016/04370-5

**ORCID:** <https://orcid.org/0000-0002-5857-1127>

Ficha catalográfica  
Universidade Estadual de Campinas  
Biblioteca do Instituto de Geociências  
Marta dos Santos - CRB 8/5892

P753d Poggi, Luciano, 1989-  
O depósito de Au-Cu-Mo Paraíba (MT) : integração de técnicas espectrais e convencionais para a exploração mineral / Luciano Poggi. – Campinas, SP : [s.n.], 2019.

Orientador: Diego Fernando Ducart.  
Dissertação (mestrado) – Universidade Estadual de Campinas, Instituto de Geociências.

1. Minérios - Alta Floresta (MT). 2. Alteração hidrotermal. 3. Mineralizações auríferas. 4. Espectroscopia de reflectância. I. Ducart, Diego Fernando, 1974-. II. Universidade Estadual de Campinas. Instituto de Geociências. III. Título.

#### Informações para Biblioteca Digital

**Título em outro idioma:** The Au-Cu-Mo Paraíba deposit (MT) : integration of spectral and conventional techniques for mineral exploration

**Palavras-chave em inglês:**

Ores - Alta Floresta (MT)

Hydrothermal alteration

Gold mineralization

Reflectance spectroscopy

**Área de concentração:** Geologia e Recursos Naturais

**Titulação:** Mestre em Geociências

**Banca examinadora:**

Diego Fernando Ducart [Orientador]

Carlos Roberto de Souza Filho

Rafael Rodrigues de Assis

**Data de defesa:** 14-02-2019

**Programa de Pós-Graduação:** Geociências



**UNIVERSIDADE ESTADUAL DE CAMPINAS  
INSTITUTO DE GEOCIÊNCIAS**

**AUTOR:** Luciano Poggi

**THE AU-CU-MO PARAÍBA DEPOSIT (MT): INTEGRATION OF SPECTRAL AND  
CONVENTIONAL TECHNIQUES FOR MINERAL EXPLORATION**

**O DEPÓSITO DE AU-CU-MO PARAÍBA (MT): INTEGRAÇÃO DE TÉCNICAS  
ESPECTRAIS E CONVENCIONAIS PARA A EXPLORAÇÃO MINERAL**

**ORIENTADOR:** Prof. Dr. Diego Fernando Ducart

Aprovado em: 14 / 02 / 2019

**EXAMINADORES:**

Prof. Dr. Prof. Dr. Diego Fernando Ducart – Presidente

Prof. Dr. Carlos Roberto de Souza Filho

Prof. Dr. Rafael Rodrigues de Assis

**A Ata de defesa com as respectivas assinaturas dos membros, encontra-se disponível no  
SIGA - Sistema de Fluxo de Dissertação e na Secretaria de Pós-graduação do IG.**

Campinas, 14 de fevereiro de 2019.

## BIOGRAPHY

**Luciano Poggi** was born in Río Cuarto, Córdoba, Argentina, in 1989. He received the bachelor degree in geology from the National University of Río Cuarto (UNRC), Córdoba, Argentina, in 2016 and a Master degree from the University of Campinas - UNICAMP, São Paulo, Brasil, in 2019. He has experience in geosciences, with emphasis on economic geology, geological mapping, topographic survey, resource estimation, reflectance spectroscopy, hyperspectral remote sensing, petrography and mineral chemistry. He works mainly with the characterization, description and zoning of hydrothermal alterations through the application of spectral techniques in Au-Cu-Mo deposits associated with deformed zones and felsic intrusive rocks.

He carried out scientific initiation (2014-2015) and his bachelor degree (2016) in an industrial-bearing minerals deposit (quartz, feldspar, micas and beryl) located in San Luis province, Argentina. During the scientific initiation, he made a topographic and structural analysis of the area, as well as detailed rocks petrography. During his bachelor degree, he added chemical analysis, designed a detailed map of the mine, resource estimation, design a work plan and finally estimated the mining project life. These results were complemented by an economic and financial analysis that considered the NPV, IRR and CR parameters. This project is part of the UNRC library and belongs to the company PIEDRA GRANDE Samica y F (internal reports - unpublished).

In the master's degree, he studied the Au ± Cu ± Mo Paraíba deposit, located in the Mato Grosso state, Brazil. He applied spectral techniques for mineral exploration as reflectance and imaging spectroscopy, in order to generate high-resolution hyperspectral images. Besides, he performed petrographic and mineral chemistry studies.

During this period, he also participated in the Teaching Internship Program (PED), performing as a monitor of the discipline "Remote Sensing and Photogeology" of the undergraduate geology course at the University of Campinas - UNICAMP. Concurrently, he published several abstracts at national and international congresses (Poggi and Ducart 2017 and Poggi et al. 2018).

## **ACKNOWLEDGMENTS**

First of all, I would like to thank my girlfriend Celeste! Who was with me from the beginning I started this adventure, with her support and unconditional love, even in the most difficult moments, bearing the distance that few people could get. She helped me every time I needed, laughed and suffered with me, and I would certainly not be here if it were not for her. To my life partner, thank you! I love you.

I thank my family, my grandparents, uncles, cousins and siblings for being a fundamental and indispensable part of my life. To my parents, who always supported me, trusted me and were present at all times. Without you, the path would have been harder to tread.

I want to especially thank Diego, Fernanda and their three children for receiving me, from the first day, in her house, in her heart and in her family. Thank you very much from the heart for making me feel like I was at home and for being present at all times.

Besides, I also thank Diego for believing in me, for helping me to grow professionally and as a person, and for the possibility of having worked together during these years, which I hope will not be the last.

To the geologist Andrés Navarro for the great help in the field tasks, by the numerous anecdotes and friendship.

To the examination board teachers, Rafael Assis, Carlos Roberto de Souza Filho and Saeid Asadzade for their excellent predisposition and professionalism at all times.

To Maria Jose, for his great help and accompaniment along these years. For your commitment, honesty and friendship. Thank you!

I would also like to thank Beto, Robertinho and Carol for the predisposition, help and confidence given over the years!

To my Brazilian brothers, Igor and Halina. Thank you very much from the heart for making me feel part of your life and for receiving me from the beginning with a smile in your beautiful country. Thank you, without you, these years would have been infinitely more difficult for me. Hope to see you soon!

To Marco, my adventure brother and his wife Nedy, for being honest, happy and always seeing the positive side of things. Never change! Thank you very much!.

To my friend of adventures and passions, Carlos, for always being present with laughter and words of support. Many thanks, tiger!

To Jorge Coniglio, my esteemed UNRC professor, for his support over the years, for being my distance tutor, counsellor, and for trusting me. Many thanks, Jorgito!

To Manuel, Nano and Lucio from the geology department of the UNRC. Each of you gave me strength so that today I could fulfil this goal. Many thanks for your support and advice.

To Vanessa, thank you very much for the friendship, support, companionship and teamwork.

To my friends: Rafaela, Jessica, Nadia, Raísa, Gaby, Simone, Everton, Luciano, Cleberson, Raphinha, Bruno, Lucas, Cesar, Robert, Sanny, Marcela S., Marcela M., Poli, Marina, Paola, Raísa, Rafael and Marcel. Thank you so much for all the moments lived, for the laughter, conversations and support. I'm carrying away a little of each of you and hope to meet you again!

To Verônica Trevisan for her help and advice in organizing the field trip, for sharing her experience and allowing me to use her samples and analyzes.

To all my Argentine friends who, in one way or another, have always been with me and accompanied me to reach this goal.

To Gorete, Cristina, Alexandre, Valdir and Maxlei for the help and innumerable explanations throughout these years. Thank you!

To Criatiane and the Institute of Chemistry for the enormous predisposition and help with the collection of hyperspectral images of high resolution.

To P.A. Gold Mineração company and the geologists Allan and Guilherme, for allowing this work to be carried out and the aid over the years.

To the METAMAT, Antônio João and Gilson from Coogavepe for the help and assistance during the field stage.

Thanks to the UNICAMP and the Institute of Geosciences for the opportunity to be part of their large family. To CAPES and FAPESP (Proc. Nr 2016 / 04370-5) for the encouragement and research promotion.

Thank you very much!

***“Que la tierra no da fruto si no la riega el sudor”***

***Martín Fierro***

## ABSTRACT

The Paraíba is an Au-Cu-Mo deposit located in the southern part of the Amazon Craton, in Alta Floresta Mineral Province, Mato Grosso, Brazil. It is composed by gold-rich quartz veins and Cu-Mo-rich hydrothermal breccias, both associated to several hydrothermal alteration zones. A novel method was applied here, involving the full integration of spectral (point and imaging spectroscopy) and conventional techniques (petrography, geochemistry, electron microprobe and SEM), with the aim to understand the geometry and evolution of the deposit and use this information to develop exploration vectors to mineralized zones.

More than 1,400 spectra of white mica, chlorite, biotite and epidote-bearing drill core samples were collected along transversal sections in the deposit by a spectrometer. In addition, hyperspectral images, with spatial resolutions of 156 and 30  $\mu\text{m}$ , were acquired on representative drill core samples. These data, integrated with petrographic studies and core logging, allowed a detailed alteration mineral mapping, as well as the recognition of temporal and spatial relationships among the alteration zones. Lithological and alteration sections, together with a mineral paragenetic sequence table and hydrothermal system evolution, were generated. Electron micro probe analysis revealed further information on the composition and crystallization temperature of the ore.

The integration of this multi-source dataset shows that the genesis of the Paraíba deposit is associated with two major mineralizing stages: (i) a first metamorphic-hydrothermal stage (Stage 1), related to Au-rich quartz veins in a ductile shear system; and (ii) a second magmatic-hydrothermal stage (Stage 2), associated with a syenogranite porphyry intrusion and Cu-Mo mineralization. Each stage has been divided into three principal sub-stages of mineralization: pre-ore, ore emplacement and post ore. Stage 1 comprises alteration zones marked by plagioclase destabilization, biotitization, silicification and phyllonite biotite's breakdown. Stage 2 comprises calcic, potassic, sericitic, propylitic alteration zones, with extensive epidotization, chloritization and late barren venules. Five chemically and spectrally different white mica groups, plus three chlorite groups, were discriminated. The combined use of composition, abundance and crystallinity extracted from spectral metrics for white mica represent a strong proxy to mineralized zones. The Au-Cu-Mo mineralization proved to be associated with higher abundance of well-ordered, highly crystalline, Al-poor and Mg-rich white micas, dominantly with trending-to-phengite to phengite composition. In this sense, the White Mica 2 and White Mica 4 are directly related to Au and Cu-Mo mineralization respectively, whereas the Al- and Fe-rich White Mica 1, 3 and 5 do not present relationship with ore zones. Chlorite groups 1 and 3, with a Mg-rich composition, are related to chloritization of phyllonites. A spatial relationship between epidotized zones and higher Cu contents was established.

The application of spectral techniques helped in the mineralogical characterization of different alteration zones and definition of mineral vectoring tools for exploration at the Paraíba deposit. This work demonstrates the importance of combining spectral and conventional techniques for the study of hydrothermal systems within complex mineral deposits.

**Key-words:** Ores - Alta Floresta (MT), hydrothermal alteration, gold mineralization, reflectance spectroscopy.

## RESUMO

O Paraíba é um depósito de Au-Cu-Mo localizado na porção sul do cráton Amazônico, na Província Mineral de Alta Floresta, Mato Grosso, Brasil. É formado por veios de quartzo com ouro e por brechas hidrotermais ricas em Cu-Mo, ambos associados a diversas zonas de alteração hidrotermal. Foi aplicado um novo método de estudo, envolvendo uma integração entre técnicas espectrais (espectroscopia pontual e de imageamento) e convencionais (petrografia, geoquímica, microsonda e MEV), com o objetivo de compreender a geometria e evolução do depósito, e utilizar essa informação no desenvolvimento de vetores de exploração para zonas mineralizadas.

Mais de 1400 espectros de mica branca, clorita, biotita e epidoto, foram coletados de amostras de testemunhos de sondagem através de um espectrômetro. Adicionalmente, foram geradas imagens hiperespectrais com resolução espacial de 156 e 30  $\mu\text{m}$  em porções representativas das amostras de testemunhos. A integração desses dados com estudos petrográficos permitiu um mapeamento detalhado da alteração mineral, bem como o reconhecimento das relações temporais e espaciais entre as zonas de alteração. Foram geradas seções litológicas e de alteração, juntamente com uma tabela da sequência paragenética e evolução hidrotermal. Análises por microsonda eletrônica revelaram informações sobre a composição e temperatura de cristalização do minério.

A integração deste conjunto de dados de múltiplas fontes mostra que a gênese do depósito Paraíba está associada a dois grandes estágios de mineralização: (i) um metamórfico-hidrotermal (Estágio 1), relacionado aos veios de quartzo ricos em Au, em um Sistema dúctil-rúptil; e (ii) um magmático-hidrotermal (Estágio 2), associado com intrusão de um corpo sienogranito porfirítico e mineralização de Cu-Mo. Cada estágio foi dividido em três principais sub-estágios: pré-mineralização, mineralização e pós-mineralização. O Estágio 1 compreende zonas de alteração marcadas pela desestabilização do plagioclásio, biotitização, silicificação e alteração da biotita do filonito. O Estágio 2 abrange zonas de alteração cálcica, potássica, sericítica e propilítica, com extensiva epidotização, cloritização e vênulas tardias estéreis. Foram discriminados cinco grupos espectral e quimicamente distintos de mica branca, e três de clorita. O uso combinados da composição, abundância e cristalinidade, extraídos de métricas espectrais para mica branca, representam um forte farejador para zonas mineralizadas. A mineralização de Au-Cu-Mo está associada à abundância de mica branca altamente cristalina, pobre em Al e rica em Mg, predominantemente com composição tendendo a fengita a fengítica. Nesse sentido, a Mica Branca 2 e Mica Branca 4 estão diretamente relacionadas a mineralizações de Au e Cu-Mo, respectivamente, enquanto que a Mica Branca 1,3 e 5, rica em Al e Fe, não apresenta relação com zonas mineralizadas. Grupos da Clorita 1 e 3, com composição rica em Mg, estão relacionados a cloritização de filonitos. Foi estabelecida uma relação espacial entre zonas epidotizadas e altos teores de Cu.

A aplicação de técnicas espectrais auxiliou na caracterização mineralógica de diferentes zonas de alteração e na definição de minerais vetores para exploração no depósito Paraíba. Este trabalho demonstra a importância de combinar técnicas espectrais e convencionais para o estudo de sistemas hidrotermais complexos.

**Palavras chaves:** Minérios Alta Floresta (MT), alteração hidrotermal, mineralizações de auríferas, espectroscopia de reflectância.

## LIST OF FIGURES

<b>Figure 1:</b> Alta Floresta Mineral Province (AFMP) map location and its geological domain. The area delimited in the right side corresponds to the eastern sector of the province, where there is a high concentration of gold deposits aligned in a NW-SE direction (Assis 2011 - Modified from Paes de Barros 2007). .....	21
<b>Figure 2:</b> Distribution of the tectono-chronological provinces of the Amazonian Craton according to a) Tassinari and Macambira (1999) and b) Santos <i>et al.</i> (2000). Red box: Alta Floresta Mineral Province (AFMP). Black square: AFMP Eastern sector (From Pavel, 2016). .....	26
<b>Figure 3:</b> Geological map of the AFMP eastern sector (Assis 2015, Modified from Miguel Jr 2011). .....	27
<b>Figure 4:</b> Crystallization ages of the main Paleoproterozoic intrusive bodies of the eastern sector of the AFMP based on U-Pb data in zircons (Assis 2015). .....	33
<b>Figure 5:</b> Satellite Worldview 2 false colour composite (bands 873 in RGB) image of the Paraíba deposit (axis of the ore bodies marked by dashed red line) showing the location of boreholes BH020, BH041 and BH059, which compose an archetype cross section of the deposit (line A-A'). Purple circles correspond to other and also some exploratory boreholes. Inactive open-pits, currently flooded, can also be spotted in the image. Colours in the image can be interpreted as follows: yellow pixels correspond to vegetation; black to water, light blue to humid crops, white to exposed soil and blue to mining infrastructure. ....	38
<b>Figure 6:</b> Major spectral absorption bands in the SWIR (Pontual <i>et al.</i> 2008). .....	42
<b>Figure 7:</b> a-b) Current open-pit photographs that were exploited to an approximate 30 meters depth and that are currently flooded. ....	46
<b>Figure 8:</b> a) Gallery photograph, currently flooded. b) Location of the shaft and elevator for transporting material and workers during the operation time of the mine. ....	47
<b>Figure 9:</b> Macro aspects of the lithotypes from Paraíba deposit. (a) Biotite gneiss with gneissic banding; (b) Paraíba tonalite; (c) Phyllonite; (d) Fine-grained gabbroic dyke cutting the Paraíba Tonalite; (e) Gabbro with serial texture and porphyritic plagioclase phenocryst; (f) Syenogranite porphyry; (g) Quartz-rich syenogranite felsic dyke cutting the Paraíba Tonalite. ....	49
<b>Figure 10:</b> Main section of the Paraíba deposit, showing the relevant lithotypes and structures. The temporal and spatial relationships among them and the areas with the highest Cu and Au values are indicated. Vertical and horizontal scales are similar. ....	52

<b>Figure 11:</b> Paraíba main section with hydrothermal alteration zones. Vertical and horizontal scales are similar. Bt= biotite; Phl= phlogopite.....	54
<b>Figure 12:</b> a) Paraíba tonalite showing a stronger alteration near to deformed areas, related to the first mineralized event; b) feldspar alteration, principally plagioclase, generating fine white mica, represented by illite and muscovite (normal potassic composition). Ill: Illite; Ms: Muscovite; Qtz: Quartz; Cal: Calcite; Ep: Epidote; Pl: Plagioclase. ....	56
<b>Figure 13:</b> a) Phyllonite hand sample; b) Thin section (crossed nicols) of the phyllonite BH020-019 sample at 125 meters of depth, composed of magnesian biotite; c) Thin section (crossed nicols) of the phyllonite BH041-016 sample at 360 meters of depth; d) Electron microprobe image (same location as figure 13c) showing some phlogopites crystals with internal compositional zonation; e) Characteristic phyllonite spectra, with phlogopite and biotite (i) and subordinate white mica associated with the phlogopite alteration (ii). Phl: Phlogopite; Qtz: Quartz; Py: Pyrite; Bt: Biotite; Chl: Chlorite. ....	58
<b>Figure 14:</b> Photo (left) and mineral spectral map (right) produced from SisuCHEMA image of the BH041-016 hand sample. Representative SisuCHEMA spectra employed in SAM classification are illustrated with correspondent mineral interpretations. ....	59
<b>Figure 15:</b> a) Principal 'Paraíba Vein' in the interior of the gallery; b) Quartz vein with centimetric sulphide bands. ....	60
<b>Figure 16:</b> a) Phyllonite thin section (crossed nicols) composed of biotite and calcite. The biotite crystals are overprinted by chlorite and phengite; b) Phyllonite thin section photograph in which is possible to observe biotite crystals altering to chlorite and titanite, where the brown core corresponds to relictic biotite.; c) Phyllonite (crossed nicols) composed of quartz + phlogopite + pyrite, with fine chlorite crystals generated from the alteration of phlogopites; d) Electron microprobe image of phyllonite composed of quartz + phlogopite + pyrite, with fine chlorite crystals generated from the phlogopite crystals alteration; e) Characteristic spectra from different zones of the phyllonite and respective mineral mixtures. Chl: Chlorite; Phg: Phengite; t-Phg: Tending to phengite; Bt: Biotite; Cal: Calcite; Ttn: Titanite; Phl: Phlogopite; Qtz: Quartz; Py: Pyrite.....	61
<b>Figure 17:</b> Phyllonite sample associated with Py of the Paraíba principal vein (left) and mineral spectral map produced from SisuCHEMA image (right) of drill core sample from Paraíba deposit. Representative SisuCHEMA spectra employed in SAM classification are illustrated with correspondent mineral interpretations. ....	62
<b>Figure 18:</b> a) Calcic alteration represented by Qtz + Ab + Act crystallizing from fractures; b) Potassic 1 alteration (crossed nicols), altered Kfs grains forming hydrothermal Bt; c)	

Hydrothermal Bt grains associated with Mag with coronitic texture of Ttn at crossed nicols; d) Crossed nicols photograph of Qtz, Anh and Kfs grains associated with abundant hematite; f) SEM image showing fractured Kfs grains associated with Hem and Ep in the matrix; g-i) Characteristic Act spectrum, principal constituent of the calcic alteration; g-ii) Mixture spectrum between biotite and phlogopites, typic of zones with intense potassic alteration. Act: Actinolite; Ab: Albite; Qtz: Quartz; Pl: Plagioclase; Bt: Biotite; Ser: Sericite; Mc: Microcline; Ap: Apatite; Ttn: Titanite; Mag: Magnetite; Anh: Anhydrite; Hem: Hematite; Ep: Epidote. .65

**Figure 19:** a) Potassic biotite breakdown alteration (crossed nicols) represented by Wm + Ilm + Rt + Ttn + Qtz; b) Potassic biotite breakdown alteration, Bt crystals altered to muscovite and the Ti-release form Ilm and Rt. Ms: Muscovite; Rt: Rutile; Ilm: Ilmenite; Qtz: Quartz; Bt: Biotite; Ttn: Titanite; t-Phg: Tending to phengite. ....65

**Figure 20:** a) Hand sample photo and mineral maps produced from SisuCHEMA image of drill core sample. Representative white mica SisuCHEMA spectra, with White mica 1 and 3 abundance and composition. b) Hand sample photo and mineral map produced from SisuCHEMA device with correspondent mineral interpretations. Ep: Epidote; Wm: White mica; Ms: Muscovite; t-Phg: Tending to phengite; Chl: Chlorite; Qtz: Quartz. ....66

**Figure 21:** a) Sericitic alteration (crossed nicols) represented by quartz + pyrite + chalcopyrite + muscovite ± molybdenite ± calcite; b, c, d) Sericitic veins cutting the tonalite and presenting a mineral assemblage of quartz + phengite + pyrite + chalcopyrite ± molybdenite. In occasions white mica could be muscovite/illite phengite; e) Representative muscovite “tending to” phengite (2215) to phengite ASD spectra (2221 nm) associated with quartz and chlorite related to the primary tonalite mineral alteration. Ms: Muscovite; Qtz: Quartz; Cal: Calcite; Ill: Illite; Py: Pyrite; Mo: Molybdenite. ....68

**Figure 22:** a) Propylitic alteration (crossed nicols) represented by chlorite + epidote + calcite; (b and c) Epidotization (crossed nicols) represented by disseminated chalcopyrite and molybdenite crystals; d) MEV photograph of Mo crystals associated with the Epidotization alteration zone; e) Propylitic and Epidotization characteristic ASD spectra. Ep: Epidote; Chl: Chlorite; Qtz: Quartz; Cal: Calcite; Mo: Molybdenite. ....70

**Figure 23:** Potassic 2 alteration composed of K-feldspar and large amounts of hematite crystals. This alteration is cut by sericitic venules and finally fractured and obliterated by an epidote-rich fluid, which will generate the hydrothermal breccia (left) and a mineral map produced from SisuCHEMA image (right), with a spatial resolution of 156 µm, related to the BH041-012 sample. Representative SisuCHEMA spectra used in SAM classification. ....71

<b>Figure 24:</b> Epidotized phyllonite (left) and mineral map produced from SisuCHEMA image (right), with a spatial resolution of 30 $\mu\text{m}$ , and related to the BH059-046. Representative SisuCHEMA spectra used in SAM classification. ....	72
<b>Figure 25:</b> a) Chloritized phyllonite with a black greyish colouration and fine texture; b-c) Chloritization (crossed nicols), showing the Chl crystals and the relic phlogopite founded in the Py border grains; d) Chloritization electron microprobe photograph, showing Phl crystals surrounding Py grains; e) Characteristic chloritization ASD spectra, showing an intermediate Mg-Fe composition. Phl: Phlogopite; Chl: Chlorite; Ttn: Titanite; Py: Pyrite. (BH059-041 sample). ....	73
<b>Figure 26:</b> Chloritized phyllonite with a black greyish colouration and fine texture (left) and mineral map produced from SisuCHEMA image (right) with a spatial resolution of 156 $\mu\text{m}$ and related to the BH059-041 sample. Representative SisuCHEMA spectra used in SAM classification, showing how the phlogopite crystals are replaced by chlorite crystals.....	74
<b>Figure 27:</b> a) Barren Qtz veinlet cutting the porphyric syenogranite; b) Late Qtz vein + Ms (white mica) (crossed nicols); c) Late Qtz vein + Ms (White Mica 5) electron microprobe photograph; d) Late Qtz + Fluorite vein (crossed nicols). Qtz: Quartz; Ep: Epidote; Hem: Hematite; Ill: Ilmenite; Cpy: Chalcopyrite; t-Phg: tending to phengite; Fl: Fluorite; Kfs: K-feldspar. ....	75
<b>Figure 28:</b> White mica compositional variations of the Paraíba deposit using the ternary diagram proposed by Tappert (2013). ....	77
<b>Figure 29:</b> a) Correlation diagram $\text{Al}^{\text{VI}}$ vs (Fe + Mg); and b) $\text{Al}_{(\text{t})}$ vs [Si + (Fe + Mg)] for the white micas from the Paraíba deposit. $R^2$ = Correlation coefficient. ....	78
<b>Figure 30:</b> Representation of the Paraíba white micas chemical composition using the $\text{MR}^3 - 2\text{R}^3 - 3\text{R}^2$ diagram proposed by Velde (1985). (M = Muscovite; A = Magmatic Micas; B = Phengites; C = Illites; D= Illites associated with Chlorite; E = Illite in sandstones, in the first stages of weathering and in hydrothermal events of granitic rocks. $\text{MR}^3 = \text{Na} + \text{K} + 2\text{Ca}$ ; $2\text{R}^3 = (\text{Al}_{(\text{t})} - \text{MR}^3)/2$ ; $3\text{R}^2 = (\text{Fe} + \text{Mg})/3$ .....	78
<b>Figure 31:</b> Representation of the Paraíba white micas chemical composition using the $\text{Al}^{\text{IV}} - \text{Al}^{\text{VI}} - \text{Fe}_{(\text{t})} + \text{Mg}$ , ternary diagram proposed by Guidotti (1987). It is possible to see the same two compositional clusters previously observed in figure 28. FMu = Ferri-Muscovite; Mu = Muscovite; Ph = Phengite; FPh = Ferri-Phengite; Mu = Muscovite. ....	79
<b>Figure 32:</b> Representation of the Paraíba's biotite and phlogopite chemical composition using the $\text{Al}^{\text{iv}}$ vs Fe# diagram proposed by Tamizel (2014). ....	81

<b>Figure 33:</b> Representation of biotite and phlogonite from Paraíba deposit chemical composition using the ternary diagram of classification of trioctahedral micas given by Mg - (Al <sup>VI</sup> + Fe <sup>3+</sup> + Ti) - (Fe <sup>2+</sup> + Mn) and proposed by Foster (1962). .....	82
<b>Figure 34:</b> Representation of the Paraíba's biotite and phlogopite chemical composition using the ternary diagram proposed by Nachit <i>et al.</i> (2005), that allow distinguishing igneous primary biotite from re-equilibrated and secondaries ones. ....	83
<b>Figure 35:</b> Representation of the Paraíba's epidote chemical composition using the ternary diagram proposed by Kartashov (2014). ....	84
<b>Figure 36:</b> Representation of the chlorite's composition from the Paraíba deposit according to the ratio proposed by Foster (1962) between Si vs Fe <sup>2+</sup> /(Fe <sup>2+</sup> + Mg <sup>2+</sup> ). ....	85
<b>Figure 37:</b> Representation of the chlorite's composition from the Paraíba deposit according to the ratio proposed by Ciesielczuk (2012) between #Al <sup>IV</sup> vs #Fe. ....	86
<b>Figure 38:</b> Representation of the variations in the concentration of FeO and MgO in the group of chlorites, implying the substitution of Fe <sup>2+</sup> by Mg <sup>2+</sup> in the octahedral layers, according to Foster (1962). ....	86
<b>Figure 39:</b> Correlation diagram between Fe/(Fe+Mg) vs Al <sup>IV</sup> for chlorite samples from the Paraíba deposit, according to Foster (1962) and Zang and Fyfe (1995). ....	87
<b>Figure 40:</b> Chlorites crystallization temperatures from the Paraíba deposit, calculated using the Inoue <i>et al.</i> (2009) geo-thermometer. ....	88
<b>Figure 41:</b> Chlorites crystallization temperatures from the Paraíba deposit, calculated using the Bourdelle <i>et al.</i> (2013) geo-thermometer on Wiewióra and Weiss (1990) diagram. ....	89
<b>Figure 42:</b> a) Histogram of white mica composition for all samples analysed and Au content in colours. It shows the relationship between the two groups and the higher Au values, evidencing a trend in wavelengths from 2214 to 2224 nm; b) Histogram of white mica composition for all samples analysed and Cu content in colours. It shows a better correlation with the larger group but it was not possible to observe a specific trend with the highest Cu values. The spectra of white mica with different composition are show at right. ....	90
<b>Figure 43:</b> White mica spectra of the Paraíba deposit with different crystallinities and different mixture proportions of illite-smectite interstratifications. The crystallinity index (CI) limit values are shown in red, calculated by ratioing the depth of Al-OH absorption at 2200 nm by the water absorption at 1900 nm (based on Pontual <i>et al.</i> 2008 and Ducart and Stolf, 2018). ....	91

<b>Figure 44:</b> BH041 StripLog, showing the relationship between the white mica spectral parameters, the Au-Cu values, and their association with the main hydrothermal alterations and the summary TSG 8 interpretation.....	93
<b>Figure 45:</b> Strip-log from the borehole BH041, showing in detail the white mica composition and its relationship with the lithotypes, hydrothermal alterations and mineralization. ....	94
<b>Figure 46:</b> Global chlorite composition analysis according to wavelength position and their relationship with the Au and Cu values.....	96
<b>Figure 47:</b> Global epidote composition analysis according to ~1550 wavelength position and their relationship with the Cu values. ....	97
<b>Figure 48:</b> a) Correlation between Si + [Fe + Mg] and b) Al <sub>(t)</sub> contents of white mica (from EPMA data, for 11O atoms) and position of 2200 nm absorption feature.....	98
<b>Figure 49:</b> a) Correlation between #Mg; b) #Fe <sub>(t)</sub> contents of chlorites (from EPMA data, for 14O atoms) and position of 2340 nm absorption feature. ....	98
<b>Figure 50:</b> Relationship between the biotite Mg contents and its variation with respect to depth from the actual surface. ....	101
<b>Figure 51:</b> Proposed evolutionary history of the Paraíba deposit summarized in 6 main stages. ....	107

## LIST OF TABLES

<b>Table 1:</b> Main geological units, geochronology and tectonic environment of the eastern sector of the AFMP (Taken from Trevisan, 2015; modified from Assis, 2015).*Not available isotopic data. ....	31
<b>Table 2:</b> Operational conditions and standards used in the EMPA. ....	44
<b>Table 3:</b> Paragenetic temporal evolution proposed for the Paraíba deposit. ....	55
<b>Table 4:</b> Summary table of the 5 groups of white mica described for the Paraíba deposit with their respective average concentrations of Al <sub>(t)</sub> , Fe <sub>(t)</sub> , Si and Mg. ....	76
<b>Table 5:</b> Location of the 6 zones of interest of the borehole BH041 and the hydrothermal alteration associated.....	92
<b>Table 6:</b> Main attributes identified for white mica groups. ....	99
<b>Table 7:</b> Main attributes identified for chlorite groups.....	100
<b>Table 8:</b> Main attributes identified for biotite groups.....	100
<b>Table 9:</b> Comparison of orogenic gold and intrusion-related gold deposits in terms of their critical regional-to deposit-scale characteristics and its relationship with the Paraíba deposit features. Concordant features are marked with a green tick, partially concordant with an orange tick, no-concordant with a red tick, and features for which there is no update information with a blue interrogation symbol. (Modified from Groves <i>et al.</i> 2003). ....	104

## INDEX

1. INTRODUCTION.....	21
2. OBJECTIVES .....	24
3. GEOLOGICAL SETTING .....	25
3.1. Regional geology .....	25
3.2. Eastern sector geology of AFMP .....	26
3.2.1. Basement (2.8 - 1.97 Ga).....	28
3.2.2. Pluto-volcanic calc-alkaline units and volcano-sedimentary sequences (1.97 - 1.78 Ga). ....	28
3.2.3. Anorogenic pluto-volcanic units (1.77 - 1.75 Ga).....	29
3.2.4. Sedimentary sequences (1.44 Ga – Cenozoic) .....	29
3.3. Tecto-magmatic evolution of AFMP .....	32
3.4. Metalliferous deposits in the eastern sector of the AFMP.....	35
3.5. Metallogenic models of Au ± Cu, Cu ± Mo and Au ± base metal deposits of the AFMP eastern sector.....	35
4. ANALYTICAL PROCEDURES .....	38
4.1. Field trip.....	38
4.2. Reflectance spectroscopy .....	39
4.2.1. White Mica .....	39
4.2.2. Chlorite .....	40
4.2.3. Biotite .....	41
4.2.4. Epidote.....	41
4.2.5. Calcite.....	41
4.2.6. Actinolite .....	41
4.3. Petrography .....	43
4.4. Scanning electron microscope (SEM) .....	43
4.5. Mineral chemistry .....	43

4.6.	Imaging Spectroscopy on Drill Core Samples.....	44
5.	PARAÍBA DEPOSIT.....	46
5.1.	Main features .....	46
5.2.	Lithotypes .....	49
5.3.	Mineralization and Hydrothermal Alteration.....	53
5.3.1.	Pre-ore stage 1 - Plagioclase destabilization .....	56
5.3.2.	Ore-stage 1 - Biotitization .....	57
5.3.3.	Ore-stage 1 – Silicification .....	59
5.3.4.	Post-ore stage 1 - Phyllonite biotite breakdown.....	60
5.3.5.	Pre-ore stage 2 – Calcic .....	62
5.3.6.	Pre-ore stage 2 - Potassic 1 and Potassic 2.....	63
5.3.7.	Pre-Ore stage 2 - Potassic biotite breakdown.....	65
5.3.8.	Ore Stage 2 – Sericitic .....	67
5.3.9.	Ore Stage 2 - Propylitic and Epidotization.....	69
5.3.10.	Post-ore Stage 2 - Chloritization, late phases and barren veins.....	72
6.	MINERAL CHEMISTRY .....	76
6.1.	White mica .....	76
6.2.	Biotite – Phlogopite .....	79
6.3.	Epidote .....	83
6.4.	Chlorite .....	84
6.4.1.	Chlorite crystallization temperature .....	87
7.	DISCUSSION .....	90
7.1.	Reflectance spectroscopy.....	90
7.1.1.	White mica.....	90
7.1.2.	Chlorite .....	95
7.1.3.	Epidote.....	96
7.2.	Validating reflectance spectroscopy and mineral chemistry .....	97

7.3.	Chlorite crystallization temperature and fluid inclusions correlation.....	98
7.4.	White mica, chlorite and biotite comparison .....	99
7.5.	Timing and mineral evolution.....	101
8.	CONCLUSIONS .....	108
9.	REFERENCES.....	110
	APPENDIX 1: White mica electron microprobe chemical data .....	124
	APPENDIX 2: Chlorite electron microprobe chemical data.....	128
	APPENDIX 3: Biotite electron microprobe chemical data. ....	131
	APPENDIX 4: Epidote electron microprobe chemical data. ....	134

## 1. INTRODUCTION

The Alta Floresta Mineral Province (AFMP), also known as Alta Floresta Auriferous Province (PAAF), is located in the southern part of the Amazon Craton, corresponding to the northern part of the Mato Grosso state. The province is elongated along a NW-NE trend, and is bounded to the north by the Cachimbo Graben, which separates it from the Tapajós Auriferous Province (TAP), and to the south by the Caiabís Graben (Fig. 1).

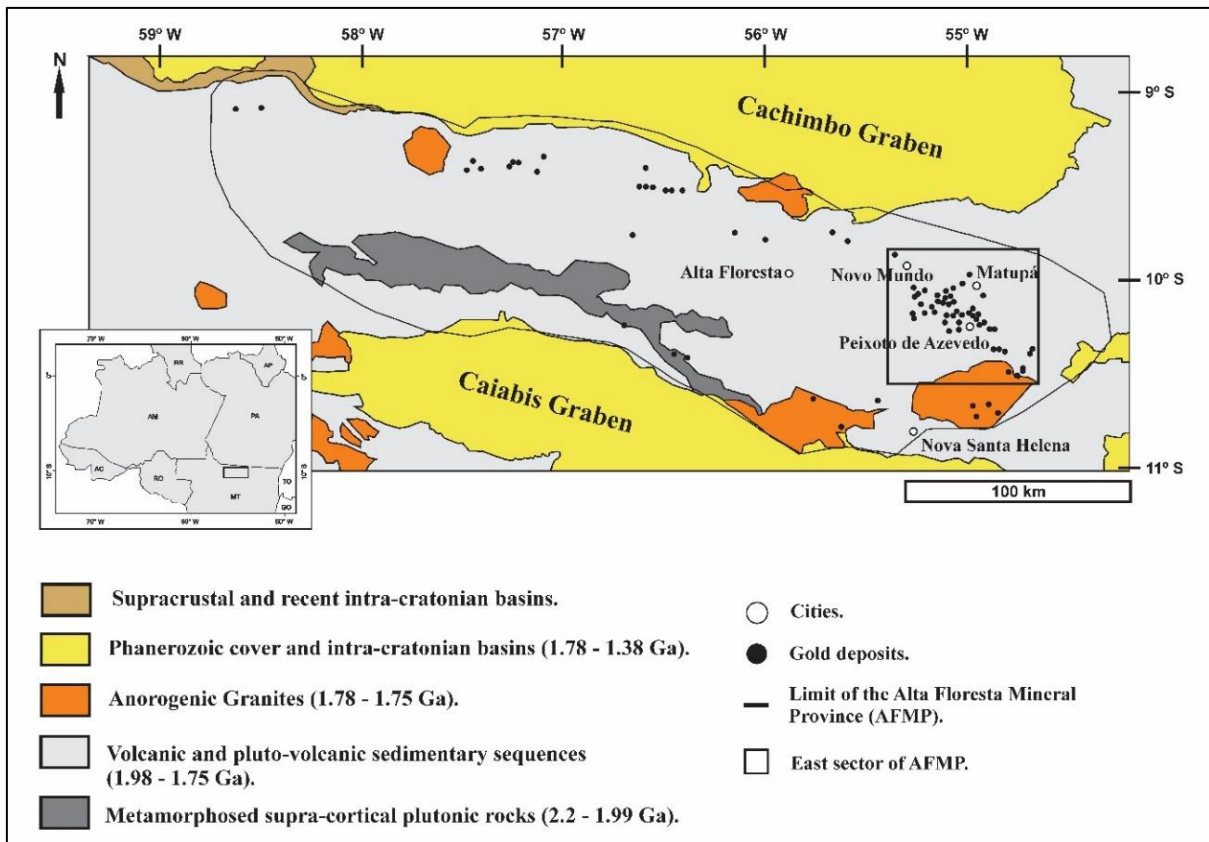


**Figure 1:** Alta Floresta Mineral Province (AFMP) map location and its geological domain. The area delimited in the right side corresponds to the eastern sector of the province, where there is a high concentration of gold deposits aligned in a NW-SE direction (Assis 2011 - Modified from Paes de Barros 2007).

The AFMP represents one of the provinces with a paramount potential for gold and copper production in Brazil. The gold production, between the decades of 1980s and 1990s, was approximately 160 t of gold (Paes de Barros 2007). The metalliferous deposits located in the eastern sector of the AFMP are divided into three groups: (i) Au  $\pm$  Cu disseminated and (ii) in veins (e.g. Pé Quente, Luizão, Basílio, Dionísio, X1, Serrinha and Paraíba deposits), and (iii) Au + Zn + Pb  $\pm$  Cu veins (e.g. Bigode, Francisco and Luiz Bastos).

Recently, a four group characterized by disseminated Cu + Mo  $\pm$  Au mineralizations (e.g. Ana, Jaca and the Paraíba deposits) (Assis 2015), was proposed.

The Paraíba is one of the most representative structurally-controlled Au-rich mineralization systems within the province, located about 12 km to the west from Peixoto de Azevedo city. It is composed of three lenticular and branched sulphides-rich quartz veins with a length of approximately 1,500 m and also areas with intense hydrothermal alteration. The deposit was previously studied by numerous authors, such as Abreu Filho *et al.* (1992), Paes de Barros (1994, 2007), Assis (2006), Santos (2011), Trevisan (2015), and Bartolomeu (2016). Abreu Filho *et al.* (1992) made lithotype descriptions, geophysical studies, and description of hydrothermal alterations. Paes de Barros (1994) described the granitoids of the area, country rock description and cross section design. Paes de Barros (2007) carried out Pb-Pb zircon geochronology in the Paraíba vein ( $1.979 \pm 3$  M.a) and fluid inclusion studies. Assis (2006) made fluid inclusion studies on sulphide-rich quartz veins. Santos (2011) carried out Pb-Pb pyrite geochronology in the Paraiba vein ( $1.814 \pm 22$  M.a). Trevisan (2015) described some lithotypes like the gneiss, tonalite and mafic dykes, fluid inclusion studies, and U-Pb geochronology of the tonalite ( $2.014 \pm 3$  M.a) and vein textures and hydrothermal alteration description. Finally, Bartolomeu (2016) made the description of the syenogranite porphyry found in the vicinity of the deposit. In addition, different interpretations were proposed regarding the metallogenetic models for the vein-type Au  $\pm$  Cu deposits. Siqueira (1997), Santos *et al.* (2001), Moreton and Martins (2005), Paes de Barros (2007), and Silva and Abram (2008) classify it as an orogenic gold deposit; Paes de Barros (2007) and Trevisan (2015) as an intrusion-related gold (IRGS) deposit; and Santos *et al.* (2001) as an intrusion-centered and/or intrusion-related type. For the Au + Cu disseminated type deposits, an IRGS genesis is proposed by Paes de Barros (2007) and related to a porphyry type by Moura *et al.* (2006) and Assis (2015).

The majority of the previous works showed that the Paleo-Proterozoic Paraiba deposit, as many others that compose the AFMP, is characterized by so many overlapping hydrothermal events that make its exploration, using conventional techniques, very complicated. Recognizing very fine grained alteration minerals and overlapping halos is a tricky task, even for experienced geologists. In this approach, reflectance spectroscopy represents a rapid, cheap, effective and non-destructive technique for the characterization of alteration minerals (Hauff *et al.* 1989, Scott and Yang 1997, Ducart 2007, Doublier *et al.* 2010, Tappert *et al.* 2011, Laukamp *et al.* 2011, Roache *et al.* 2011, Cudahy *et al.* 2016, Wang *et al.* 2017). In spite of the high capacity of these spectral techniques for mapping

alteration minerals, is still not widely used in Brazil (Passos 1998; Passos, 1999; Souza Filho and Passos 1999; Prado *et al.* 2016; Naleto 2018).

Minerals, rocks and other terrestrial compounds exhibit diagnostic absorption features in either the visible-near infrared (VNIR) (400 - 1000 nm), short-wave infrared (SWIR) (1000 - 2500 nm), mid-infrared (MIR) (3000 - 5000 nm), and/or longwave infrared (LWIR) (8000 - 14000 nm) regions in response to electronic and vibrational processes, as well as overtones (Clark 1999, Hook *et al.* 1999). Alteration minerals such as white mica, chlorite and epidote are characteristic of several types of hydrothermal systems and commonly present compositional variations with distance to the system (Sillitoe 2010, Halley *et al.* 2015, Phillips and Powell 2015, Chmielowski *et al.* 2016, Wang *et al.* 2017, Neal *et al.* 2018). The spectral signature of alteration minerals is increasingly being used as a vector to find, measure and map alteration zones. The quantitative information characterization from spectral techniques allows determining the abundance and physical-chemical properties of minerals such as composition and degree of structural ordering (Ducart *et al.* 2015, 2016). It indirectly provides information about hydrothermal fluid, temperature and composition (Reyes 1990) and, therefore, can be used to interpret the physical size, paleo-hydrological structure and evolution of the system. On a detailed scale, hyperspectral images with high spatial resolution obtained from borehole samples help to verify the spatial and temporal relationships of the alteration pattern (Travers and Wilson 2015, Naleto 2018).

Based on the knowledge of the effectiveness of the spectral techniques for the study of hydrothermal alteration minerals, it was try to develop a more effective method to study the Paraiba deposit, by integrating traditional techniques (petrography, geochemistry, electron microprobe and SEM) and spectral exploration techniques. Therefore, this work presents a novel procedure that can assist the future exploration for Au-Cu-Mo deposits in the AFMP.

## 2. OBJECTIVES

---

The major aim of this work is to understand the spatial distribution and evolution of the Paraíba hydrothermal system, and use this information to develop exploration vectors that can be applied locally and regionally in the AFMP.

In this sense, this master's dissertation seeks:

- To map in detail the lithotypes and the hydrothermal alteration zones observed in the deposit.
- To propose a paragenetic sequence chart and evolution model for the deposit.
- To obtain information about the composition, crystallinity and abundance of the minerals that composes the different hydrothermal alteration zones using spectral data.
- To validate the spectral results with mineral chemistry.

### 3. GEOLOGICAL SETTING

---

#### 3.1. Regional geology

The Amazonian Craton, defined by Almeida (1978), is located in the northern extreme of South America. It is limited by the Neoproterozoic orogenic belts of Tucavaca in Bolivia, Araguaia-Cuiabá in central Brazil and Tocantins to the North (Almeida *et al.* 1976, Cordani *et al.* 1988, Tassinari and Macambira 1999). In Brazil, the craton is bounded by the Baixo Araguaia group to the East and with Alto Paraguay, Cuiabá and Corumbá groups to the South and South-east. It limits with the Maranhão phanerozoic basin to the North-east, with Xingu and Alto Tapajós to the South, with Parecis to the South-west, Solimões to the West and with Tacutu to the North. To the centre, the Amazonian basin is covering the tectonic area (Santos 2003).

Several authors have divided the Amazonian craton into different geochronological provinces. According to the model of Tassinari and Macambira (1999), the AFMP is located between the Ventuari-Tapajós (1.95 to 1.8 Ga) and Rio Negro-Juruena (1.8 – 1.55 Ga) geo-chronological provinces, whereas Santos *et al.* (2000) propose that it is located between the tectono-chronological provinces of Tapajós-Parima (2.03 - 1.88 Ga) and Rondônia-Juruena tectonic provinces (1.82 - 1.54 Ga) (Fig. 2).

Apart from the geochronologic division, this area has been interpreted to be generated in a magmatic arc environment, related to subduction events with SO-NE direction, developed and amalgamated during the Paleo and Mesoproterozoic to the proto-craton designated as Central Amazonian Province (Tassinari and Macambira 1999, Santos *et al.* 2006, Silva and Abram 2008). However, recent contributions proposed by Juliani *et al.* (2013) have demonstrated the absence of island arc terranes, metamorphism and deformation correlated to collisional processes in the Central Amazon and Ventuari-Tapajós (Tassinari *et al.* 1999) or Tapajós-Parima (Santos *et al.* 2000) provinces. According to the authors, based on fieldwork, geochemistry, geophysical studies and isotope geology the Amazonian Craton is essentially composed of two continental magmatic arcs developed between 2.0 and 1.86 Ga, named as Tapajonic Arcs, with a possible flat subduction stage, under an Archean-Paleoproterozoic continent. In this model, E-W structures approximately parallel to the trench of a northward subduction zone would control the emplacement of different calc-alkaline magma and volcanism. According to Juliani *et al.* (2013) and Fernandes (2010), these magmatic arcs were, at least in part, overlapped.

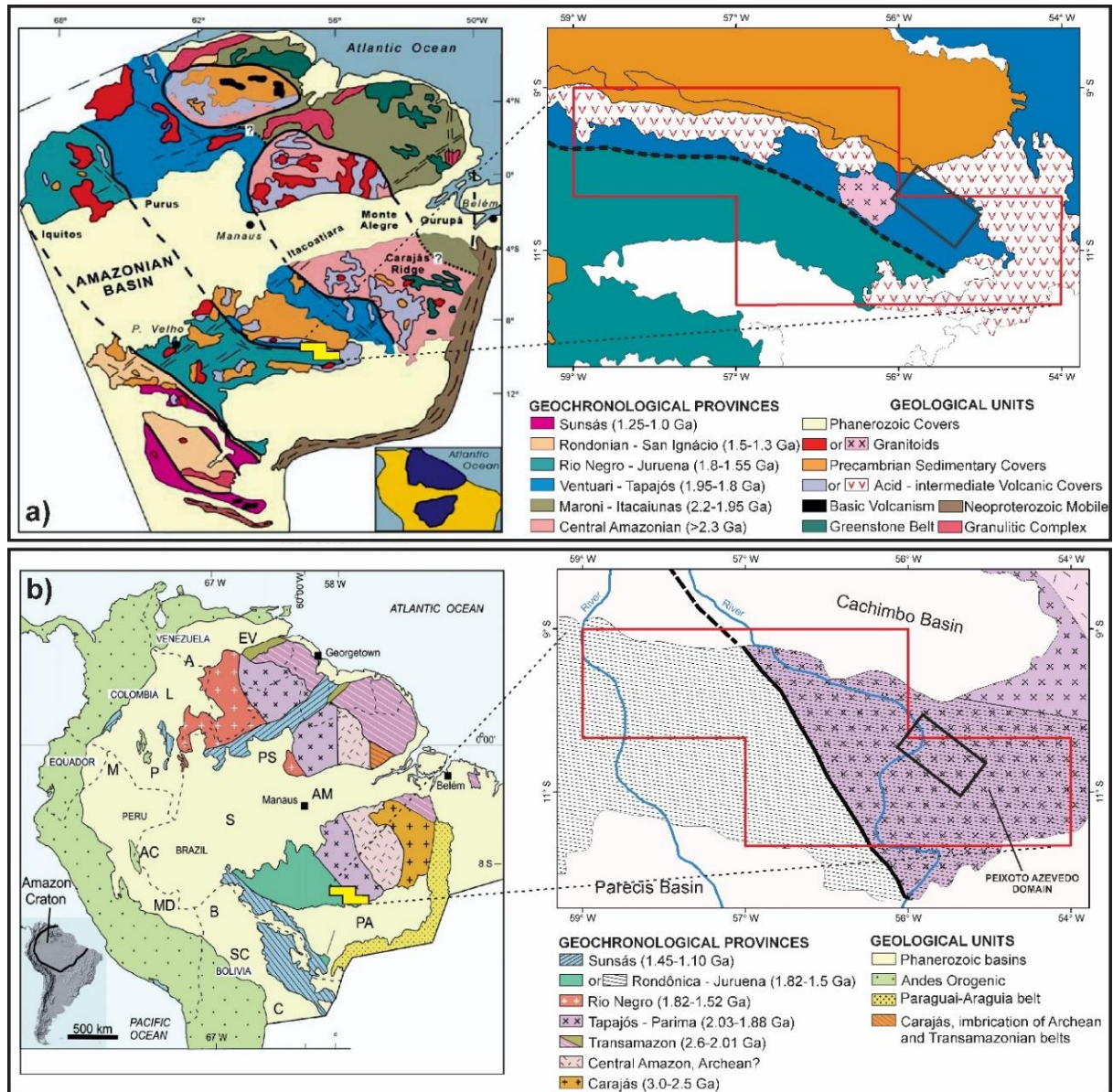


**Figure 2:** Distribution of the tectono-chronological provinces of the Amazonian Craton according to a) Tassinari and Macambira (1999) and b) Santos *et al.* (2000). Red box: Alta Floresta Mineral Province (AFMP). Black square: AFMP Eastern sector (From Pavel 2016).

### 3.2. Eastern sector geology of AFMP

The geology of the eastern sector of the AFMP can be divided into the following geological domains: i) basement (2.8 - 1.97 Ga); ii) pluto-volcanic calc-alkaline units and volcano-sedimentary sequences (1.97 - 1.78 Ga); iii) syn-orogenic to anorogenic pluto-volcanic units (1.77 - 1.75 Ga); and iv) sedimentary sequences (1.44 Ga – Cenozoic) (Assis 2015), and can be seen in figure 3 and ordered in Table 1.

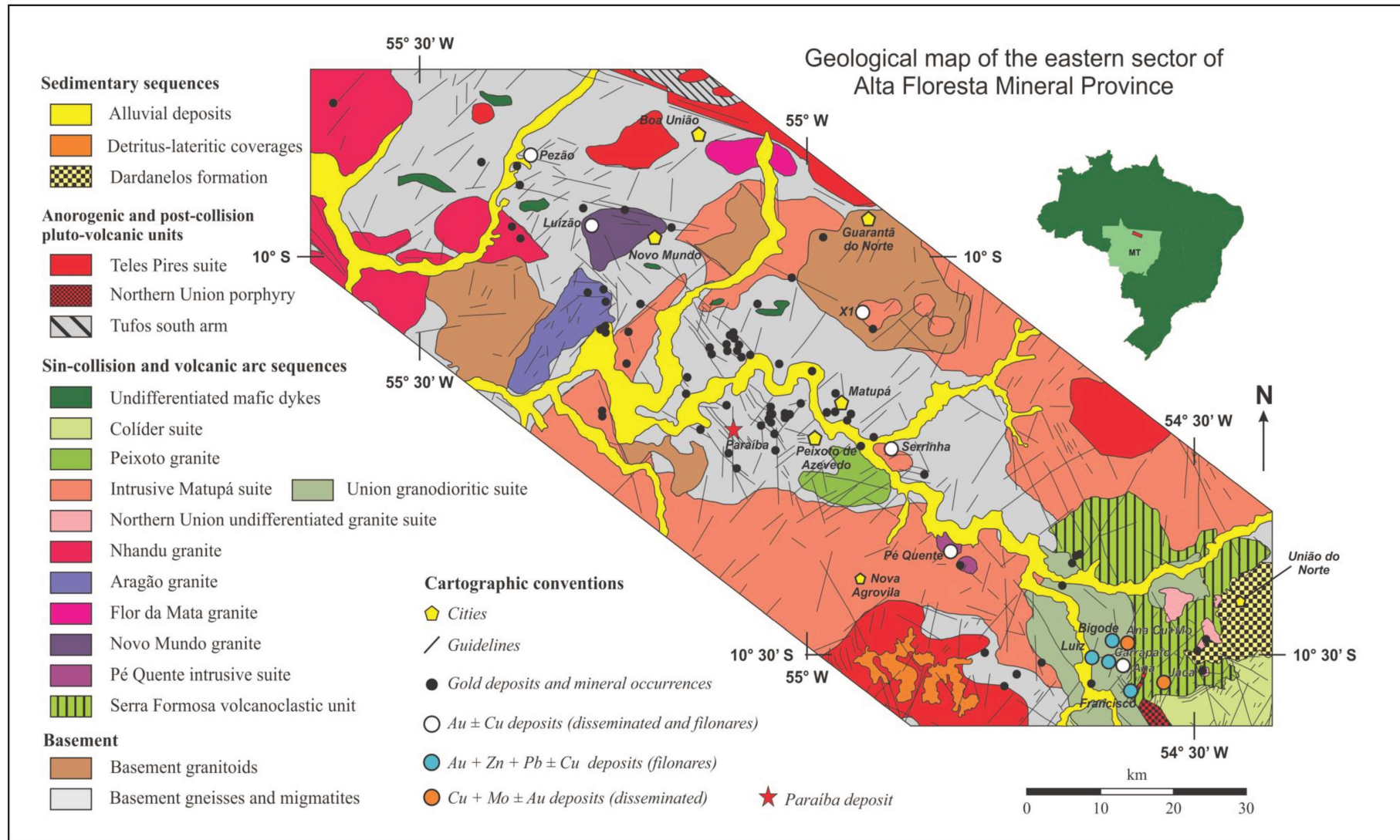


**Figure 3:** Geological map of the AFMP eastern sector (Assis 2015, Modified from Miguel Jr 2011).

### 3.2.1. Basement (2.8 - 1.97 Ga)

The basement, belonging to Cuiú-Cuiú suite, is characterized by migmatite and granitic to tonalitic gneiss intruded by foliated granitoids with calc-alkaline signature and tonalitic to monzogranitic composition (Paes de Barros 2007). They occur along narrow strips, in shear zones with NW-SE direction, surrounded by granitic and basic rocks or associated with N-S fault zones direction. SHRIMP U-PB zircon ages indicate crystallization ages at 1.99 Ga  $\pm$ 7 Ma (Alta Floresta gneiss, Souza *et al.* 2005) and 1.98 Ga  $\pm$ 7 Ma (Alto Alegre gneiss, Paes de Barros 2007) for the gneisses of granitic to tonalitic composition.

For rocks from the Cuiú-Cuiú suite, Santos *et al.* (1997) obtained similar ages (2 Ga  $\pm$ 7 Ma and 2.03 Ga). However Paes de Barros (2007) achieved Pb-Pb ages at 2.81 Ga  $\pm$ 4 Ma (gneiss Gavião), and Assis (2015) obtained SHRIMP U-Pb ages at 1.98 Ga  $\pm$ 8.8 Ma (gneiss Nova Guarita) and 1.97 Ga  $\pm$ 8.1 Ma (foliated biotite tonalite).

### 3.2.2. Pluto-volcanic calc-alkaline units and volcano-sedimentary sequences (1.97 - 1.78 Ga)

The pluto-volcanic units are formed by a series of granitic intrusions: Pé Quente suite (1.97 - 1.90 Ga; Assis 2011, Miguel-Jr 2011, Assis 2015) and Novo Mundo (1.96 Ga; Paes de Barros 2007), Flor da Mata, Aragão (1.93 Ga; Miguel-Jr 2011), Nhandu (1.87 Ga; Silva and Abram 2008) and Peixoto granites (1.79 Ga; Paes de Barros 2007).

Additionally, covering the basement is the Serra Formosa Vulcanoclastic Unit, while truncating the older plutons are the granodioritic suítes União, described by Assis (2008), Assis (2011), Assis *et al.* 2012, and dated by Miguel-Jr (2011) in 1.85 Ga (U-Pb), undifferentiated União do Norte, Colíder, Matupá (1.87 Ga; Moura 1998, Souza *et al.* 2005), União do Norte porphyry and Teles Pires. All this units host gold mineralization in the form of veins or disseminations with exception of the Flor da Mata and Peixoto granite. In general, these pluto-volcanic sequences have a calc-alkaline affinity, medium to high potassium, meta-luminous to slightly peraluminous and oxidized I-type granite, typical of volcanic arcs. Sequences dominated by volcanic and volcanoclastic rocks within these plutono-volcanic units are represented by the Serra Formosa Volcanoclastic Unit (1.72 Ga; Miguel-Jr 2011) composed of epiclastic rocks represented essentially by sandstones and gravackes, all of them with very fine granulometry to medium, as well as subordinate-supported matrix volcanoclastic sandy conglomerate lenses (Assis *et al.* 2012) and the Colíder suite (1.78 Ga; JICA/MMAJ 2000, Pimentel 2001, Silva and Abram 2008). The Colíder Suite (Silva and

Abram 2008) corresponds to high potassium calc-alkaline magmatism compatible with orogenic granite patterns. The lithotypes that composed this suite truncate all the previously defined units, or are in tectonic contact with the Nhandu and Matupá granite, being represented predominantly by subvolcanic and volcanic rocks and, to a lesser extent, pyroclastic and epiclastic rocks.

### **3.2.3. Anorogenic pluto-volcanic units (1.77 - 1.75 Ga)**

The Northern Union Porphyry (Assis 2011), intrusive in the Serra Formosa Vulcanoclastic Unit, corresponds to a subvolcanic unit that occurs in the form of laccoliths and composed of porphyritic alkali-feldspar granite of alkaline and anorogenic nature. Assis (2011) proposes a correlation between the Northern Union Porphyry and the sub-volcanic epizonal manifestations of the Teles Pires Intrusive Suite.

The Teles Pires Intrusive Suite (Santos 2000) comprises an association of plutonic and subvolcanic rocks of intrusive granitic composition in all previous older units. The suite is represented by batholiths and stocks consisting of porphyritic granite and biotite granite. The litho-geochemical data show characteristics of medium to high potassium, metaluminous to peraluminous A-type granite, corresponding to post-collision intrusions (Moreton and Martins 2005, Silva and Abram 2008).

### **3.2.4. Sedimentary sequences (1.44 Ga – Cenozoic)**

Sedimentary units cover all the previously defined units. Firstly, the Mesoproterozoic rocks of the Caiabis Group (Dardanelos Formation) composed of sandstone and quartz sandstone sequences of medium grain size with frequent levels of conglomerates with parallel and crossed flat stratification. These rocks are interpreted as alluvial fan systems by Moreton and Martins (2005) and as sediments from a pull-apart basin by Souza *et al.* (2005). U-Pb SHRIMP detrital zircon ages between 1.98 Ga  $\pm$ 4 Ma and 1.37 Ga  $\pm$ 13 Ma (Leite and Saes 2003) represent the maximum ages reported to this sedimentary sequence.

Finally, the Cenozoic periods are represented by alluvial and colluvial deposits, whereas the Tertiary and Quaternary by clastic and unconsolidated sediments (Souza *et al.* 2005).

GEOLOGICAL DOMAINS	GEOLOGICAL UNITS	AGES (Ma)	TECTONIC SETTINGS	REFERENCES
Sedimentary sequences	<b>Tertiary and Quaternary covers</b>	Quaternary	Intracratonic unconsolidated sediments	Souza <i>et al.</i> (2005)
	Clastic and unconsolidated politic sediments			
	<b>Caiabis group (Dardanelos Formation)</b>	1987 ±4 to 1377 ±13	Pull-apart or strike slip basin	Leite & Saes (2003); Souza <i>et al.</i> (2005)
	Sandstone			
A-type granites and related volcanic units	<b>Teles Pires Intrusive suite</b>	1782 ±17 to 1757 (U-Pb)	Post-orogenic (1.94 < TDM < 2.28; -3.4 < εNd(t) < +3)	Santos (2000), Pinho <i>et al.</i> (2001), Souza <i>et al.</i> (2005); Silva & Abram (2008)
	Alkali-feldspar granite, porphyritic granite, granophyre, rhyolite, rhyodacite, dacite, andesite, tuff, breccia and ignimbrite.			
	<b>União do Norte Porphyry</b>	1774 ±7.5	Post-orogenic *	Assis (2011); Miguel-Jr (2011).
	Porphyritic alkali-feldspar granite to monzogranite			
	<b>Colíder suite</b>	1786 ±17, 1785 ±6.3; 1781 ±8	Volcanic-arc to syn-orogenic setting (1.94 < TDM < 2.34; -3.4 < εNd(t) < +3)	JICA/MMAJ (2000), Silva & Abram (2008), Pimentel (2001)
	Intermediate to acid epiclastic, pyroclastic, subvolcanic and volcanic rocks.			
Calc-alkaline plutono-volcanic units (I-type granites)	<b>Peixoto granite</b>	1792 ±2 (Pb-Pb)	Syn-orogenic volcanic-arc *	Paes de Barros (2007)
	Biotite monzogranite, biotite granodiorite and biotite tonalite.			
	<b>União Granodioritic suite</b>	1853 ±23 (LA-ICP-MS)	Volcanic-arc granites *	Assis (2011); Miguel-Jr (2011)
	Biotite-hornblende granodiorite and biotite-hornblende tonalite.			
	<b>Undifferentiated União do Norte Granitic suite</b>	Unknown age	Volcanic arc granites *	Assis (2008)
	Syenogranite, monzogranite, syenite and quartz-monzonite.			
	<b>Matupá Intrusive suite</b>	1872 ±12 (Pb-Pb)	Syn-orogenic volcanic-arc (2.15 < TDM < 2.34; -4.3 < εNd(t) < +3.04)	Moura (1998), Souza <i>et al.</i> (2005)
	Biotite granite, biotite monzogranite, hornblende monzogranite, biotite-hornblende monzonite, hornblende monzodiorite, biotite-hornblende monzogranite, porphyritic biotite			

Calc-alkaline plutono-volcanic units (I-type granites)	Nhandu granite	1.889 ±17, 1.879 ±5.5 (U-Pb) and 1.848 ±17	Syn-orogenic volcanic-arc (2.14 < TDM < 2.17; εNd(t) = -0.91)	Moreton & Silva (2005); Silva & Abram (2008), JICA/MMAJ (2000)
	Syenogranite, monzogranite with subordinate subvolcanic.			
	Aragão granite	1.931 ±12 (U-Pb)	Volcanic-arc *	Vitório (2010), Miguel-Jr (2011), Ramos (2011)
	Syenogranite, monzogranite with porphyritic and micro granite facies.			
	Flor da Mata granite	Unknown age (correlated to the Novo Mundo granite)	Volcanic-arc *	Ramos (2011)
	Alkali-feldspar granite, syenogranite, monzonite, granodiorite.			
	Novo Mundo granite	1.970 to 1.964 (U-Pb and Pb- Pb)	Syn-orogenic volcanic arc (2.55 < TDM < 2.76; -7.62 < εNd(t) < - 4.48)	Paes de Barros (2007)
	Syenogranite, monzogranite, granodiorite, quartz-monzonite and monzonite.			
	Pé Quente Intrusive suite	1.979 ±31 (U-Pb) to 1.901 ±6.8 (U-Pb)	Volcanic-arc *	Assis (2011), Miguel-Jr (2011), Assis (2015)
Monzonite, quartz-monzonite, quartz- monzodiorite, monzodiorite, fine-coarse albitite, aplitic granodiorite and biotite tonalite.				
Serra Formosa Volcaniclastic Unit	Maximum age: 2009, Minimum age: 1718	Back-arc foreland basin within an active continental margin *	Assis (2011), Miguel-Jr (2011)	
Feldspathic-sandstone, feldspathic-wake, lithic-sandstone and matrix supported sandy-polymictic conglomerate.				
Basement rocks	Foliated granitoids	1.998 (Pb-Pb) to 1.978 ±8.1(U-Pb)	Volcanic-arc *	Paes de Barros (2007), Assis (2015)
	Quartz diorite, tonalite, granodiorite.			
	Gneisses and migmatites	2.816 ±4 (U-Pb) to 1.980 ±8.8 (U-Pb)		Souza et al. (2005), Paes de Barros (2007), Assis (2015)
	Anfibolite and monzonitic, tonalitic and granitic orthogneiss, partly migmatite.			

**Table 1:** Main geological units, geochronology and tectonic environment of the eastern sector of the AFMP (Taken from Trevisan 2015; modified from Assis 2015). \*Not available isotopic data.

### 3.3. Tecto-magmatic evolution of AFMP

Based on intrusion relationships, geochemistry and geochronology, Assis (2015) proposed that the evolution of felsic magmatism in the eastern sector of the AFMP was developed in three Paleoproterozoic magmatic events separated by approximately 311 Ma (Fig. 4):

(i) Orosinian: Represented by the granitic basement rocks like Nova Guarita gneiss and foliated tonalite with ages between 1.980 to 1.970 Ma, and correlated with the Cuiú-Cuiú complex (1.98 – 2.03 Ga; Santos *et al.* 1997, Paes de Barros 2007, Assis 2015), Novo Mundo granite (1.95 – 1.97 Ga; Paes de Barros 2007) and Pé Quente monzonite (1.97 Ga; Miguel-Jr 2011).

(ii) Late Orosinian (1.931 to 1.878 Ma), which includes the Aragão granite (1.93 Ga; Miguel-Jr 2011), X1 granodiorite (1.904 Ma; Assis 2015), Pé Quente tonalite (1.901 Ma; Assis 2015), Nhandu granite (1.88 – 1.87 Ga; Paes de Barros 2007), besides the Matupá (1.87 Ga; Moura 1998, Silva 2014), União Granodioritic (1.85 Ga; Miguel-Jr 2011) and Juruena (1.82 – 1.81 Ga; JICA/MMAJ 2000) suites.

(iii) Statherian (1.782 to 1.727 Ma) includes the Peixoto granite (1.79 – 1.76 Ga; Paes de Barros 2007, Silva 2014), Teles Pires Intrusive (1.79 – 1.75 Ga; Santos 2000, Pinho *et al.* 2003) and Colíder (1.78 Ga; Pimentel 2001, Silva and Abram 2008) suites, besides the União do Norte (1.774 Ga; Miguel-Jr 2011) and X1 quartz-feldspar (1.773 Ma; Assis 2015) porphyries. The last two are included in the Teles Pires and Colíder suites, respectively.

In addition, geochemical of major and traces elements, isotopic and geochronological data, suggest for the petrogenesis of the rocks of the AFMP eastern sector, a neoarchean to paleo-proterozoic magmatic source, derived from a metasomatized mantle that remained in the crust and evolved through the combination of fractional crystallization and subordinate cortical contamination (Assis 2015).

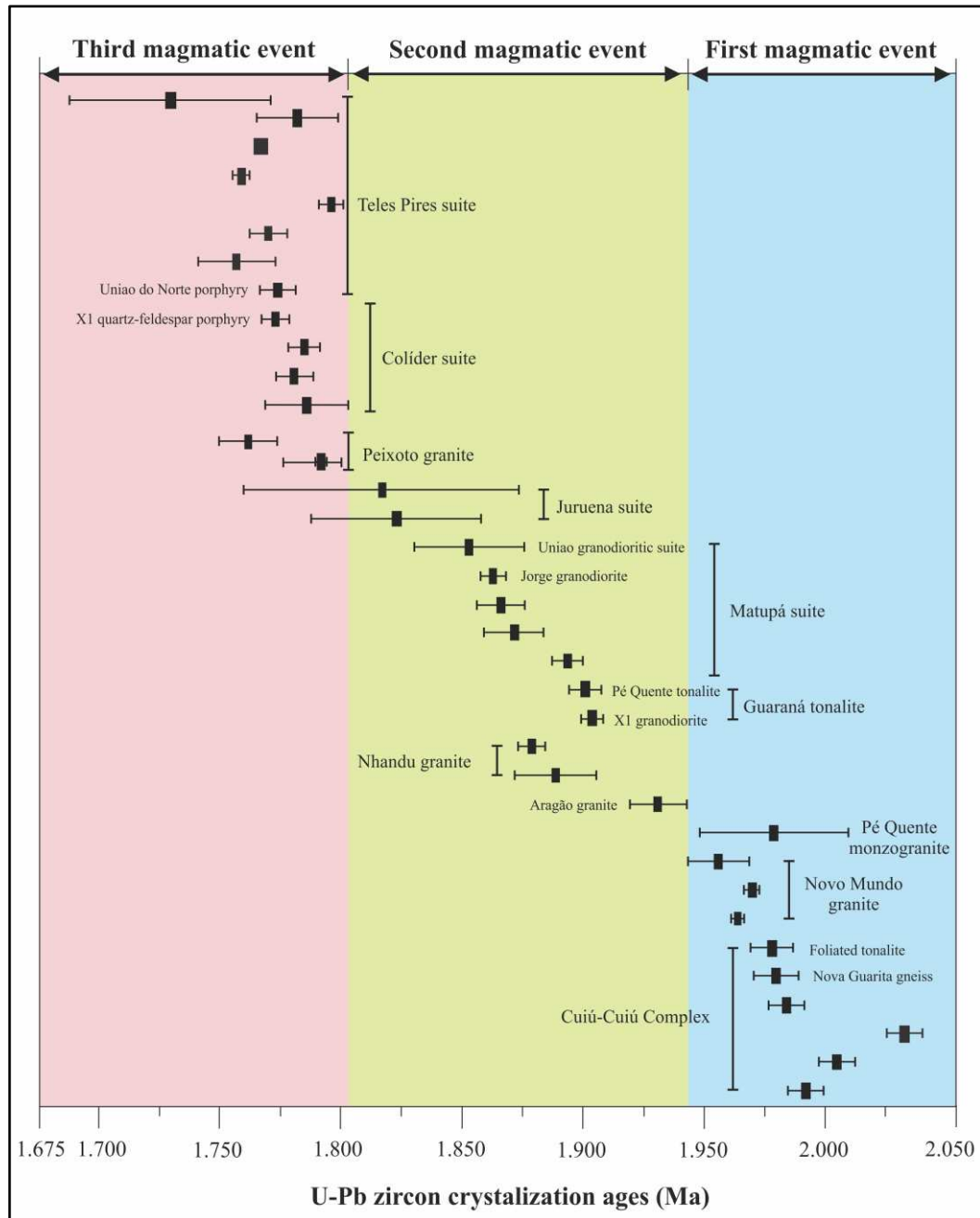


**Figure 4:** Crystallization ages of the main Paleoproterozoic intrusive bodies of the eastern sector of the AFMP based on U-Pb data in zircons (Assis 2015).

Regarding the tectonic regime of the AFMP, several models have been proposed over the last years to explain the felsic plutono-volcanic events that take place in the Amazonian craton: (i) Within-plate magmatism model (Neder *et al.* 2002); (ii) Post-collisional extensional magmatism model (Lamarão *et al.* 2002, Barros *et al.* 2009, Assis 2011, Assis *et al.* 2012) and (iii) Accretionary arc magmatism model (Tassinari and Macambira 1999, Santos 2000, Assis 2011, Assis 2015). Within this context, there is a significant consensus that the most granitic rocks in the province were built up during several

magmatic arcs over the Paleo and Mesoproterozoic collision (Tassinari and Macambira 1999, Cordani and Teixeira 2007, Souza *et al.* 2005, Silva and Abram 2008). Taking these arguments into account, Assis (2015) propose a tecto-magmatic division following the accretion model of volcanic arcs in three main stages: i) stage 1: Magmatic Arc, chronologically correlate to the development of the Cuiú-Cuiú magmatic arc (2.1 - 1.95 Ga); ii) stage 2: Juruena Magmatic Arc (1.9 - 1.8 Ga); and iii) stage 3: post-orogenic phase of Juruena Magmatic Arc (1.78 - 1.75 Ga).

The stage 1 (2.1 - 1.95 Ga) is related to the development of the Cuiú-Cuiú magmatic arc, with gneiss and tonalite generation belonging to the Cuiú-Cuiú suite, 2.03 - 1.98 Ga (Santos *et al.* 1997, Paes de Barros 2007, Assis 2015). These gneisses were generated at deep crustal levels under high P and T conditions from calico-alkaline granitic I-type magmas. On the other hand, the tonalite represents an I-type felsic magmatism developed at shallower crustal levels and with low P and T conditions. These units may represent a geodynamic evolution from a platform with a volcanic arc, where crystallized the basement rocks, to subsequently metamorphosed gneiss, and foliated granitoids and finally to a more evolved setting, with subsequent emplacement of not-metamorphosed granitic plutons, like Pé Quente monzonite and Novo Mundo granite. Additionally, according to Assis (2015), this stage can be related to the development of the Ventuari-Tapajós volcanic arc (1.95 - 1.8 Ga) according to the Tassinari and Macambira (1999) model.

The stage 2 (1.9 - 1.8 Ga) is related to the phase of greater crustal thickening, with the construction of the Juruena Arc and can be related to the second magmatic event, which is also responsible for production of a very large amount of plutonic and volcanic sequences represented by the Pé Quente tonalite (1.9 Ga  $\pm$  6.8 Ma, Assis 2015), biotitic granodiorite X1 (1.9 Ga  $\pm$  4.6 Ma, Assis 2015), Jorge granodiorite (1.86 Ga  $\pm$  4.8 Ma, Assis 2015), Nhandu Granite (1.88 Ga  $\pm$  17 Ma to 1.87 Ga  $\pm$  5.5 Ma, Silva and Abram 2008), and also the intrusive suites Matupá (1.87 Ga  $\pm$  12 Ma; Moura 1998), Juruena (1.82 Ga  $\pm$  35 Ma to 1.81 Ga  $\pm$  17 Ma, JICA/MMAJ 2000) and Paranaíta (1.81 - 1.79 Ga; Santos *et al.* 2000). In addition, all these units also represents an evolution of the tectonic environment, from an initial production of magmatism at the beginning of the volcanic arc, represented by the Guarantã granite (tonalite to granodiorite composition), towards a more stable platform with generation of more evolved felsic magmatism (Matupá and Paranaíta suites), and according to Assis (2015) that would be related to the construction of the Rio Negro-Juruena arc (1.8 - 1.55 Ga) in the Tassinari and Macambira (1999) model. However, the older plutons (e.g Pé Quente tonalite, X1 biotite granodiorite, Jorge granodiorite and Nhandu granite) would be

associated with Ventuari - Tapajós arc (1.95 - 1.8 Ga; Tassinari and Macambira, 1999), while Paranaíba and Matupá suites would be restricted to the youngest volcanic arc (1.8 – 1.55 Ga).

The stage 3 (1.78 – 1.75 Ga) is related to a more stable platform, evolving from a post-collisional environment to a within-plate environment, with volcanic units to sub-volcanic porphyries. The system begins with a felsic, type I magma, with continental affinity and with anorogenic magmas of the Colíder Suítes (1.78 Ga; Pimentel 2001) and Teles Pires (1.79 - 1.75 Ga, Santos *et al.* 2000). After the crustal thickening peak, an extensional phase begins, in this way the asthenosphere rises and melts the lower crust generating alkaline granitic A-type magmas, represented by the União do Norte porphyry. According to Assis (2015), this occurred during a post-orogenic period associated with the Rio Negro-Juruena event after its amalgamation with the Ventuari Tapajós province, based on the Tassinari and Macambira (1999) model.

### **3.4. Metalliferous deposits in the eastern sector of the AFMP**

There are several metalliferous deposits and occurrences within the AFMP. Most analysed cases in the last two decades suggest that these deposits are mainly hosted in granitic intrusions and volcanic-volcaniclastic sequences. Most of them are mainly located in the eastern sector of the AFMP and are represented by vein-type deposits. However, in the last two decades, several disseminated deposits have also been studied by companies and academic entities (Assis 2006, Paes de Barros 2007, Assis 2011, Miguel-Jr 2011, Trevisan 2012a, Trevisan 2012b, Rodrigues 2012, Assis 2015, and Trevisan 2015).

The metalliferous deposits located in the AFMP eastern sector, are mainly divided into four groups: i) Disseminated Au  $\pm$  Cu; ii) Au  $\pm$  Cu vein-type, iii) Au + Zn + Pb  $\pm$  Cu vein-type in fragile domain, and iv) disseminated Cu + Mo  $\pm$  Au mineralizations. The first two groups are represented by the Pé Quente, Luizão, Basílio, Dionísio, X1, Serrinha and Paraíba deposits, the third one by Bigode, Francisco and Luiz Bastos. The fourth group is represented by Ana, Jaca and the Paraíba deposits. In this work, only the Paraíba deposit would be described in detail in the next topics.

### **3.5. Metallogenic models of Au $\pm$ Cu, Cu $\pm$ Mo and Au $\pm$ base metal deposits of the AFMP eastern sector.**

According to Paes de Barros (1994), Siqueira (1997), Groves *et al.* (1998), Madruci (2000), Santos *et al.* (2001), Moreton and Martins (2003) and Paes de Barros (2007), most of the Au  $\pm$  Cu deposits within the AFMP, including the Paraíba, show typical

characteristics of orogenic gold deposits based on Kerrich and Cassidy (1994) recommendations: (i) vetiform units hosted in fractures associated with shear zones, (ii) are syn-cinematic and generally located in sub-vertical faults, (iii) restricted hydrothermal halos, (iv) generally associated with transitional ductile/fragile zones, (v) an assemblage dominated by quartz, carbonate, mica, albite, chlorite, epidote and pyrite, (vi) metals associated with Au include Ag, As, Sb, Bi and Te, (vii) fluids inclusions with low salinity (<5 wt% NaCl), high CO<sub>2</sub> + CH<sub>4</sub> contents from 5 to 30 mol% and also with aquo-carbonatics immiscible phases albite, chlorite, epidote and pyrite.

On the other hand, the disseminated gold-rich deposits from AFMP, cluster several important deposits, that according to Paes de Barros (2007), the Au ± Cu (± Bi ± Te ± Mo ± Ag) disseminated deposits of the AFMP eastern sector also show certain similarities with Au deposits associated with intrusive systems (IRGS: intrusion-related gold systems; Thompson *et al.* 1999, Lang and Baker 2001), given by: (i) gold-bismuth association, (ii) ore minerals: pyrite ± chalcopyrite ± galena and sulphosalts, (iii) coexistence of aqueous bi-phase and aquo-carbonatic fluid inclusions, (iv) vetiform mineralization style and (v) restricted hydrothermal system. Additionally, Santos *et al.* (2001) proposed that the structurally-controlled Au ± Cu deposits of the AFMP show similar characteristics of mesothermal type and intrusion-centered deposits (Sillitoe 1991) or intrusion-related (Sillitoe and Thompson 1998).

On the other hand, Moura *et al.* (2006) proposed that the Serrinha deposit (Moura 1998) shows similar characteristics to the porphyry-type deposits, according to petrologic, mineralogic, isotopic and fluid inclusion evidence (Corbett and Leach 1997, Seedorff *et al.* 2005, Sillitoe 2010). Assis (2015) proposed that the Pé Quente, Xi and Luizão Au ± Cu disseminated deposits are also associated with porphyry style even though with some characteristics that differs from the classic Andean porphyries. Based on field data and petrographic, geochemical and fluid inclusions evidence, Trevisan (2015) proposed an intrusion-hosted gold-quartz vein system classification for the Paraíba deposit.

Metals such as Cu, Mo, Au, Sn, and W form important mineralizations spatial and genetically associated with felsic intrusions in the upper-crust. Fluid saturation during the magma crystallization mobilize and concentrate metals in magmatic-hydrothermal systems and could generate Cu-Mo-Au and Sn-W porphyry-type deposits (Sillitoe 2010). The presence of disseminated Cu + Mo ± Au mineralizations at the Paraíba deposit is interpreted as a magmatic-hydrothermal system, developed from the intrusion of an igneous sub-volcanic

porphyry rock, considered the source of fluids, heat and metals and which is overlapping an Au  $\pm$  Cu metamorphic-hydrothermal system.

Assis (2011) suggest that the Au + base metals (Zn + Pb  $\pm$  Cu) deposits (Bigode, Francisco and Luiz Bastos deposits) are associated to an intermediate sulphidation epithermal genesis according to its proximity to sub volcanic felsic rocks, vetiform mineralization style, its mineral assemblage, and textures.

## 4. ANALYTICAL PROCEDURES

### 4.1. Field trip

The field trip was carried out between 4th-26<sup>th</sup> July, 2017. It comprised observation of the main rock outcrops of the area surrounding the Peixoto de Azevedo city, plus sampling of surface samples and measuring structural data at the Paraíba open pit and nearby areas. Geological units and hydrothermal alteration zones were identified, described and charted from 1,800 m of core logging (boreholes BH020, BH041 and BH059), which are representative of a main cross section of the Paraíba deposit (Fig. 5).

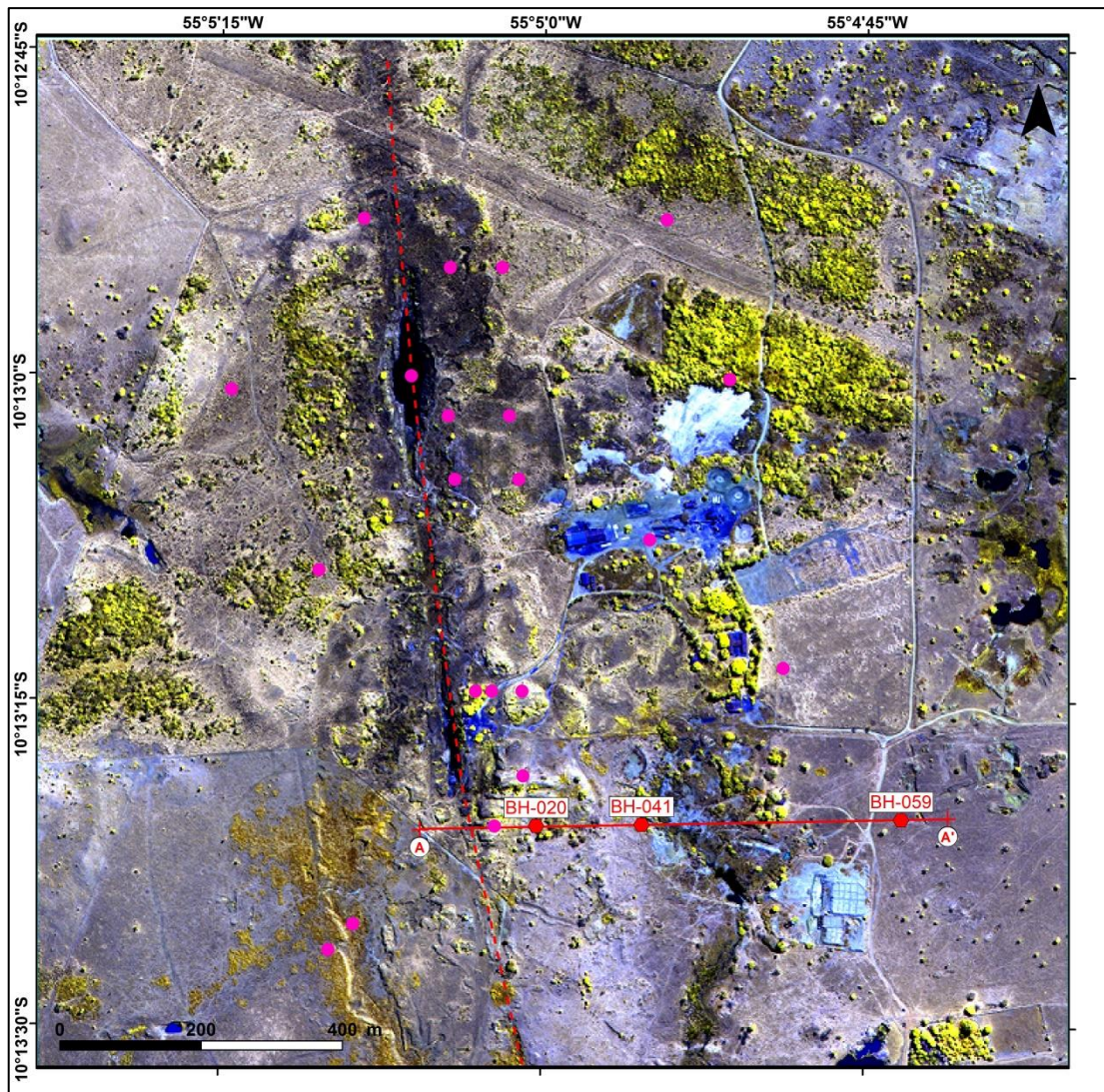


**Figure 5:** Satellite Worldview 2 false colour composite (bands 873 in RGB) image of the Paraíba deposit (axis of the ore bodies marked by dashed red line) showing the location of boreholes BH020, BH041 and BH059, which compose an archetype cross section of the deposit (line A-A'). Purple circles correspond to other and also some exploratory boreholes. Inactive open-pits, currently flooded, can also be spotted in the image. Colours in the image can be interpreted as follows: yellow pixels correspond to vegetation; black to water, light blue to humid crops, white to exposed soil and blue to mining infrastructure.

## 4.2. Reflectance spectroscopy

Spectroscopy is the study of light as a function of wavelength that has been emitted, reflected, or scattered from a solid, liquid, or gas. Minerals, rocks and other terrestrial compounds, like hydrocarbons, exhibit diagnostic absorption features in either the VNIR (400 - 1.000 nm), SWIR (1.000 - 2.500 nm), MIR (3.000 - 5.000 nm), and/or LWIR (8.000 - 14.000 nm) regions due to electronic and vibrational processes, as well as overtones and combinations (Farmer 1974, Hunt 1977, Clark and Roush 1984, Gaffey *et al.* 1993, Hapke 1993, Clark 1999, Hook *et al.* 1999).

As a fundamental part of this work, 1,400 point spectral measurements were made along boreholes (BH) 020, 041, 059 (Fig. 5) with an ASD-FieldSpec® 3 Hi-Resolution spectroradiometer, spaced of 1.3 m, approximately. The spectra collected with this instrument will be called from here onwards as “ASD spectra” to differentiate it from those obtained from SisuCHEMA hyperspectral images (here coined as “SisuCHEMA spectra”). This instrument records spectra with 2,151 bands, at a spectral resolution of 3 nm to 8.5 nm in the VNIR and 6.5 nm in the SWIR wavelength regions, and sampling intervals of 1.4 nm (VNIR) and 2 nm (SWIR). The spectra were obtained using a contact probe of 20 mm diameter with an internal illumination source. The collected spectra were analysed and interpreted at the IG/UNICAMP facilities. The first step was to observe the shape and position of the absorption features, then the mineralogy was identified with the assistance of ENVI® and TSG™ 8 software. Secondly, using spectral libraries as USGS (Clark *et al.* 1993) and GMEX guides (Pontual *et al.* 2008), there were created quantitative parameters that allowed to determine the abundance, composition and structural ordering (crystallinity) of the minerals that composed the different hydrothermal alteration zones.

This study focuses on 1300 to 2500 nm spectral region because white mica, chlorite, biotite, phlogopite, carbonate and epidote absorption features are located mainly in the SWIR. The principal absorption features are between 2200 and 2400 nm, caused by a metal-(OH) coupling (Clark 1999). In this range, the main characteristic features of certain minerals are at 2200, 2250, 2350 and 2380 nm (Pontual *et al.* 1997). Besides, there exist two features related to water overtones at 1400 and 1900 nm (Fig. 6).

### 4.2.1. White Mica

White mica is identified in spectra by Al-OH absorptions at ~2200 nm, associated with features at around 1410 nm (OH bonds), 1900 nm (H<sub>2</sub>O bonds), and 2240 nm (Al-OH secondary features). The 2200 nm characteristic wavelength is due to the combination of

vibrations caused by stretching and flexion as a response of a Tschermak substitution in the octahedral position from Al-rich (Si-poor) white mica (paragonite and muscovite) to Al-poor (Si-rich) phengite (Velde 1965, Clark *et al.* 1990, Duke 1994, Bishop *et al.* 2008). This substitution implies an exchange given by  $(\text{Al}^{\text{IV}}, \text{Al}^{\text{VI}}) = \text{Si} [\text{Mg}, \text{Fe}^{2+}]$  where  $\text{Al}^{\text{IV}}$  is substituted by Si, and  $\text{Al}^{\text{VI}}$  by Mg and Fe. This substitution can increase the principal absorption wavelength. The white mica composition can vary from 2184 nm, typically associated with the most Na-rich (paragonite), through 2200 nm (muscovite) and up to 2225 nm, generally associated to Fe-Mg and Si substitution (phengite). Besides, the intermediate values are designated as ‘tending to’ paragonite (2190 nm) and ‘tending to’ phengite (2214 nm) (Pontual *et al.* 2008).

The crystallinity is a qualitative term used to refer to the disturbance of order and periodicity of crystalline materials (Guggenheim *et al.* 2002). In practice, the crystallinity is defined as the degree of perfection of translational periodicity as determined by some experimental method. The crystallinity index (CI) can be determined using reflectance spectroscopy, by rationing the depth of Al-OH feature at 2200 nm with the water absorption feature at 1900 nm (Pontual *et al.* 2008). This index not only shows the white mica crystallinity but also the mixture proportion of white mica (illite) and smectite interstratifications. Crystallinity is a spectral parameter commonly used as a proxy for the evolution of (dioctahedral) phyllosilicates during increasing temperature (Cudahy *et al.* 2008). It is also used to describe changes in water content and other processes that take place during the evolutionary sequence. Besides, the white mica abundance was calculated measuring the depth of the 2200 nm principal feature (Pontual *et al.* 2008).

#### 4.2.2. Chlorite

The chlorite composition can be determined through the two main diagnostic absorptions occurring between 2240 - 2270 nm associated with FeOH, and between 2310 - 2370 nm associated with Mg-OH. The wavelengths of these absorptions vary with composition, from the shortest wavelengths for the most magnesian-rich chlorites to longer wavelengths as the proportion of iron increases. For Mg-rich chlorite, the range varies between 2325 and 2332.5 nm, Mg-Fe chlorite from 2332.5 to 2340 nm, Fe-Mg chlorite from 2340 to 2347.5 nm and Fe-rich chlorite between 2347.5 and 2355 nm (Pontual *et al.* 2008). In chlorite with intermediate composition, the 2250 and 2350 nm features do not have equal depths, and the 2250 nm absorption peak appears to be smaller (Pontual *et al.* 1997, Clark *et al.* 2007).

#### 4.2.3. Biotite

The biotite can be determined from the 2255 and ~2350 nm features, related to Fe-OH and Mg-OH bond, respectively. Besides, it can be identified by a negative slope between 1700 and 1900 nm due to the strong influence of  $\text{Fe}^{+2}$  content. In addition, the biotite can be recognized by features at ~900 and ~1165 nm. The 'peak' between the two biotite main absorption features usually sits higher relative to the hull than for chlorites. For its part, the phlogopite presents an absorption feature at ~2244 nm due to the Fe-OH bond that is not always present. The main feature is located at ~2325 nm and the secondary at ~2380 nm both related to the Mg-OH content (Pontual *et al.* 2008).

#### 4.2.4. Epidote

The epidote has a large number of absorptions, many of which are shared with other minerals. For example, features located at ~2256 nm (due to Fe-OH) and ~2335 nm can overlap in mixtures with chlorite and carbonate. For a correct classification, it is used the diagnostic features related to the OH bond located at ~1545 and ~1830 nm (Pontual *et al.* 1997). Using the spectral variation of the ~1545 nm feature, it is possible to determine the composition within the epidote-clinozoisite solid solution (Roache *et al.* 2011).

#### 4.2.5. Calcite

Calcite is a common mineral in mixtures, especially in propylitic alteration. It is represented by a simple and asymmetric diagnostic feature, located between 2340 and 2345 nm and usually superposed with other minerals like chlorite and epidote. Besides, calcite presents other two absorptions at 1880 and 1892 nm, but they are not usually present in mixtures.

#### 4.2.6. Actinolite

Actinolite presents a double absorption peak at ~2301 and ~2314 nm, and a secondary diagnostic peak at 2384 nm due to the Mg content. Besides, it presents a diagnostic feature at ~2217 that separates it from talc and a drop in reflectance between 1500 and 1900 nm related to the  $\text{Fe}^{+2}$  content, which separates it from tremolite.

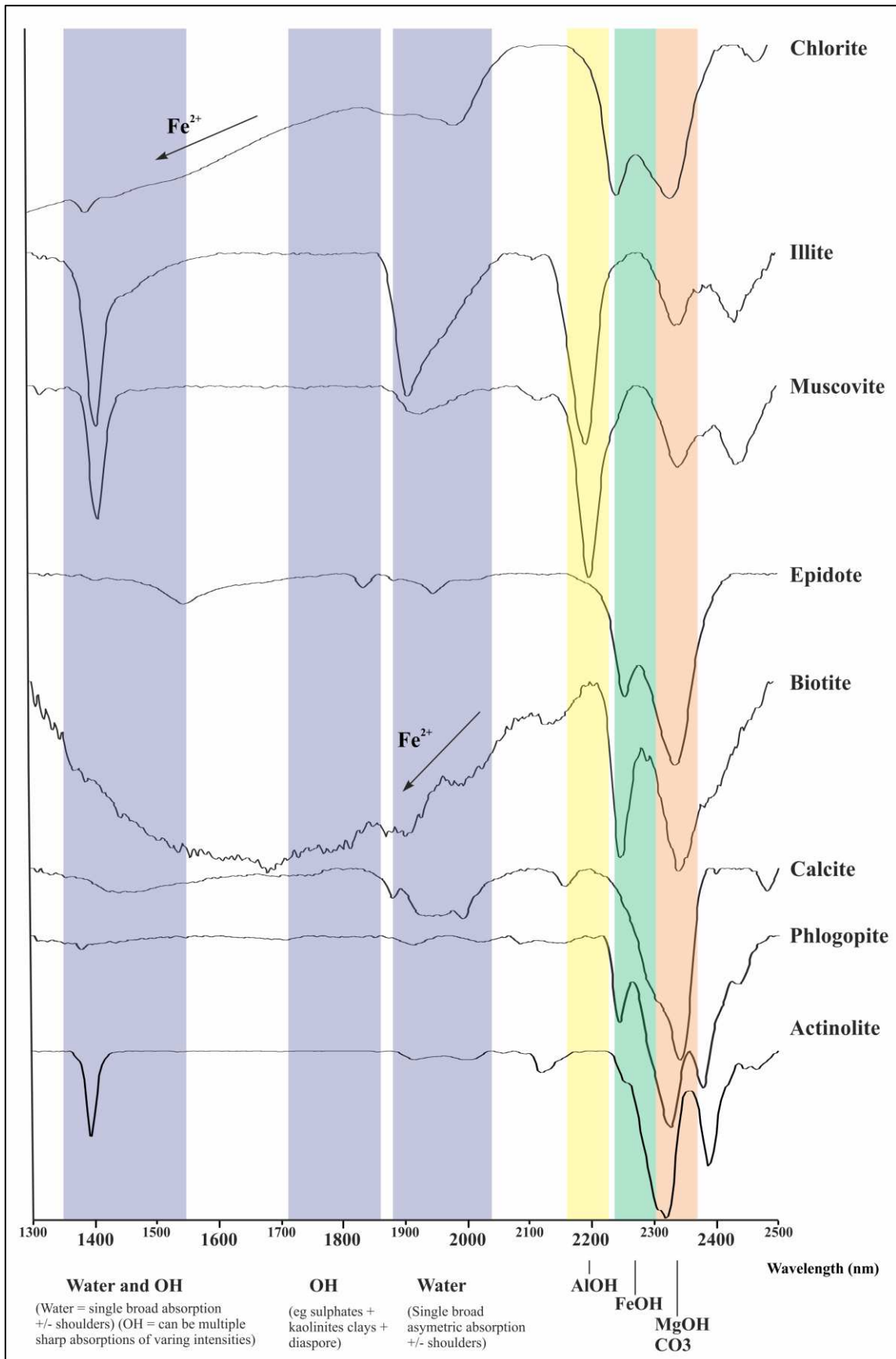


**Figure 6:** Major spectral absorption bands in the SWIR (Pontual *et al.* 2008).

### **4.3. Petrography**

Petrographic studies with transmitted and reflected light were carried out in the Microscopy Laboratory of the Institute of Geosciences, UNICAMP, from 16 thin sections. Additionally, pre-existing petrographic thin sections, used by Trevisan (2015), were also analysed aiming to compare and increase the quantity and quality of information concerning the deposit. There were used to define: (i) types, styles and spatial and temporal distribution of the hydrothermal alteration zones; (ii) ore and its relation to gangue minerals, as well as its temporal, spatial and genetic relationship with host rocks and hydrothermal alterations; (iii) compositional and textural variations in phyllosilicates such as biotite, phlogopite, chlorite and muscovite among others. The photographs of the thin sections were obtained with a Sony Cybershot camera (12 megapixels resolution) attached to the microscope.

### **4.4. Scanning electron microscope (SEM)**

The SEM analyses were performed in the scanning electron microscopy laboratory of the IG-UNICAMP. This type of study was carried out with aiming (i) to clarify the compositional and textural differences of minerals of high exploratory value like muscovite, biotite, phlogopite and chlorite, found both with reflectance spectroscopy and petrographic analysis; (ii) to determine the characteristics of the hydrothermal halos, particularly those associated with sulphides-rich quartz veins that could not be recognized with a conventional petrographic microscope; (iii) to characterize the ore minerals disposition and their approximate chemical composition; (iv) to identify the textural relationships between ore and gangue minerals. The equipment used was a Leo 430i Oxford with digital scanning coupled to a dispersive energy spectrometer (Energy Dispersive X-Ray Spectrometer, EDS - Oxford Instruments). The operating conditions of the equipment were the following: acceleration voltage 20 kV; focal length of 19 mm and an electric current flow of approximately 3 nA.

### **4.5. Mineral chemistry**

Chemical analyses on chlorite, white mica, biotite, phlogopite and epidote were made in representative samples from mineralized zones. The purpose of this stage was: (i) to classify these minerals and determine their composition; (ii) cross-compare the chemical compositions in different hydrothermal alteration zones; and (iii) delimit crystallization temperature intervals in chlorite (geothermometer), aiming to understand the physical-chemical formational conditions of the Parafba deposit.

These analyses were carried out in 8 thin sections using the Electron Microscope Analyzer (EMPA) in the Geosciences Institute, São Paulo State University (UNESP). It was employed the Wavelength Dispersive Spectroscopy (WDS) method in a JEOL JXA-8230 electronic microprobe using model JEOL JXA-8230 with standard operational conditions, as shown in Table 2. Before the analyses, the thin sections were metalized with a carbon film of 10 nm.

Parameter	JEOL JXA-8230
Mineral (deposit)	Chlorite, Muscovite and Biotite
Accelerating voltage (kV)	15
Probe current (nA)	19.5
Beam diameter (µm)	10

Standard	
Al	biotite
Si	biotite
Fe	biotite
K	biotite
Ti	biotite
Na	kaersutite $[\text{NaCa}_2(\text{Mg}_4\text{Ti})\text{Si}_6\text{Al}_2\text{O}_{23}(\text{OH})_2]$
Mg	kaersutite $[\text{NaCa}_2(\text{Mg}_4\text{Ti})\text{Si}_6\text{Al}_2\text{O}_{23}(\text{OH})_2]$
Cl	tugtupite $[\text{Na}_4\text{AlBeSi}_4\text{O}_{12}\text{Cl}]$
Ca	chlorite
Cr	chlorite
Ni	chlorite
Mn	manganese-rich willemite
Ba	barium sanidine
Rb	pollucite $[(\text{Cs}, \text{Na}, \text{Rb})_2\text{Al}_2\text{Si}_4\text{O}_{12} \cdot (\text{H}_2\text{O})]$

**Table 2:** Operational conditions and standards used in the EMPA.

#### 4.6. Imaging Spectroscopy on Drill Core Samples

Some representative drill core samples, in which thin sections were created, were also scanned using a SisuCHEMA hyperspectral imaging system, aiming to analyse in detail the mineral variability. This camera generates images in the wavelength range between 928 and 2524 nm with 256 channels and a spatial resolution of 156 x 156 and 30 x 30 µm.

The pre-processing stages consisted of (i) mask creation with the aim of eliminating unwanted sectors of the samples, and (ii) elimination of bands with noise or non-coherent data at the beginning and the end of the spectra. The processing was based on the procedure described in detail by Boardman (1993), Boardman *et al.* (1995), and Boardman and Kruse (2011), and implemented in ENVI® as the “Spectral Hourglass” tool. The hourglass processing uses the nature of hyperspectral data to find the most spectrally pure, or spectrally unique, pixels (named endmembers) within the dataset and determine their

locations. It is possible to visualize the data in n-D space and cluster the purest pixels into endmembers, and optionally supply your own endmembers.

The Spectral Hourglass uses a sequence of processing steps. Firstly, the minimum noise fraction (MNF) is computed (Green *et al.* 1988). This method applies a principal component analysis to eliminate the correlation between the original bands and the generated eigenimages (MNF bands). With this process, two groups of images are generated; one dominated by noise, which is discarded, and another with coherent images, on which the "pixel purity index" (PPI) (Boardman *et al.* 1995) was applied to find and select those pixels that are spectrally diverse (i.e., potential endmembers). Subsequently, the purest pixels are selected as endmembers with the aid of "n-dimensional" interactive dispersion diagrams (where n is equal to the number of selected MNF bands) (Boardman 1993, Boardman *et al.* 1995), where the spectral signatures are defined selecting the most extreme points of the data cloud. The Spectral Angle Mapper (SAM) method, which uses an n-D angle to compare the pixels with the reference spectra was also employed to generate compositional maps, using spectral libraries created from ASD-measured spectral endmembers.

Additionally, some SisuCHEMA images were processed with the ENVI's module MMTG A-List Hyperspectral Data Processing Software (CSIRO; Mason 2002) for mapping the wavelength of some absorption features (ex. Al-OH). Besides, SisuCHEMA images were also used to compare and validate white mica and chlorite principal absorption features with their respective mineral chemistry, acquiring point spectra at the same location where microprobe measurements were made, allowing the comparison between mineral chemistry and spectral response.

## 5. PARAÍBA DEPOSIT

### 5.1. Main features

Paraíba is a key Au + Cu vein-type deposit within the AFMP. It was discovered in the 1970's and is located 12 km to the west of "Peixoto de Azevedo" city. The deposits has been studied by several authors: Abreu Filho *et al.* (1992), Paes de Barros (1994), Siqueira (1997), Souza *et al.* (2005), Moreton and Martins (2005), Assis (2006), Silva and Abram (2008), Trevisan (2015) and Bartolomeu (2016).

The mining activity has developed from artisanal mining until obtaining in 1990 the mining concession by the National Department of Mineral Production (NDMP), on behalf of the Cooperativa Mista de Garimpeiros Produtores de Ouro do Vale do Rio Peixoto Azevedo – COOPERXOTO. Until now, only the vein-type areas have been mined, which were initially exploited as an open pit reaching a depth of 30 m approximately (Fig. 7a and b) (Siqueira 1997). Later, the mine was developed underground through a gallery of 300 m in N-S direction with access through a 100 m shaft (Fig. 8a and b). Actually, it is in possession of P.A. Gold Mineração private company, which is carrying out exploratory activities.

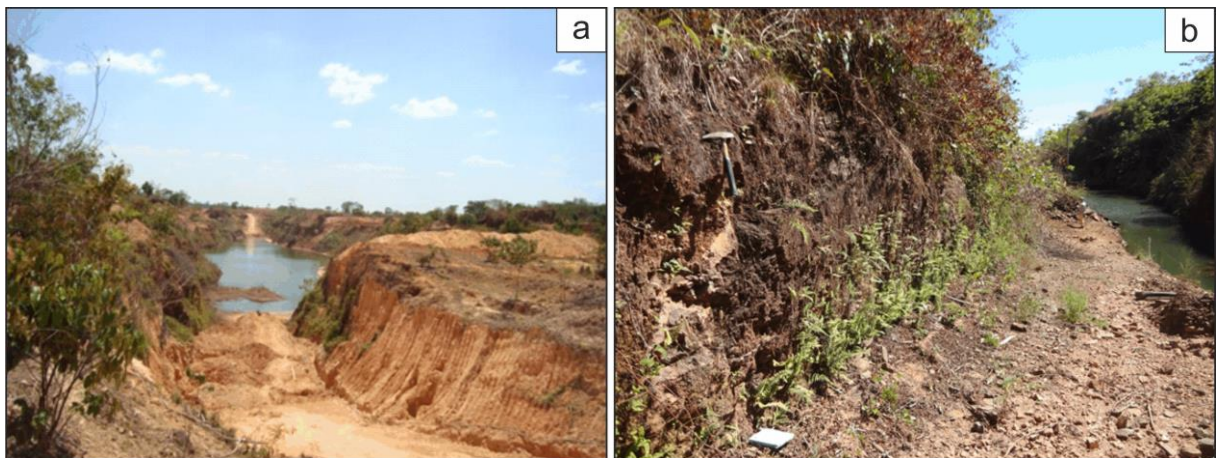


**Figure 7:** a-b) Current open-pit photographs that were exploited to an approximate 30 meters depth and that are currently flooded.

Siqueira (1997) describes the presence of (i) milonitized tonalite with quartz porphyroclast, (ii) tonalite to granodiorite, (iii) magnetic amphibolite enclaves, and (iv) granitic dykes. Core logging data and gallery mapping show that the principal quartz-vein (Filão do Paraíba) and the secondary vein (Paraibinha) are usually restricted to the mylonitized zones. According to Trevisan (2015), the principal veins are in contact with a pervasive and intracrystalline biotite-potassic alteration zone, which are enveloped by

chloritic and sericitic alteration halos. For more distal zones this author defined a potassic alteration zone with K-feldspar, a spatially restricted propylitic alteration and late veins with varied composition.



**Figure 8:** a) Gallery photograph, currently flooded. b) Location of the shaft and elevator for transporting material and workers during the operation time of the mine.

The principal mineralized zone is composed of three lenticulars and branched sulphides-gold-rich quartz veins with approximately 1,500 m in length and hosted in a N05W/65-70E ductile/brittle shear zone. The main vein, with a thickness of 0.3 - 1.5 m., presents 1 to 3 cm gold-rich pyrite bands. According to Paes de Barros (1994), the Paraíba deposit has veins sub-parallel to a dextral and antithetical shear zone, with a dip of 70-90°E, characterized by an intense mylonitic foliation with an attitude between N05-15W. Besides, the Paraíba deposit presents Cu and Mo-rich hydrothermal alteration areas that have not been exploited by the company yet.

The veins zones mineralization is represented principally by pyrite, chalcopyrite, magnetite, bismuthinite and bismuth, and subordinated galena, chalcocite, bornite and covellite (Silva and Abram 2008, Trevisan 2015). According to Paes de Barros (1994), the Au (Ag = 13,24 a 17 wt%) occurs as subrounded aggregates in pyrite and subordinate in the chalcopyrite. The disseminated Cu and Mo mineralization are associated with high propylitic alteration areas and also with intense epidotization zones.

## 5.2. Fluid inclusion studies

Petrographic and fluid inclusions (FI) micro thermometric data, obtained by Assis (2006), allowed to distinguish different fluid types: (1) aqueous bi-phase FI with moderate salinity (between 2 and 12.8 wt.% eq. NaCl and homogenization temperature from 78.7 to 243 °C); (2) aqueous three-phase FI (L+V+S) with high salinity (between 37% and 43.5 wt.% eq. NaCl and homogenization temperature from 286.5 to 362.1 °C); (3) aqueous-carbonatic FI with low to moderate salinity (between 1.6% and 14.5 wt.% eq. NaCl and homogenization temperature of 159.3 to 315.8 °C). According to Assis (2006), CO<sub>2</sub>-rich fluids coexisting with aqueous fluids with high salinity suggest a magmatic or metamorphic immiscible system that interact with more diluted aqueous fluids. Estimated pressure and temperature conditions for the entrapment of fluid inclusions “3” vary from 1.0 to 3.6 Kbar and 236 to 368 °C, respectively. Taking into account these values, the Paraíba veins possibly formed in a depth of 3.0 to 10.8 km.

Silva and Abram (2008) identified similar FI types in the principal quartz veins: (1) carbonatic FI (with a homogenization temperature from 12 to 31.1 °C); (2) aqueous-carbonatic (with low salinity between 4.6 and 25 wt.% eq. NaCl and a homogenization temperature from 270 to 320 °C); (3) aqueous FI (LH<sub>2</sub>O + VH<sub>2</sub>O) (with low salinity between 1 and 4 wt.% eq. NaCl and a homogenization temperature from 200 to 340 °C); (4) aqueous bi-phase FI (with solids presence): (4a) presents LH<sub>2</sub>O + VH<sub>2</sub>O + S association (with a moderate to high salinity between 13 and 24 wt.% eq. NaCl and a homogenization temperature from 103 to 207 °C); (4b) present high salinity between 27.4 and 28.2 wt.% eq. NaCl and a homogenization temperature from 153 to 200 °C. Silva and Abram (2008) proposed that the process responsible for the ore mineral precipitation was a merge between magmatic fluids with high temperature and cold aqueous fluids with moderate to high salinity.

Trevisan (2015) also recognize in the Paraíba deposit the presence of three FI types in the Paraíba deposit: (i) three-phase aqueous-carbonatic FI, with (CO<sub>2</sub>(V) + CO<sub>2</sub>(L) + H<sub>2</sub>O(L) + NaCl) composition and variable salinity, from 10% to 80 wt.% eq. NaCl; (ii) aqueous FI, (H<sub>2</sub>O(L)), present water vapour (H<sub>2</sub>O(V)) and one or more solid phases. Most of these phases are of cubic shape, colourless and isotropic, revealing that halite is possibly the dominant solid phase; and (iii) mono-phase FI characterized by subrounded to sub-angular colourless to dark-colour inclusions, randomly distributed within quartz crystals. This inclusion type is common in the Paraíba principal quartz vein coexisting with type 1 inclusions.

Additionally, Silva and Abram (2008) and Trevisan (2015) estimated crystallization temperatures using the chlorite geothermometer proposed by Chatelineau and Nieva (1985). The first authors obtained, for the principal auriferous quartz vein, values between 290 and 340 °C, concordant with the FI study. Trevisan (2015) obtained crystallization temperatures between 314 and 332 °C and barometric data from 6.5 to 9.5 kbar, suggesting a depth between 19.6 and 28.5 km. These values are considerably higher than those obtained by Assis (2006), probably because of the high Si content in the structure of the analysed muscovite crystals.

### 5.3. Lithotypes

The local geology of the Paraíba deposit is constituted by seven main lithotypes: (i) gneiss, (ii) tonalite, (iii) phyllonite, (iv) fine-grained gabbroic dykes, (v) gabbro, (vi) syenogranite porphyry, and (vii) quartz-rich syenogranite dykes (Fig. 9).

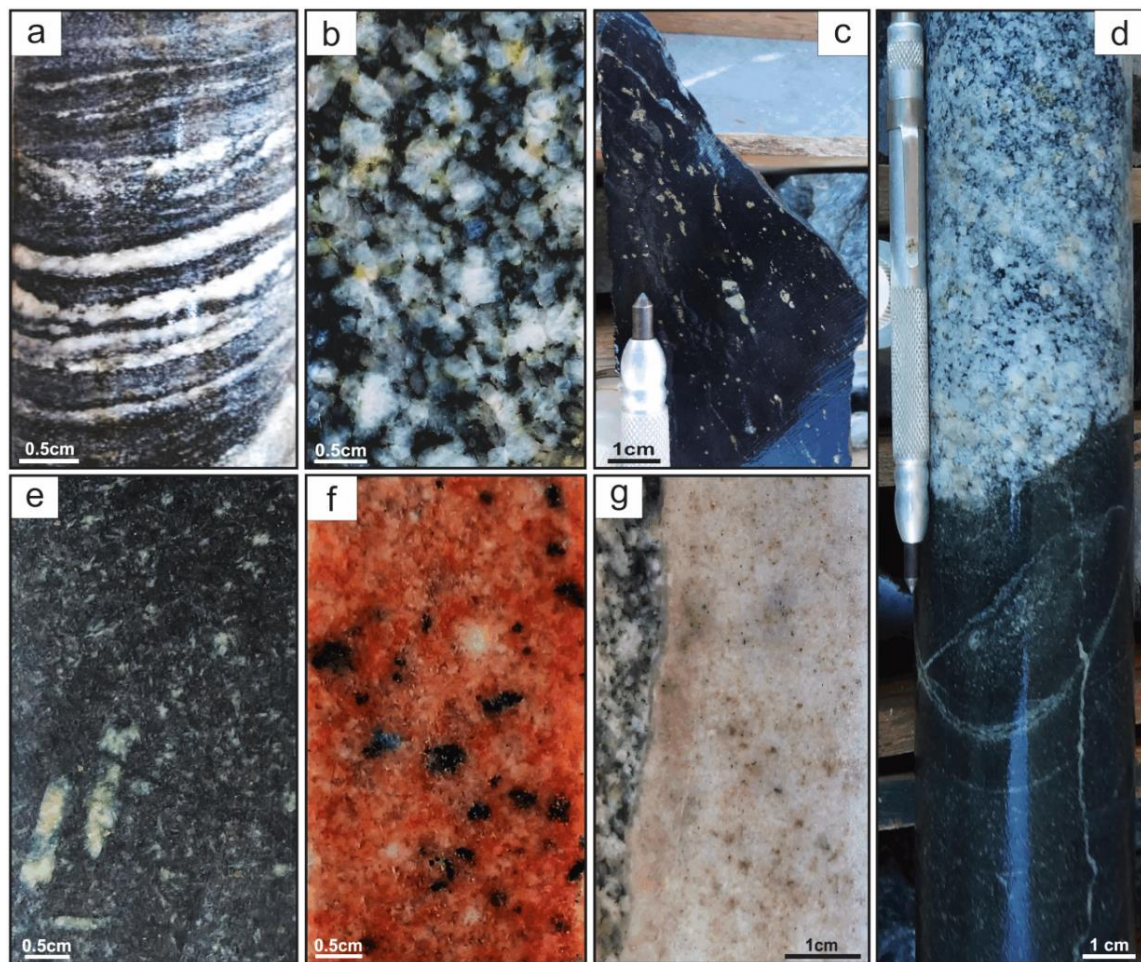


**Figure 9:** Macro aspects of the lithotypes from Paraíba deposit. (a) Biotite gneiss with gneissic banding; (b) Paraíba tonalite; (c) Phyllonite; (d) Fine-grained gabbroic dyke cutting the Paraíba Tonalite; (e) Gabbro with serial texture and porphyritic plagioclase phenocryst; (f) Syenogranite porphyry; (g) Quartz-rich syenogranite felsic dyke cutting the Paraíba Tonalite.

It was observed that the gneiss is the oldest rock of the deposit and it was firstly intruded by the tonalite. Both lithotypes were transformed in phyllonites by faulting and later intruded by fine-grained gabbroic dykes and porphyritic gabbroic bodies. Finally, these lithologies were cut by quartz veins and veinlets, a syenogranite porphyritic body, quartz-rich syenogranite felsic dykes, breccias and stock-works.

The gneiss, described by Trevisan (2015) and Oliveira (2016), was defined as an anisotropic, equigranular, fine-grained rock with well-defined deformed foliation and a granitic composition. It presents mafic bands that vary between 0.5 and 2 cm of thickness and are composed of biotite and hornblende (Fig. 9a). The leucocratic bands are characterized by quartz, plagioclase and K-feldspar.

The tonalite is a leucocratic, white-greyish and fine to medium-grained rock (Fig. 9b), usually isotropic, but also presents locally anisotropic flexures of foliated appearance. The texture varies from an equigranular, euhedral to subhedral, up to seriate inequigranular. It is composed of quartz, plagioclase, K-feldspar, biotite, chlorite, titanite, apatite, zircon and epidote. In thin section, the quartz appears anhedral, medium-grained, with subgrains, with wavy extinction and, in many cases, recrystallized. The microcline appears in anhedral to subhedral crystals, often with perthitic texture and quite altered to muscovite/sericite. On the other hand, the feldspars, especially oligoclase, are partial to fully overprinted by muscovite/sericite, while biotite crystals are subhedral, medium to coarse-grained and varies from well-preserved grains to completely alter to chlorite.

Phyllonite is a term used by several authors to refer to a rock in which texture is the result of ductile shearing or mechanical shattering of grains and often show only slight development of new minerals (Sander 1911, Sibson's 1977, Prochaska *et al.* 1992, Jefferies *et al.* 2006). It indicates a rock with phyllitic appearance created by deformation. Some classifications consider it as a variety of ultramylonite that contain 90-100% matrix. In the Paraíba deposit, phyllonite is found in strips parallel and subparallel to the main deformation zone, with an N05-15W orientation. The strips have a variable width from 0.5 to 8 m, greyish to dark green colour and are fragile and moderately friable (Fig. 9c). They partly present strong deformation and penetrative foliation, defined by phlogopite and biotite crystals and subordinate chlorite and muscovite. The main quartz veins, with dimensions from centimetric to 1.5 m, are placed in the mylonitic foliation, even though in certain zones are discordant to the phyllonite.

The fine-grained gabbroic dykes show a phaneritic, equigranular, holocrystalline and fine-grained texture (Fig. 9d). According to Oliveira (2016), these dykes present a

mineral assemblage composed by hornblende and plagioclase with intense propylitic hydrothermal alteration.

The gabbro is a fine, melanocratic and phaneritic greenish-black rock, isotropic with seriate texture and with porphyritic plagioclase crystals, some of them partially chloritized (Fig. 9e). The phenocrysts represent about 10% of the rock and are composed of euhedral to subhedral plagioclase grains with a greenish-white colouration and dimensions between 2 and 10 mm. The matrix is fine to very fine-grained (<1 mm), and contains plagioclase and fine mafic grains. The mineral composition comprises 55% plagioclase, 40% mafic minerals and 5% quartz, which allows to classify it as a gabbro or a fine-grained diorite. This lithotype is intensely hydrothermally altered, where the transformation of mafic minerals to actinolite, silicification, quartz grain recrystallization and plagioclase destabilization are common.

The porphyry is a pink to pale pink, leucocratic, fine-phaneritic rock, varying from equigranular to inequigranular. It shows granular euhedral/subhedral to seriate texture and porphyritic euhedral to subhedral plagioclase, microcline and quartz crystals (Fig. 9f), that constitutes about 10 to 15% of the rock volume, and sizes between 1 and 6 mm. The biotite grains appears subhedral, reddish black, and with sizes between 0.5 and 2 mm. The porphyry matrix is fine to very fine-grained, with crystal sizes smaller than 2 mm and formed of plagioclase, K-feldspar, quartz, muscovite, biotite and magnetite crystals. The microcline shows subhedral crystals of fine to medium size, sometimes with perthite texture and without developed twins. Quartz is anhedral with sizes between 25 and 200 microns; crystals larger than 250 microns present wavy extinction and sub-grain generation. The plagioclase content is limited, occurs in subhedral, fine to medium-grained crystals, with polysynthetic twins and commonly altered to muscovite/sericite. The mineral association is estimated in 25% quartz, 40% microcline, 10% plagioclase, 20% muscovite and 5% magnetite, and can be classified as syenogranite porphyry.

The light pink quartz-rich syenogranite dykes are leucocratic and fine to very fine-grained. They are isotropic, with euhedral and subhedral K-feldspar, muscovite and opaque crystals forms (Fig. 9g). They are discordant in respect to the tonalite, related maybe to a more evolved stage of the porphyry. The mineral assemblage is estimated in 60% quartz, 15% muscovite, 15% k-feldspar, 5% epidote, and 5% opaques (pyrite and chalcopyrite).

All lithotypes were defined by a detailed description of boreholes BH020, BH041 and BH059, corresponding to the main section of the deposit, as shown in Figure 10.

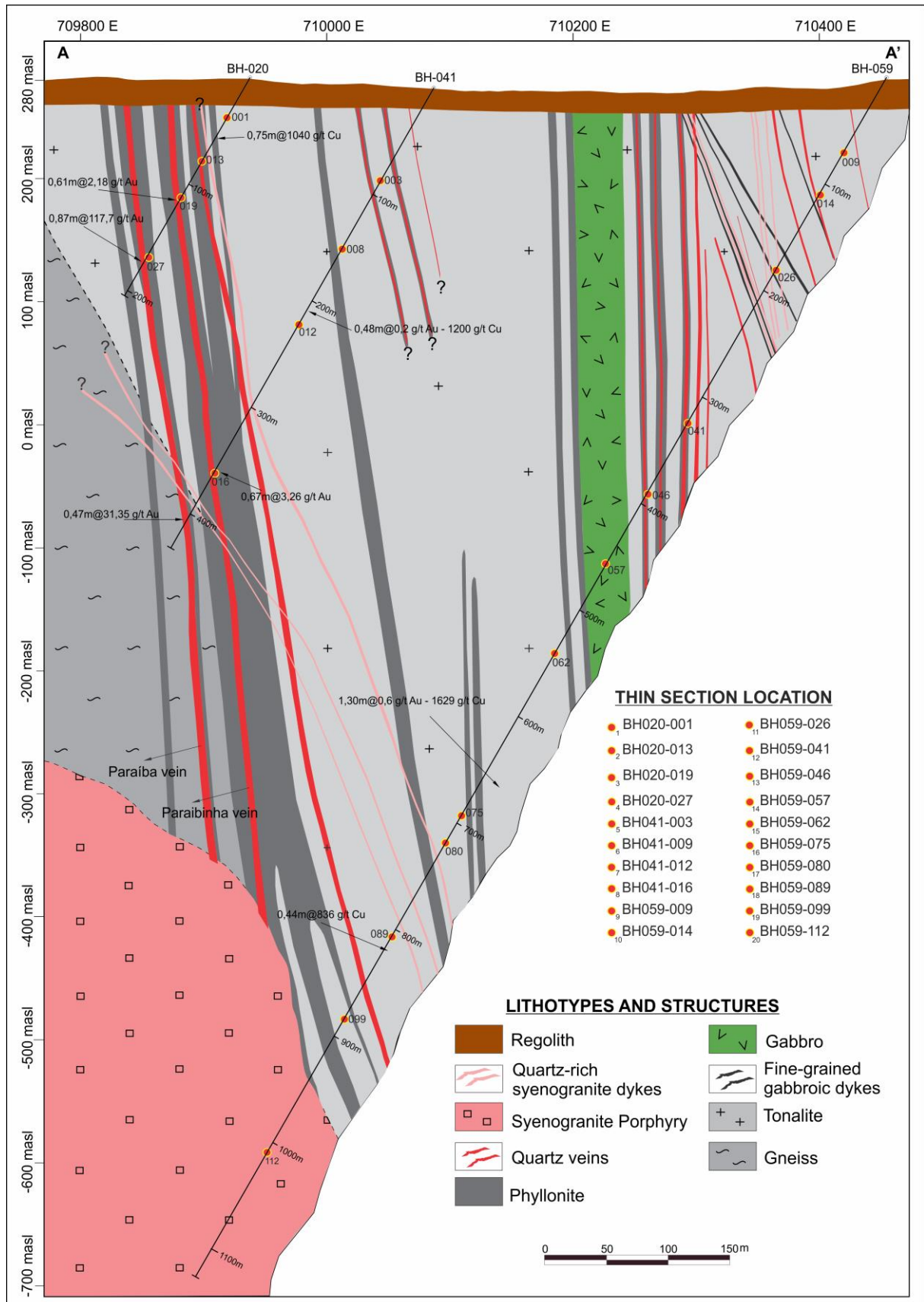


**Figure 10:** Main section of the Paraíba deposit, showing the relevant lithotypes and structures. The temporal and spatial relationships among them and the areas with the highest Cu and Au values are indicated. Vertical and horizontal scales are similar.

#### **5.4. Mineralization and Hydrothermal Alteration**

Different types and styles of hydrothermal alteration occur in the granitic rocks surrounding the mineralized zones of the Paraíba deposit. The areas with Au, Cu and Mo anomalies are mainly associated with sulphides-rich quartz veins and veinlets, as well as to zones with disseminated sulphides related to intense sericitic, propylitic and epidote-rich alterations.

The hydrothermal alteration zones, shown in Figure 11, were described according to the proposed paragenetic evolution time (Table 3) created from field observations, spectral data and thin section description. They were grouped in two major stages: (i) metamorphic-hydrothermal stage, related to a ductile shear system and (ii) magmatic-hydrothermal stage, associated with the syenogranite porphyry rock intrusion which is correlated with the generation of different hydrothermal alteration zones, some of them with important economic value. Both stages have been divided into three principal sub-stages: Pre-ore, ore and post-ore stages.

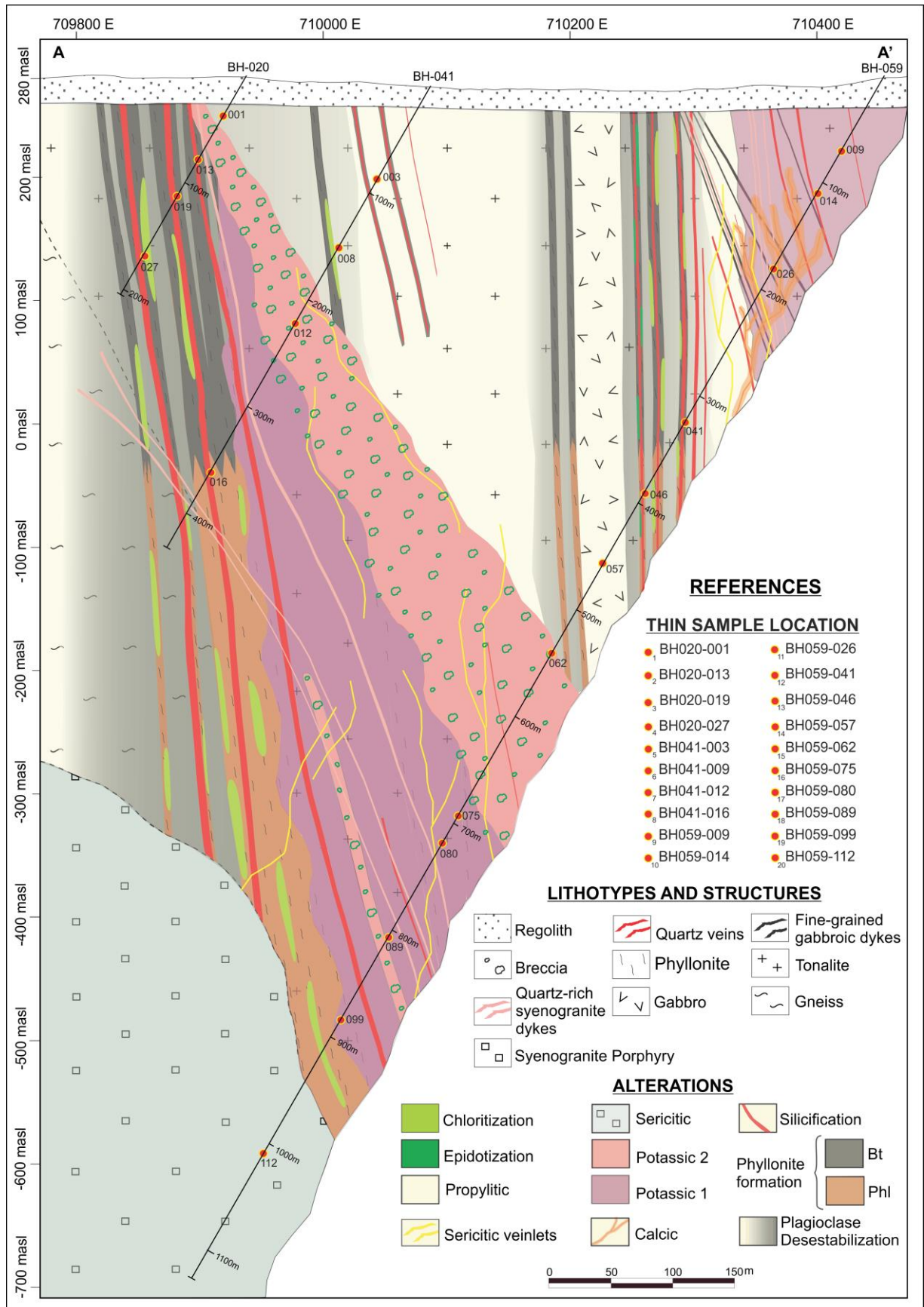


**Figure 11:** Paraíba main section with hydrothermal alteration zones. Vertical and horizontal scales are similar. Bt= biotite; Phl= phlogopite.

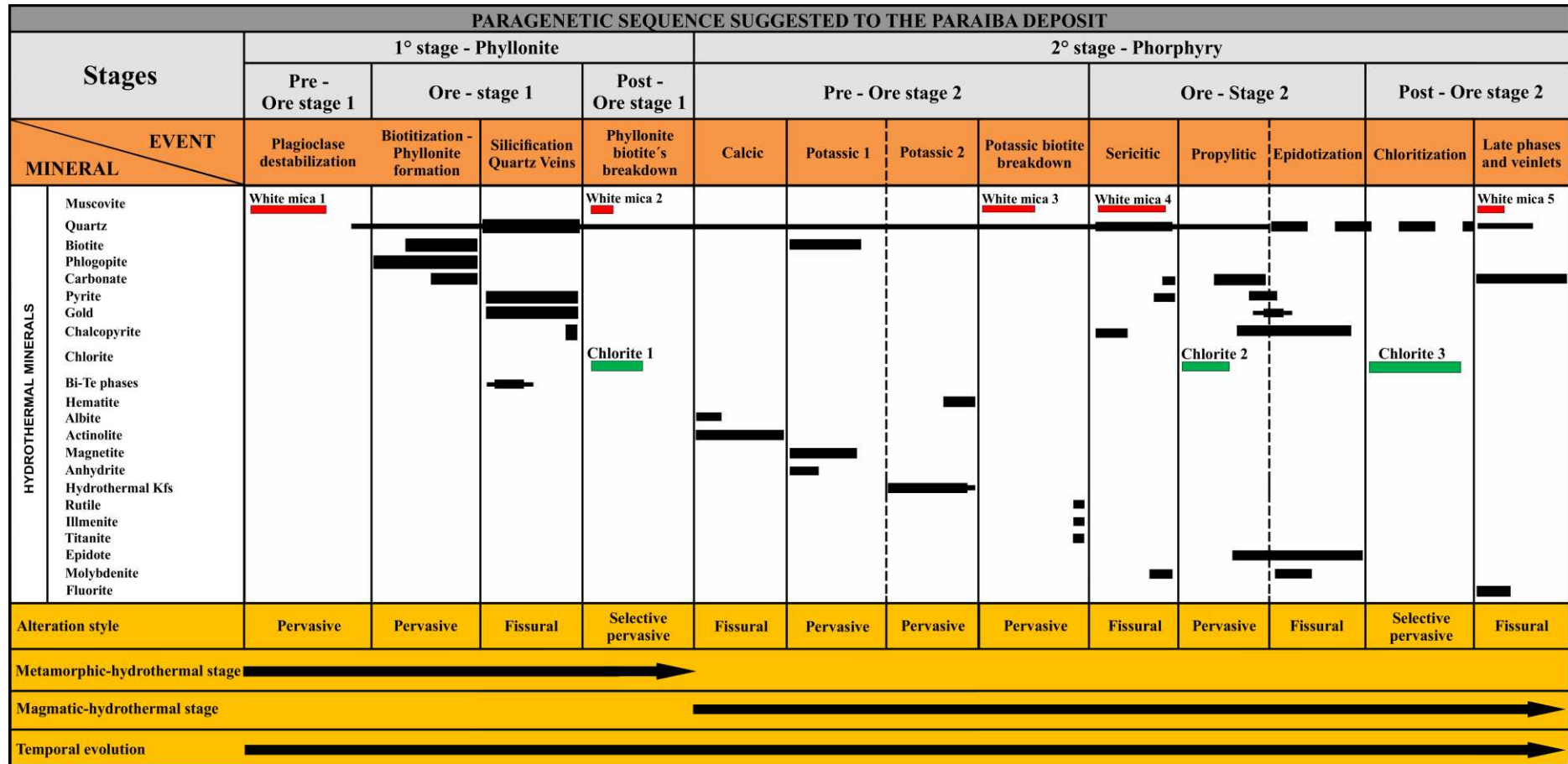


**Table 3:** Paragenetic temporal evolution proposed for the Paraíba deposit.

#### 5.4.1. Pre-ore stage 1 - Plagioclase destabilization

This alteration represents the initial stage of the paragenetic evolution (Fig. 12a-b). The principal mineral assemblage is composed of fine-grained white mica ('White Mica 1') + quartz. In strongly altered areas, the White Mica 1 completely replaces plagioclase and occasionally igneous biotite, giving the rock a greyish colouration. Plagioclase is the most susceptible mineral to this alteration. It is commonly replaced by anhedral to subhedral White Mica 1, with sizes between 5 and 80  $\mu\text{m}$ , generated from the grain edges towards the centre or from the twin faces. The spectral analysis, made from ASD data, indicate for White Mica 1 an illite to muscovite/illite normal potassic composition, evidenced by the position of the principal absorption feature at  $\sim 2200\text{ nm}$  (Fig. 12c).

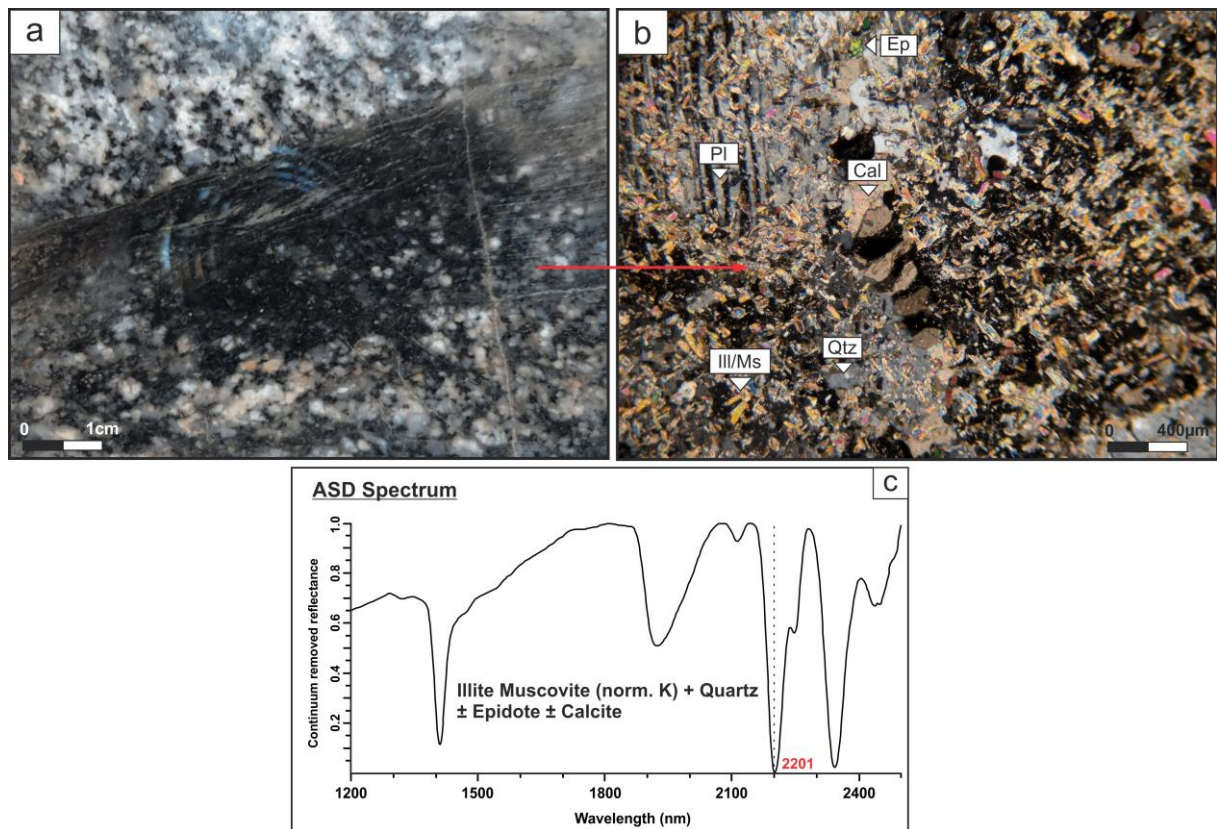


**Figure 12:** a) Paríba tonalite showing a stronger alteration near to deformed areas, related to the first mineralized event; b) feldspar alteration, principally plagioclase, generating fine white mica, represented by illite and muscovite (normal potassic composition). Ill: Illite; Ms: Muscovite; Qtz: Quartz; Cal: Calcite; Ep: Epidote; Pl: Plagioclase.

#### 5.4.2. Ore-stage 1 - Biotitization

This stage represents the phyllonite formation (Figs. 13a). It appears as a pervasive and intracrystalline alteration, mainly defined by phlogopite, biotite and carbonate oriented crystals. Up to 250 m down the borehole present a biotite + carbonate dominant composition, with predominance of Mg-biotite; beyond that depth biotite crystals are replaced by phlogopite + carbonate crystals.

Biotite shows grain sizes between 25 and 100  $\mu\text{m}$ , euhedral to subhedral with laminar texture and brown colour (Fig. 13b). Associated with this alteration there is a large quantity of very fine and irregular crystals of carbonates with sizes from 25 to 250  $\mu\text{m}$ . For its part, the phlogopite is coloured light brown to greenish, presents laminar habit with grain sizes between 25 and 500  $\mu\text{m}$ , subhedral to anhedral form and usually zoned with higher and lower Mg content areas (Fig. 13c and d). The compositional variation between biotite and phlogopite could be observed from ASD spectra, while both minerals are spectrally similar, a detailed analysis of the shape, symmetry and depth of the main ( $\sim 2250$  and  $\sim 2350$  nm for biotite, and  $\sim 2244$  y  $\sim 2325$  nm for phlogopite) and secondary ( $\sim 2380$  nm for phlogopite) absorption features, allowed their proper classification (Fig. 13e). SisuCHEMA data with spatial resolution of 156  $\mu\text{m}$ , collected from some representative samples, show dark strips of biotite or phlogopite composition, accompanied by calcite and subordinate phengite white mica and chlorite, generated by the alteration of biotite and/or phlogopite (Fig. 14).

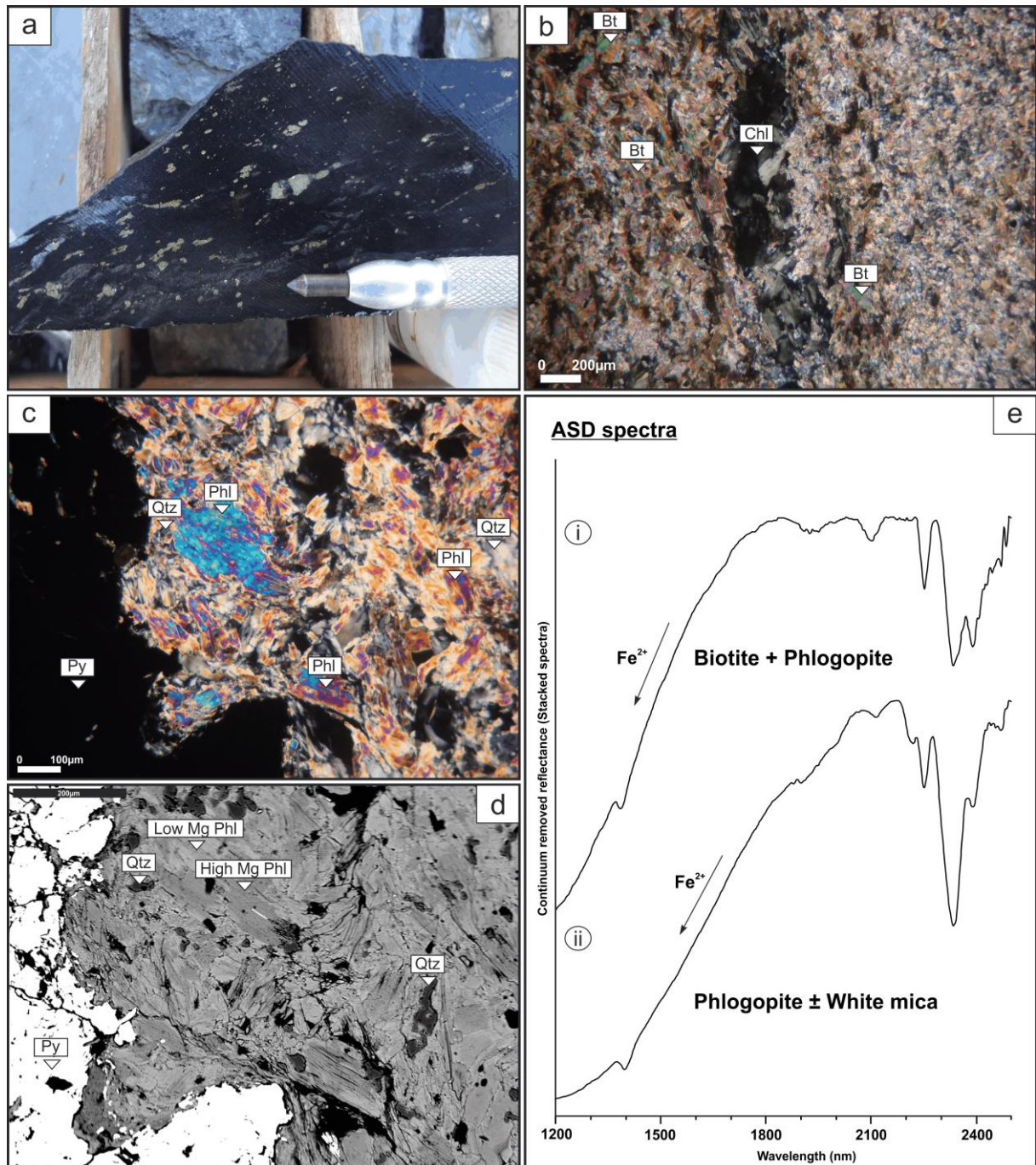


**Figure 13:** a) Phyllonite hand sample; b) Thin section (crossed nicols) of the phyllonite BH020-019 sample at 125 meters of depth, composed of magnesian biotite; c) Thin section (crossed nicols) of the phyllonite BH041-016 sample at 360 meters of depth; d) Electron microprobe image (same location as figure 13c) showing some phlogopites crystals with internal compositional zonation; e) Characteristic phyllonite spectra, with phlogopite and biotite (i) and subordinate white mica associated with the phlogopite alteration (ii). Phl: Phlogopite; Qtz: Quartz; Py: Pyrite; Bt: Biotite; Chl: Chlorite.

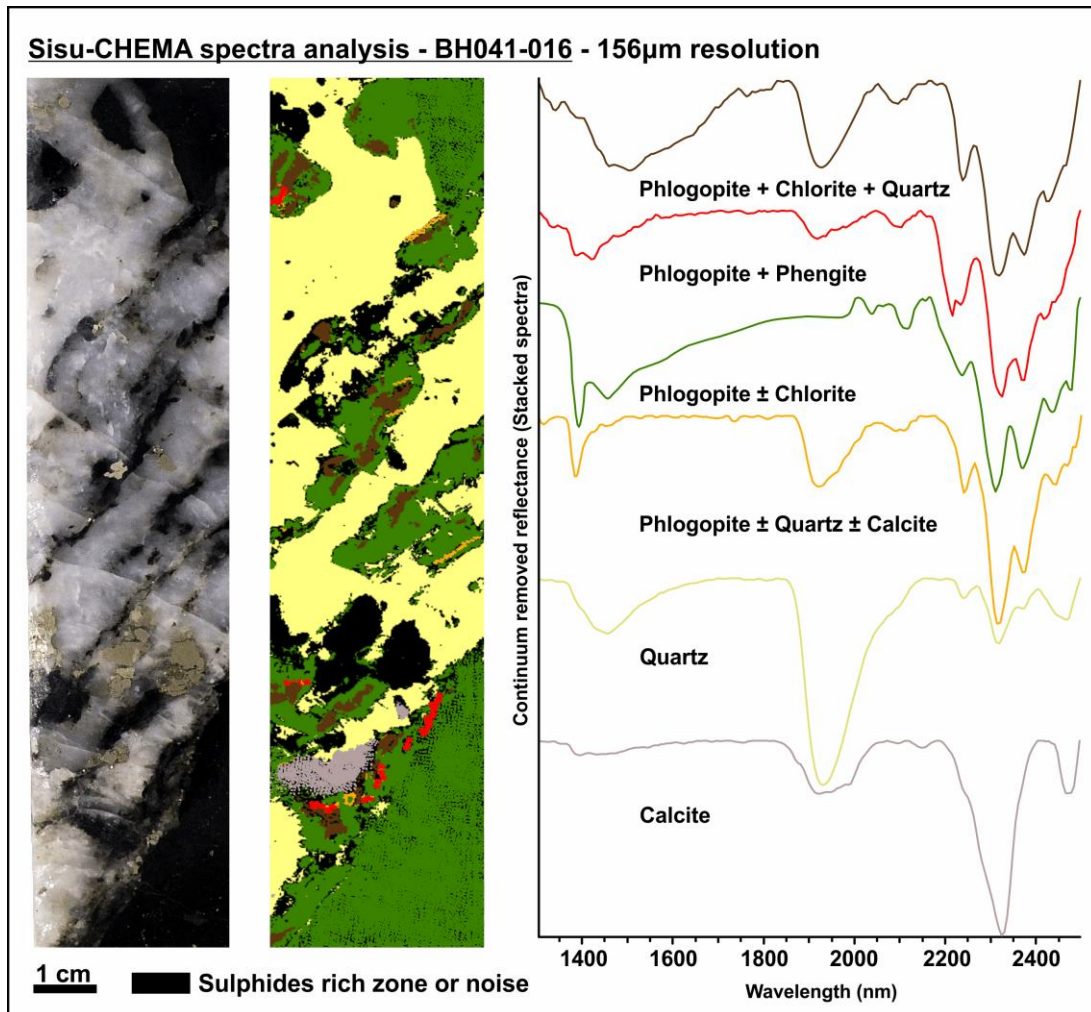


**Figure 14:** Photo (left) and mineral spectral map (right) produced from SisuCHEMA image of the BH041-016 hand sample. Representative SisuCHEMA spectra employed in SAM classification are illustrated with correspondent mineral interpretations.

#### 5.4.3. Ore-stage 1 – Silicification

This alteration includes the Paraiba and Paraibinha quartz veins formation, which are placed in the phyllonite-mylonitic foliation. This vein presents 0.5 to 2 m width, massive and banded textures, sulphide-rich bands of 1 to 3 cm, possibly due to successive opening and filling events (Fig. 15). These sulphides represent up to 30% of the veins, which are composed of quartz + pyrite ± chalcopyrite ± bismuthinite ± native bismuth.

Other secondary veins are centimetric, with up to 0.5 m width and have massive texture. In certain sectors these veins are discordant respect to the phyllonite. The tonalite and gneiss are the host rocks and usually present disseminated pyrite.

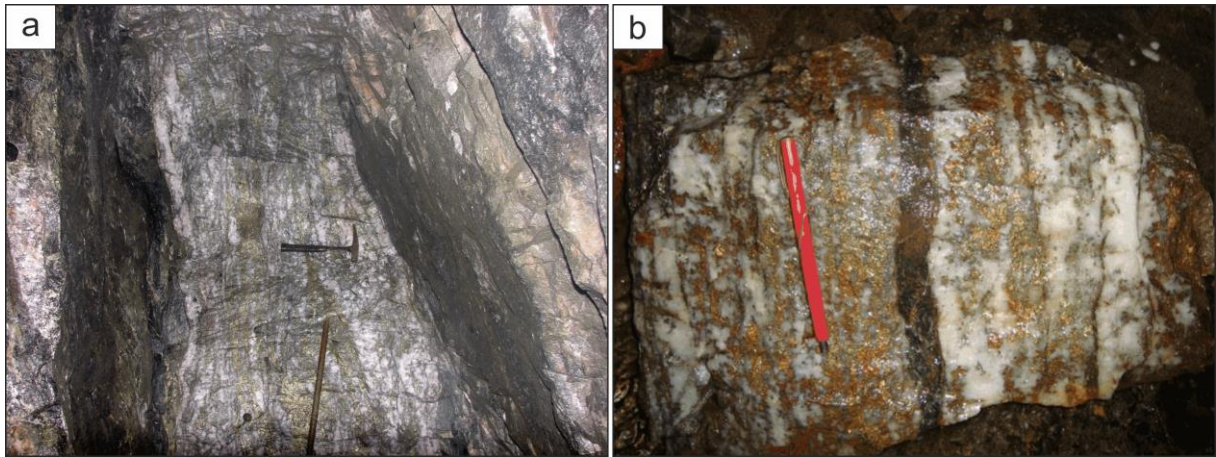


**Figure 15:** a) Principal 'Paraíba Vein' in the interior of the gallery; b) Quartz vein with centimetric sulphide bands.

#### 5.4.4. Post-ore stage 1 - Phyllonite biotite breakdown

This alteration corresponds to the final stage within the metamorphic-hydrothermal stage. The phlogopite and biotite that present in the phyllonites were altered to white mica and chlorite. The white mica crystals, named as “White mica 2”, are subhedral with grain sizes from 50 to 200  $\mu\text{m}$  and laminar habit (Fig. 16a). The chlorite, named as “Chlorite 1” is anhedral to subhedral, fine to coarse-grained, and with sizes between 120 and 200  $\mu\text{m}$  (Fig. 16b, c, d).

Biotite and phlogopite destabilization was observed from ASD spectra. This analysis allowed the identification of phlogopite and phengite mixtures. The phengite is generated from the phlogopite alteration and is characterized by the principal absorption feature between 2210 and 2225 nm (Fig. 16 e-i). In figure 16e-ii a spectrum with abundant phengite is shown associated with relative amounts of phlogopite, biotite, and Mg-Fe-rich chlorite, being the white mica and chlorite generated from the phlogopite and biotite alteration. Figure 16e-iii shows mixtures between muscovite and chlorite, characteristic of those zones that present a stronger phlogopite and biotite alteration, accompanied with calcite, mineral associated with the phyllonite formation. In the same way, when the phyllonite destabilization is advanced, it is mainly composed of phengite and chlorite, with a variable amount of phlogopite and/or biotite. This relationship was observed with SisuCHEMA data, which also allowed identifying calcite and quartz late veins that cut the mylonitic foliation (Fig. 17).

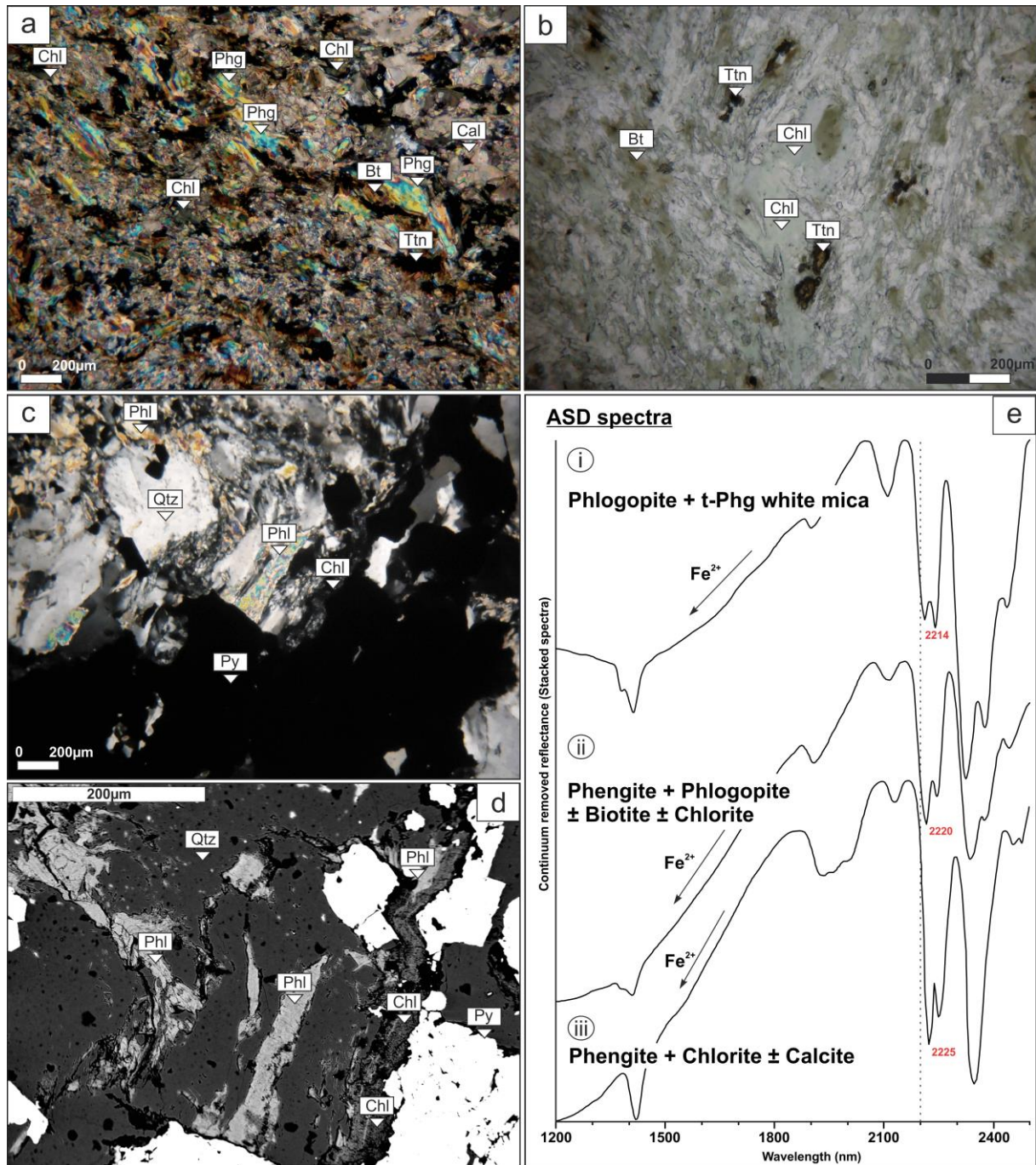


**Figure 16:** a) Phyllonite thin section (crossed nicols) composed of biotite and calcite. The biotite crystals are overprinted by chlorite and phengite; b) Phyllonite thin section photograph in which is possible to observe biotite crystals altering to chlorite and titanite, where the brown core corresponds to relict biotite.; c) Phyllonite (crossed nicols) composed of quartz + phlogopite + pyrite, with fine chlorite crystals generated from the alteration of phlogopite crystals; d) Electron microprobe image of phyllonite composed of quartz + phlogopite + pyrite, with fine chlorite crystals generated from the phlogopites alteration; e) Characteristic spectra from different zones of the phyllonite and respective mineral mixtures. Chl: Chlorite; Phg: Phengite; t-Phg: Tending to phengite; Bt: Biotite; Cal: Calcite; Ttn: Titanite; Phl: Phlogopite; Qtz: Quartz; Py: Pyrite.

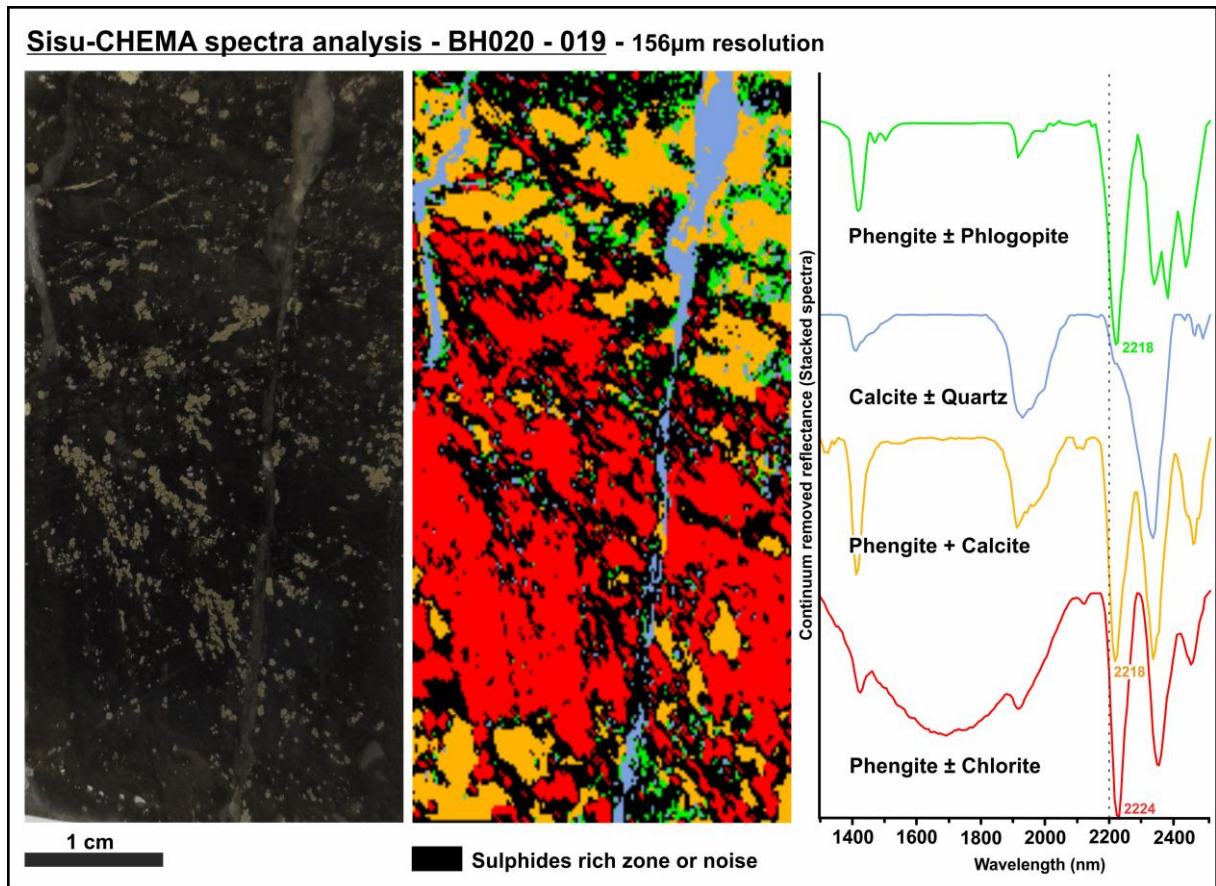


**Figure 17:** Phyllonite sample associated with Py of the Paraíba principal vein (left) and mineral spectral map produced from SisuCHEMA image (right) of drill core sample from Paraíba deposit. Representative SisuCHEMA spectra employed in SAM classification are illustrated with correspondent mineral interpretations.

#### 5.4.5. Pre-ore stage 2 – Calcic

The calcic alteration represents the beginning of the magmatic-hydrothermal stage, related to the syenogranite porphyry intrusion. It occurs in a restricted area, where the tonalite is strongly altered and fractured. It was described at the first meters of the bore-hole 059, an area characterized by the occurrence of many mafic and felsic dykes. The samples are characterized by a reddish green colouration and are composed of abundant actinolite + albite + quartz (Fig. 18a). The actinolite crystals are euhedral to subhedral and also prismatic to fibro-radial, with grain sizes between 50 and 350  $\mu\text{m}$  and occasionally reach 1 mm. For its part, the albite crystals are anhedral with grain sizes up to 20  $\mu\text{m}$ . In general, the albite crystals present a reddish colouration. The quartz is anhedral and fine with a grain size between 50 to 100  $\mu\text{m}$ .

The actinolite is clearly recognizable from the principal spectral features at 2100 nm (which differentiate it from talc), 2300 nm (as a result of the mixture with chlorite) and

the diagnostic feature at 2380 nm related to the Mg content, and the negative slope observed between 1500 and 1900 nm associated with the Fe content (Fig. 18g-i).

#### **5.4.6. Pre-ore stage 2 - Potassic 1 and Potassic 2**

These alterations are related to the syenogranite porphyry intrusion. Both are interdigitated, genetic and spatial related. In contact to the porphyry it is found the 'Potassic 1' alteration, formed by large amounts of biotite generated from the microcline and orthoclase alteration. It presents abundant magnetite, anhydrite and subordinate neo-formed hydrothermal k-feldspar (Fig. 18b, c and d). The biotite crystal sizes are from 1 to 3 mm, with subhedral form. The magnetite crystals vary from anhedral to euhedral, with sizes between 50 and 700  $\mu\text{m}$ . The microcline has around 2 mm length, with irregular twins evidencing its hydrothermal origin. The mineral assemblage for the potassic 1 alteration is quartz + biotite + K-feldspar + magnetite + anhydrite. The 'potassic 2' alteration is represented by a large amount of K-feldspar (microcline) + quartz + hematite. The hydrothermal microcline shows diffuse and irregular twins and grain size between 20  $\mu\text{m}$  and 5 mm (Fig. 18e). A large number of sub microscopic inclusions of hematite are founded, giving them the characteristic reddish colouration (Fig. 18f).

These alterations were determined from field descriptions, spectral data (which shows biotite predominance, Fig. 18g-ii) and petrographic analysis. Others minerals as magnetite, anhydrite, and K-feldspar do not have a good spectral response in the SWIR region of the electromagnetic spectrum.

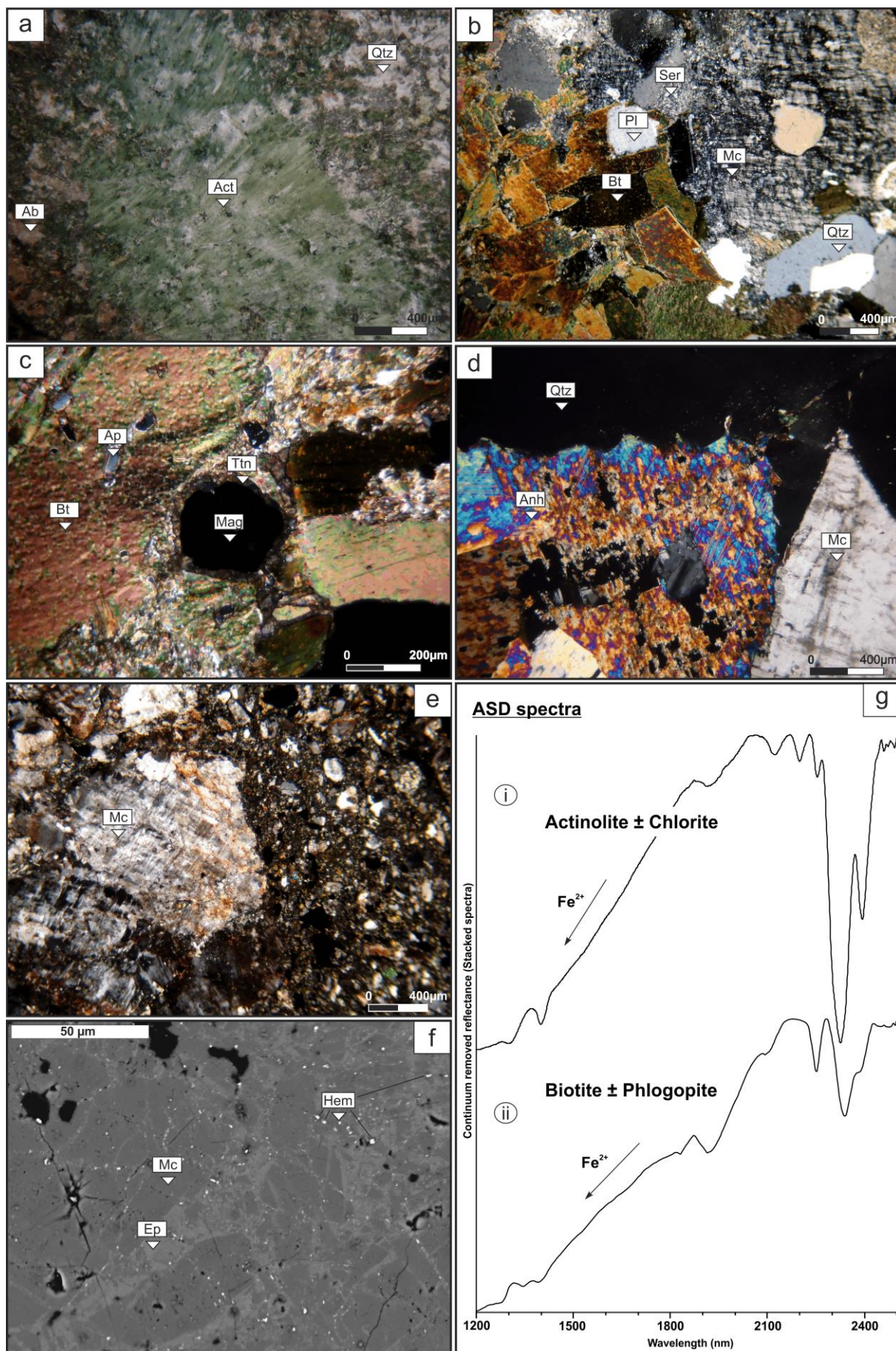


**Figure 18▲:** a) Calcic alteration represented by Qtz + Ab + Act crystallizing from fractures; b) Potassic 1 alteration (crossed nicols), altered Kfs grains forming hydrothermal Bt; c) Hydrothermal Bt grains associated with Mag with coronitic texture of Ttn at crossed nicols; d) Crossed nicols photograph of Qtz, Anh and Kfs grains associated with abundant hematite; f) SEM image showing fractured Kfs grains associated with Hem and Ep in the matrix; g-i) Characteristic Act spectrum, principal constituent of the calcic alteration; g-ii) Mixture spectrum between biotite and phlogopites, typical of zones with intense potassic alteration. Act: Actinolite; Ab: Albite; Qtz: Quartz; Pl: Plagioclase; Bt: Biotite; Ser: Sericite; Mc: Microcline; Ap: Apatite; Ttn: Titanite; Mag: Magnetite; Anh: Anhydrite; Hem: Hematite; Ep: Epidote.

#### 5.4.7. Pre-Ore stage 2 - Potassic biotite breakdown

Represent the last sub-stage within the pre-ore stage 2, and it is characterized by the destabilization of biotite crystals generated in the potassic alteration, forming muscovite grains named as White Mica 3. This white mica is associated with large amounts of ilmenite and rutile crystals, resulting from the release of Ti by the parental biotite and crystallizing in the cleavage face of the white mica.

The white mica is well-formed, with subhedral to euhedral form. Grain sizes vary from 200 to 1000  $\mu\text{m}$ , usually with tabular or lamellar habit, sometimes crenulated. Rutile appears with prismatic habit, subhedral to euhedral, with grain sizes ranging from 50 to 200  $\mu\text{m}$ . Ilmenite is coarse-grained (between 1800 and 3200  $\mu\text{m}$ ), with euhedral form and skeletal textures, being pseudomorphic from the titanite. This alteration is characterized by a mineral assemblage composed of white mica + ilmenite + rutile + titanite + quartz (Fig. 19a and b).

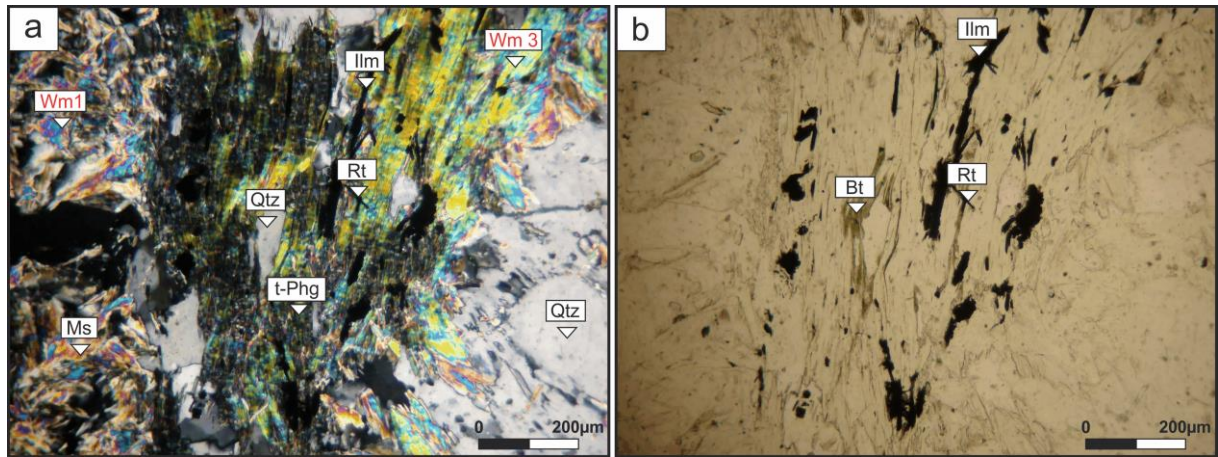


**Figure 19:** a) Potassic biotite breakdown alteration (crossed nicols) represented by Wm + Ilm + Rt + Ttn + Qtz; b) Potassic biotite breakdown alteration, Bt crystals altered to muscovite and the Ti-release form Ilm and Rt. Ms: Muscovite; Rt: Rutile; Ilm: Ilmenite; Qtz: Quartz; Bt: Biotite; Ttn: Titanite; t-Phg: Tending to phengite.

White Mica 3 was recognised from the ASD spectra as tending to phengite, characterized by the maximum absorption between 2207 and 2215 nm. White Mica 3 is surrounding and superposing the White Mica 1, as shown in the compositional white mica

gradient map generated from the SisuCHEMA data and validated by petrographic analysis (Fig. 20a). Figure 20b shows a SisuCHEMA compositional map where White Mica 1 is superimposed by white mica 3. Subsequently, both white mica groups are propilitized and epidotized.

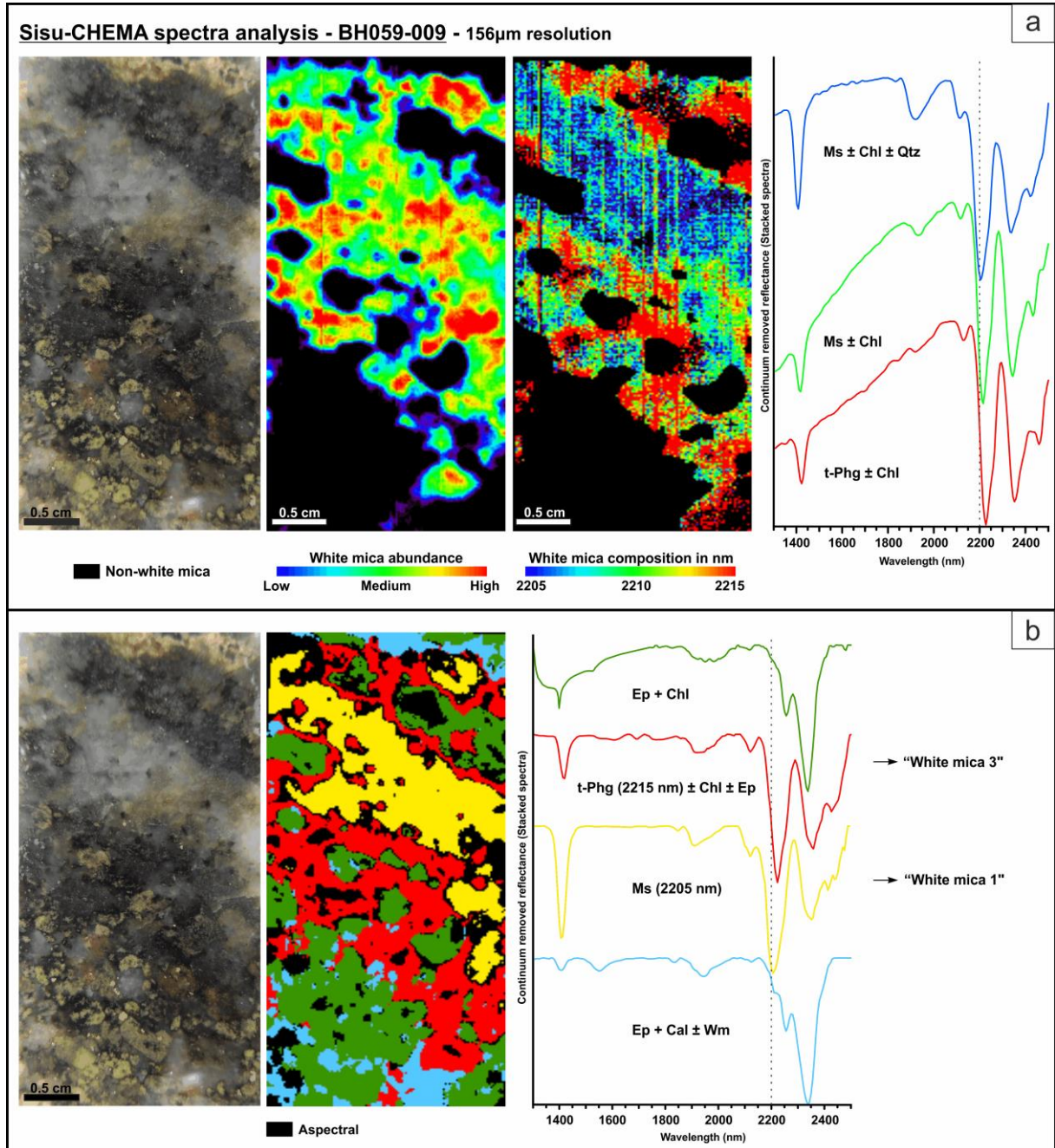


**Figure 20:** a) Hand sample photo and mineral maps produced from SisuCHEMA image of drill core sample. Representative white mica SisuCHEMA spectra, with White mica 1 and 3 abundance and composition. b) Hand sample photo and mineral map produced from SisuCHEMA device with correspondent mineral interpretations. Ep: Epidote; Wm: White mica; Ms: Muscovite; t-Phg: Tending to phengite; Chl: Chlorite; Qtz: Quartz.

#### 5.4.8. Ore Stage 2 – Sericitic

This alteration represents the first mineralization phase related to the syenogranite porphyry intrusion. It is formed by veins and veinlets with 2 - 20 cm width, composed by quartz (with massive texture), sulphides (pyrite, chalcopyrite and subordinated molybdenite), and white micas named as “White Mica 4”. This mica is fine- to medium-grained, presents tabular habit and sizes between 50 and 150  $\mu\text{m}$ .

Besides, veins and veinlets are observed cutting discordantly the potassic alteration zones, where the White Mica 4 is associated with carbonate crystals. The mineral assemblage, in this case, is represented by quartz + phengite + calcite + pyrite + chalcopyrite  $\pm$  molybdenite. (Fig. 21a). However, when these venules cut the tonalite, they present a mineral assembly of quartz + phengite + pyrite + chalcopyrite  $\pm$  molybdenite (Fig. 21b, c and d).

White Mica 4 presents a ‘tending to’ phengite to phengite composition, due to the variable position of the principal spectral absorption between 2213 and 2221 nm. According to their crystallinity, it could be muscovite and also muscovite/illite. Besides, this white mica is associated with calcite, quartz and also chlorite related to the alteration of primary tonalite minerals (Fig. 21e).

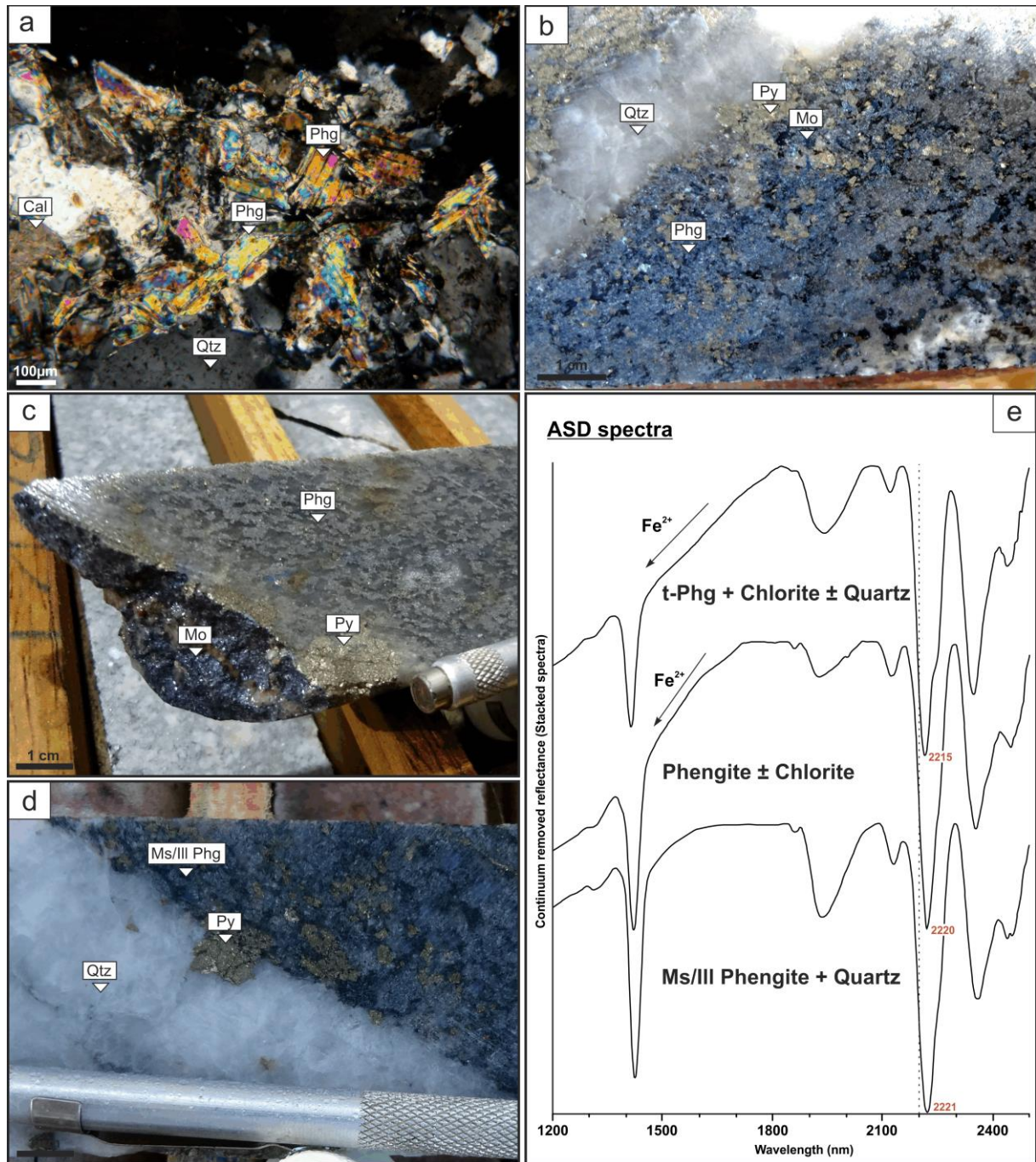


**Figure 21:** a) Sericitic alteration (crossed nicols) represented by quartz + pyrite + chalcopyrite + muscovite ± molybdenite ± calcite; b, c, d) Sericitic veins cutting the tonalite and presenting a mineral assemblage of quartz + phengite + pyrite + chalcopyrite ± molybdenite. In occasions white mica could be muscovite/illite phengite; e) Representative muscovite “tending to” phengite (2215) to phengite ASD spectra (2221 nm) associated with quartz and chlorite related to the primary tonalite mineral alteration. Ms: Muscovite; Qtz: Quartz; Cal: Calcite; Ill: Illite; Py: Pyrite; Mo: Molybdenite.

#### **5.4.9. Ore Stage 2 - Propylitic and Epidotization**

Propylitic and epidotization alterations are related to the syenogranite porphyry intrusion; therefore, they will be described together. The propylitic alteration is widely distributed along the main section, affecting all the lithotypes. It has a greenish colouration given by chlorite + epidote + calcite mineral assemblage (Fig. 22a). The chlorite, named as 'Chlorite 2', appears abundantly, with anhedral to subhedral shape and grain sizes between 200 and 750  $\mu\text{m}$ . This alteration is related to disseminated pyrite and chalcopyrite mineralization. When increasing the number of epidote crystals, the amount of pyrite also increases. The propylitic epidote crystals are generally sub-euhedral to anhedral with sizes between 25 and 100  $\mu\text{m}$ . The calcite is abundant, generally anhedral and with varied sizes.

The epidotization represents the final ore-stage within the magmatic-hydrothermal system. It is composed of large amounts of hydrothermal epidote with prismatic habit, euhedral form, and sizes that can reach up to 750  $\mu\text{m}$  (Fig. 22b). Areas with high epidotization have great economic value due to the presence of large amounts of disseminated chalcopyrite and molybdenite (Figs. 22c-d). Figure 22e shows the representative ASD spectra on epidotization areas, as well as propylitized zones, evidenced by the presence of chlorite and calcite in the spectra.

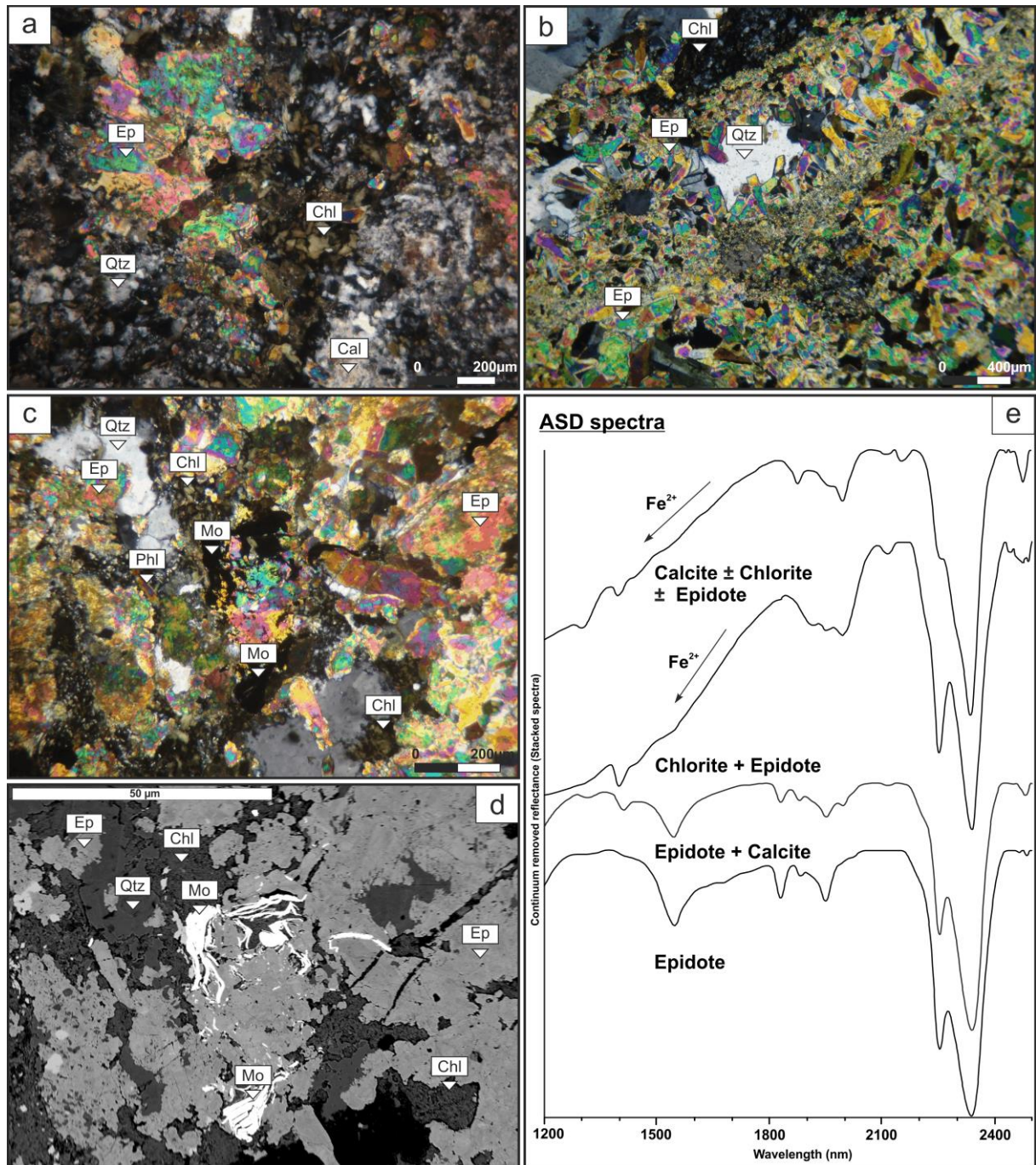


**Figure 22:** a) Propylitic alteration (crossed nicols) represented by chlorite + epidote + calcite; (b and c) Epidotization (crossed nicols) represented by disseminated chalcopyrite and molybdenite crystals; d) MEV photograph of Mo crystals associated with the Epidotization alteration zone; e) Propylitic and Epidotization characteristic ASD spectra. Ep: Epidote; Chl: Chlorite; Qtz: Quartz; Cal: Calcite; Mo: Molybdenite.

The epidotization is responsible for the hydrothermal breccia generation, fracturing the potassic 2 zone into angular to subangular feldspar crystals (microcline and orthoclase), with sizes between 20  $\mu\text{m}$  and 3 cm. The feldspar contains abundant small crystals of hematite, giving to the rock its reddish colouration. The matrix is very fine-grained ( $<5 \mu\text{m}$ ) and completely composed of epidote. The breccia fragments are composed of K-feldspar, that does not have any characteristic spectral response in the SWIR region, and the matrix is composed principally of epidote. SisuCHEMA data show phengite, quartz and calcite veins related to the sericitic alteration, cutting the potassic 2. Later the Potassic 2 and Sericitic alteration are obliterated by the epidotization (Fig. 23). Figure 24 shows quartz veins with sulphides, related to the silicification stage, and the generation of phengite and chlorite from phyllonites biotite and phlogopite alteration. Besides, it shows that the epidotization is superposing the previous alteration.

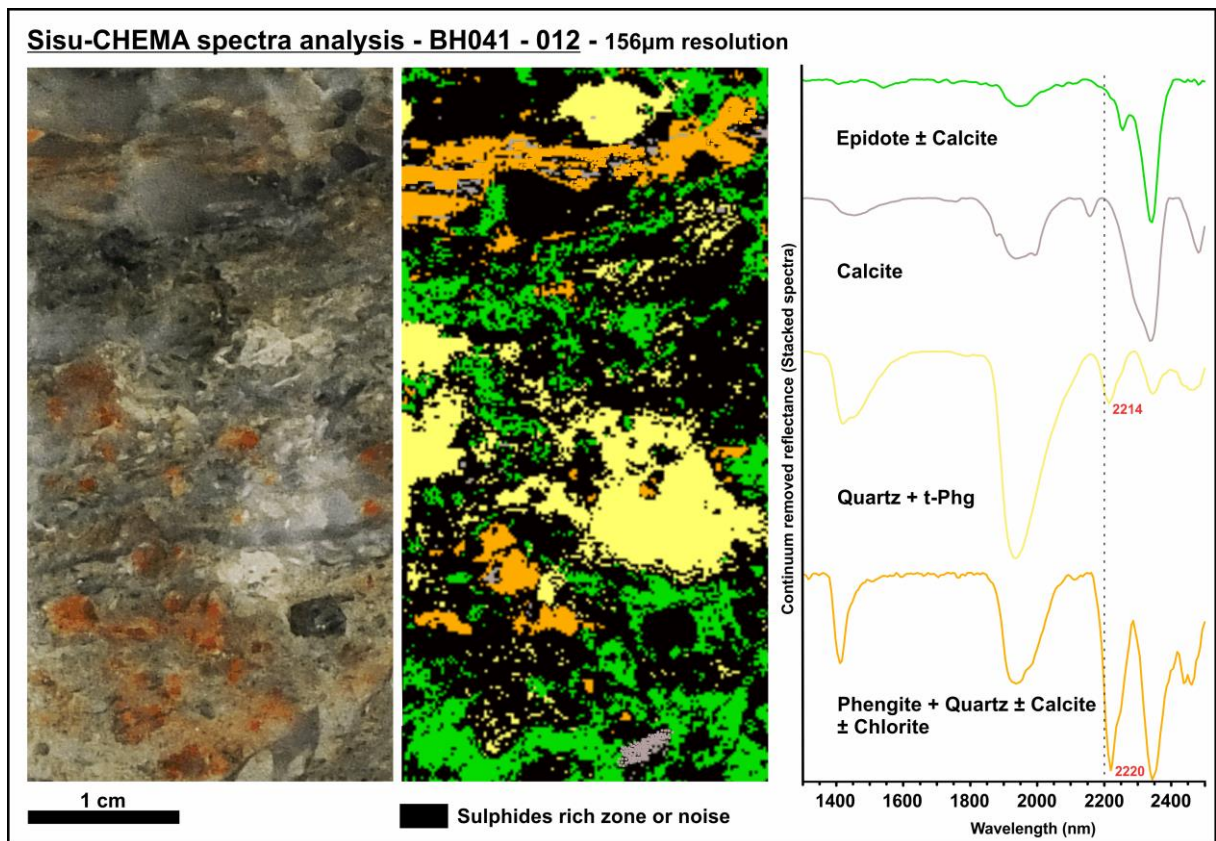


**Figure 23:** Potassic 2 alteration composed of K-feldspar and large amounts of hematite crystals. This alteration is cut by sericitic venules and finally fractured and obliterated by an epidote-rich fluid, which will generate the hydrothermal breccia (left) and a mineral map produced from SisuCHEMA image (right), with a spatial resolution of 156  $\mu\text{m}$ , related to the BH041-012 sample. Representative SisuCHEMA spectra used in SAM classification.

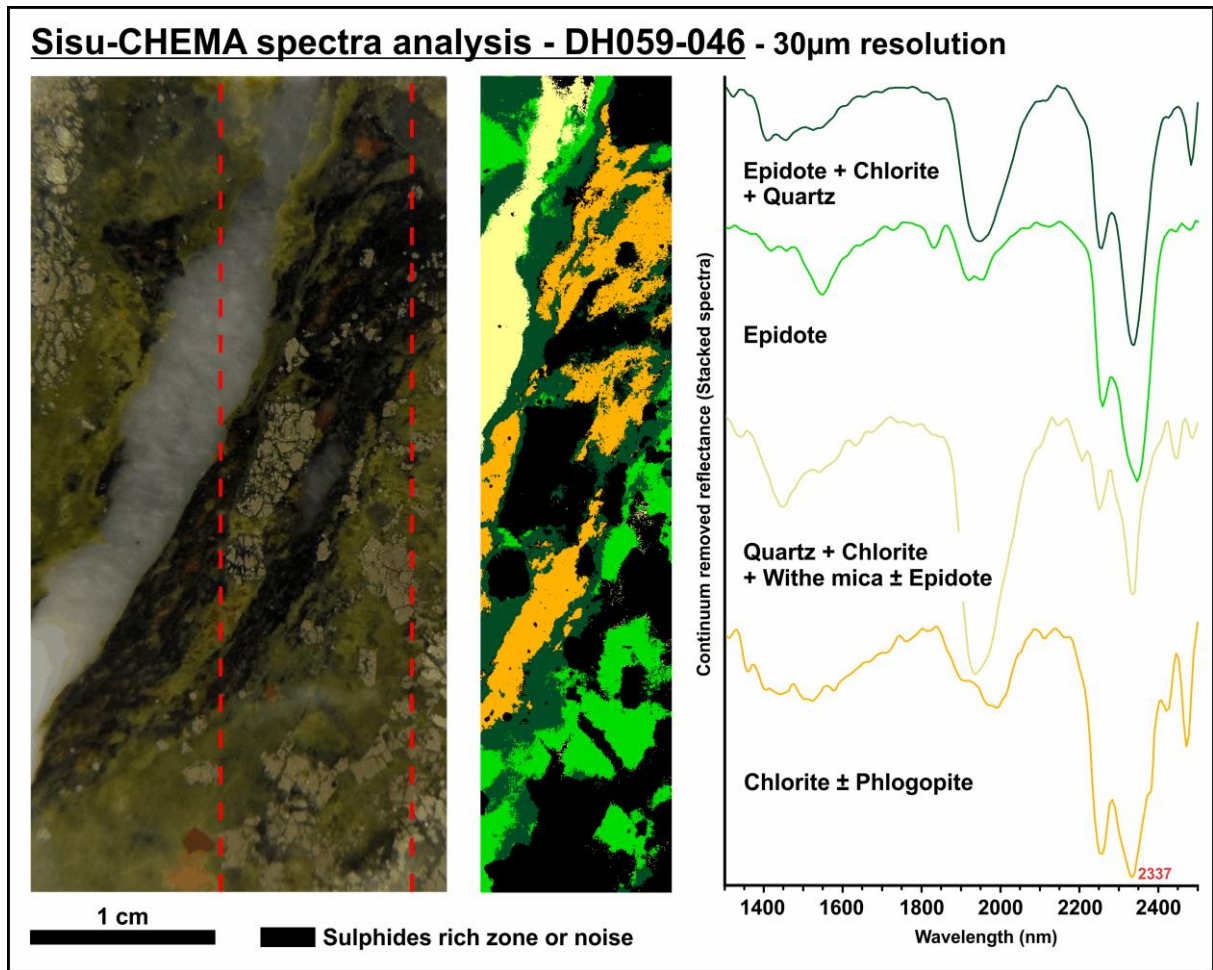


**Figure 24:** Epidotized phyllonite (left) and mineral map produced from SisuCHEMA image (right), with a spatial resolution of 30 µm, and related to the BH059-046. Representative SisuCHEMA spectra used in SAM classification.

#### 5.4.10. Post-ore Stage 2 - Chloritization, late phases and barren veins

The chloritization represents one of the "Stage 2 post mineralization" alterations and is related to a final stage within the Paraíba evolution. It is characterized by an intense and pervasive phyllonite chloritization, which gives to the rock a greyish black colouration, finer grains sizes and partial mylonitic foliation disappearance (Fig. 25a). Additionally, it is observed several pyrite crystals with phlogopite crowns. The chlorite, named as "Chlorite 3", appears with euhedral shape and grain sizes between 200 µm and 1 mm (Fig. 25b, c and d). ASD data show the Mg-Fe composition for this group of chlorites (2333 nm), besides spectrally evidencing the existence relic phyllonite phlogopites (2380 nm flexion) (Fig. 25e).

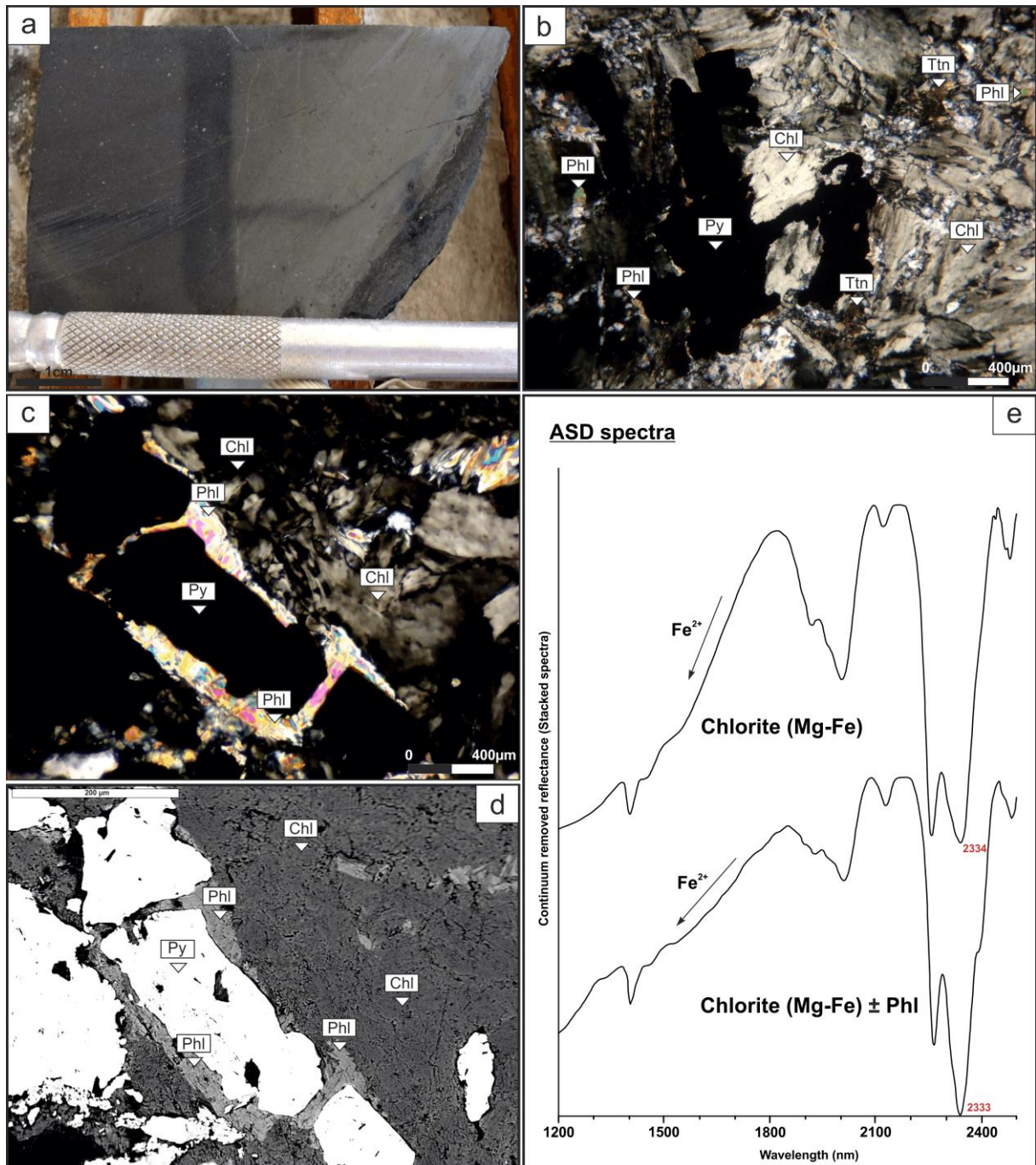


**Figure 25:** a) Chloritized phyllonite with a black greyish colouration and fine texture; b-c) Chloritization (crossed nicols), showing the Chl crystals and the relic phlogopite founded in the Py border grains; d) Chloritization electron microprobe photograph, showing Phl crystals surrounding Py grains; e) Characteristic chloritization ASD spectra, showing an intermediate Mg-Fe composition. Phl: Phlogopite; Chl: Chlorite; Ttn: Titanite; Py: Pyrite. (BH059-041 sample).

Additionally, it was observed from SisuCHEMA concerning the chloritized phyllonite sample that the phlogopite was replaced by large chlorite crystals, helping to determine the mineral and textural variations in a very-fine grained sample (Fig. 26).

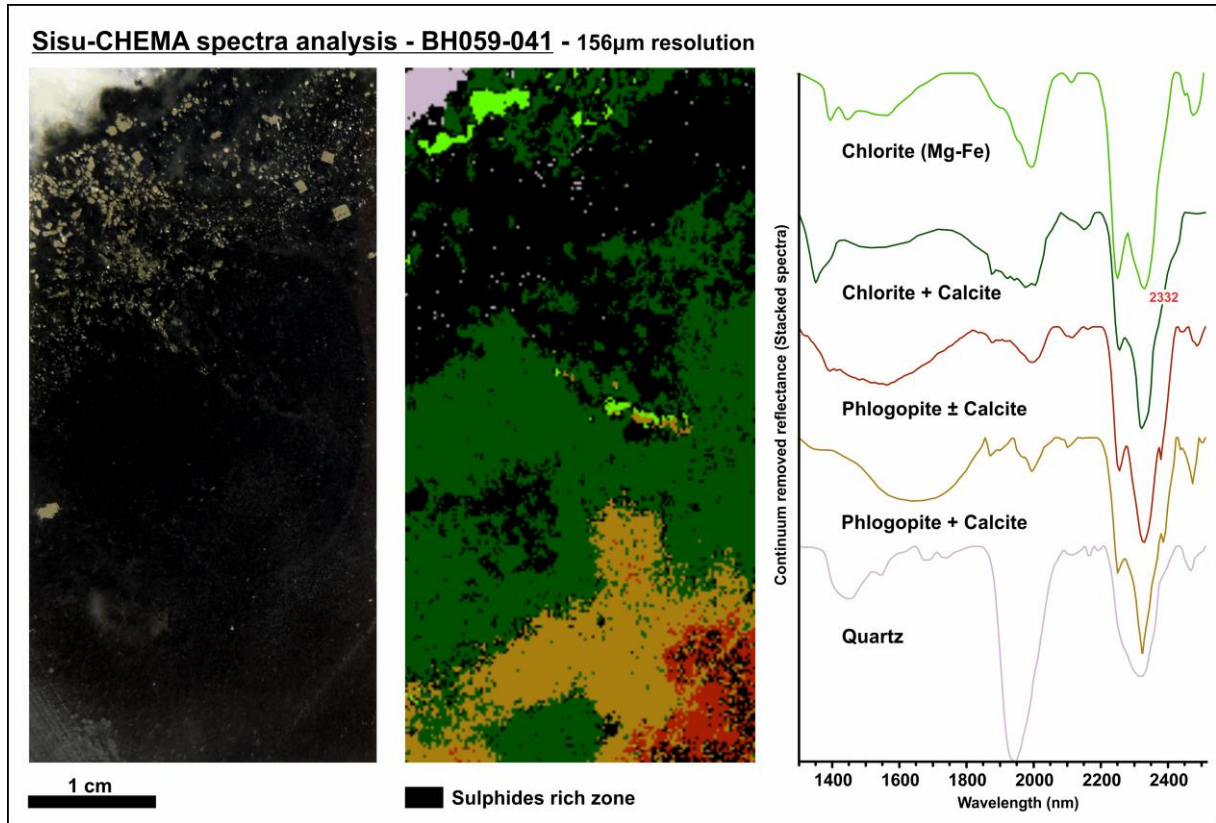


**Figure 26:** Chloritized phyllonite with a black greyish colouration and fine texture (left) and mineral map produced from SisuCHEMA image (right) with a spatial resolution of 156  $\mu\text{m}$  and related to the BH059-041 sample. Representative SisuCHEMA spectra used in SAM classification, showing how the phlogopite crystals are replaced by chlorite crystals.

The late phases and barren veinlets are cutting all the lithotypes as well as the rest of the hydrothermal alterations. They are distributed throughout the main section of the deposit. Veinlets, from millimetric to, occasionally, centimetric sizes, are mainly composed by barren quartz (Fig. 27a) and quartz + white mica. This white mica, named as “White Mica 5”, has a fibro-radial habit and sizes from 20 to 100  $\mu\text{m}$ , occasionally reaching 200  $\mu\text{m}$ . (Fig. 27b and c). They are possibly related to late syenogranite porphyry venules and present a “tending to” phengite composition with absorptions among 2212 and 2214 nm. In addition, veins of calcite, quartz + calcite, and quartz + magnetite + fluorite were observed (Fig. 27d).

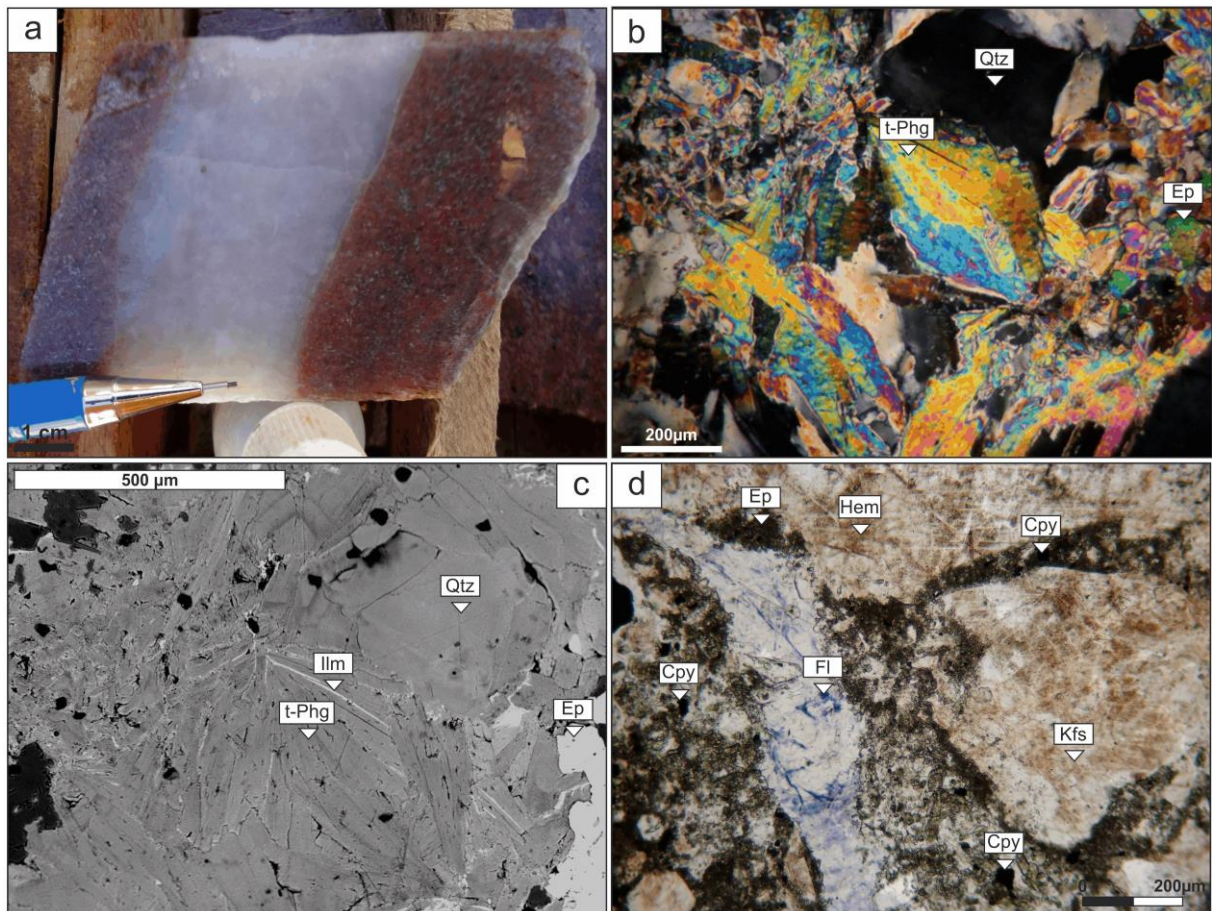


**Figure 27:** a) Barren Qtz veinlet cutting the porphyric syenogranite; b) Late Qtz vein + Ms (white mica) (crossed nicols); c) Late Qtz vein + Ms (White Mica 5) electron microprobe photograph; d) Late Qtz + Fluorite vein (crossed nicols). Qtz: Quartz; Ep: Epidote; Hem: Hematite; Ilm: Ilmenite; Cpy: Chalcopyrite; t-Phg: tending to phengite; Fl: Fluorite; Kfs: K-feldspar.

## 6. MINERAL CHEMISTRY

Regarding the spatial relationship between white mica, chlorite, biotite and epidote crystals with mineralized zones, there were obtained their chemical composition by electron microprobe analysis (Appendix 1 - 4). Considering the paragenetic sequence, the white mica was classified as White Mica 1, 2, 3, 4 and 5. These groups are associated with plagioclase destabilization, phyllonite biotite's breakdown, potassic 1 alteration, sericitic veins and barren veins, respectively. Chlorite crystals were classified as 1, 2 and 3, and are related to phyllonite biotite's breakdown, propylitic alteration and phyllonites chloritization, respectively. Biotite crystals, associated with phyllonite areas, were analysed considering the sample number and its position in the main cross section. Epidote crystals of propylitic and epidotized zones were also analysed with electron microprobe to study the high relationship that exists between this mineral and the Cu and Mo-rich zones.

### 6.1. White mica

The structural formulas were calculated on the basis of 11 equivalent oxygen atoms, in an anhydrous base and considering the separation of  $\text{Fe}^{2+}$  and  $\text{Fe}^{3+}$ .

According to Deer *et al.* (1992), a significant amount of water can indicate, among other factors, highly altered samples that do not reflect the original chemical composition. In that way, the selected compositional interval was between 90.8 and 97.6% and 3 of a total of 53 muscovite samples, with water percentages greater than 9.2 wt%, were excluded.

The five white mica groups identified by field descriptions, spectroscopy and petrography present different Al, Fe, Si and Mg contents (Table 4) and show different cation substitution degrees. Thus, using the white mica classification diagram (Fig. 28) proposed by Tappert (2013), the five (5) white mica groups fall within the phengite composition, determined by the Si:Al ratio bigger than 3 a.p.f. (Deer *et al.* 1992).

White Mica Characteristics	● White Mica 1	● White Mica 2	● White Mica 3	● White Mica 4	● White Mica 5
Al <sub>(t)</sub>	2.45	2.32	2.39	2.35	2.38
Fe <sub>(t)</sub>	0.19	0.15	0.23	0.15	0.24
Si	3.19	3.25	3.16	3.21	3.14
Mg	0.18	0.31	0.21	0.31	0.27

**Table 4:** Summary table of the 5 groups of white mica described for the Paraíba deposit with their respective average concentrations of Al<sub>(t)</sub>, Fe<sub>(t)</sub>, Si and Mg.

It was possible to determine different white mica compositions and the existence of two significant clusters: (i) White Mica 1 presents a phengite composition with Fe and Al

enrichment and low Si, (ii) White Mica 2 presents a compositional trend from phengite to Mg and Si-rich phengite, (iii) White Mica 3 has an intermediate phengite composition, (iv) White Mica 4 has an Mg-rich composition and an enrichment trend in Si, (v) White Mica 5 presents an intermediate phengite composition with high Si.

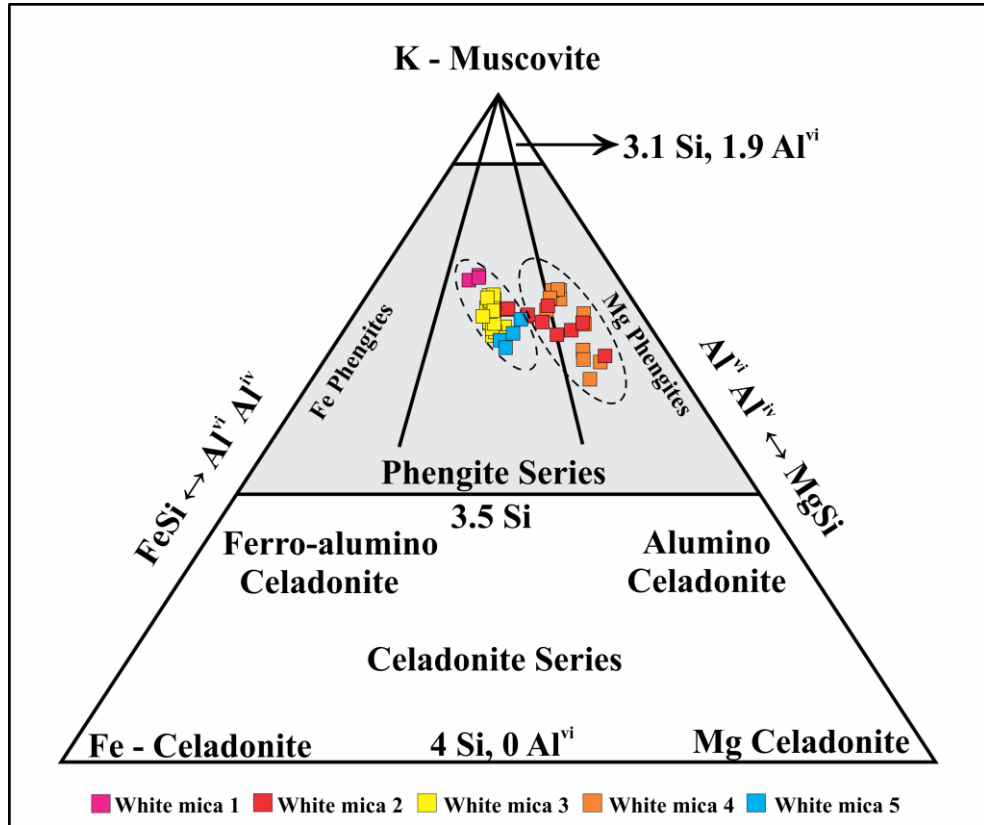


**Figure 28:** White mica compositional variations of the Paraíba deposit using the ternary diagram proposed by Tappert (2013).

In the analysed cases, the charge compensation is carried out by replacing  $\text{Al}^{\text{IV}} \rightarrow (\text{Fe}^{2+} + \text{Mg}^{2+})$  in the octahedral positions as is shown in figure 29a. The other very frequently substitution in the phengite group, is the Tschermak type. Miller *et al.* (1981) describes it as  $\text{Al}_{(\text{t})} \rightarrow [\text{Si}: + (\text{Fe}^{2+} + \text{Mg}^{2+})]$  (Fig. 29b).

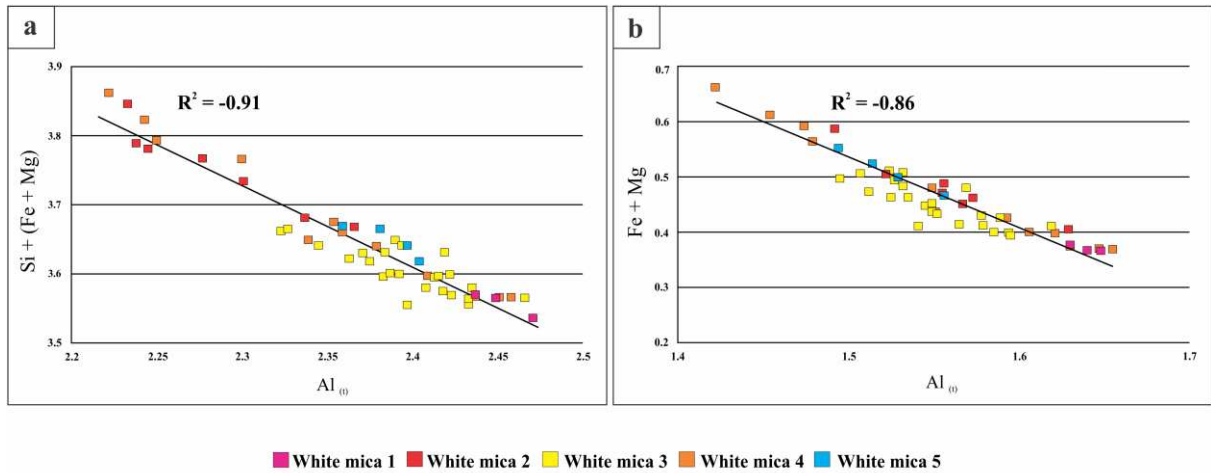


**Figure 29:** a) Correlation diagram  $Al^{VI}$  vs  $(Fe + Mg)$ ; and b)  $Al_{(VI)}$  vs  $[Si + (Fe + Mg)]$  for the white micas from the Paraíba deposit.  $R^2$  = Correlation coefficient.

Another useful diagram which shows variations in the white mica composition is the ternary diagram proposed by Velde (1985) which use a Muscovite-Phengite-Celadonite solid solution line (Fig. 30). Thus, the "White Mica 1" presents muscovite tending to illite composition, whereas the "White Mica 2" presents varied composition, from muscovite to phengite. The "White Mica 3" presents an intermediate composition, while the "White Mica 4" has an intermediate to phengite composition. Finally, the "White Mica 5" presents an intermediate composition between normal potassic Muscovite to phengite.

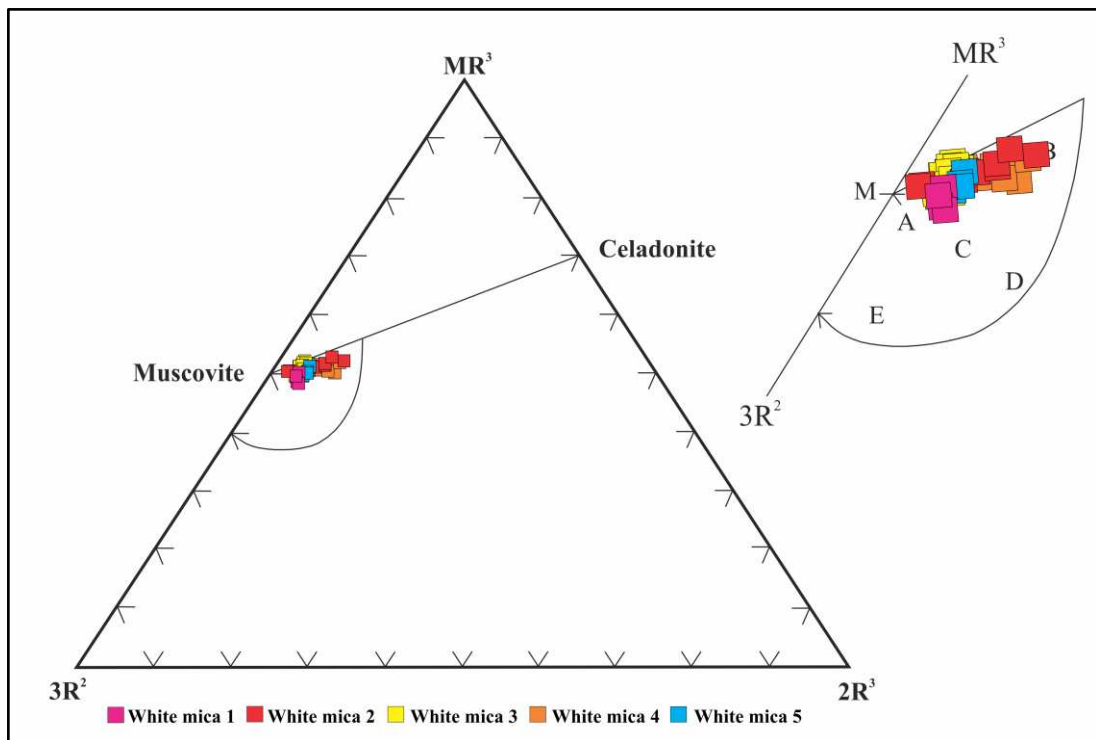


**Figure 30:** Representation of the Paraíba white micas chemical composition using the  $MR^3 - 2R^3 - 3R^2$  diagram proposed by Velde (1985). (M = Muscovite; A = Magmatic Micas; B = Phengites; C = Illites; D = Illites associated with Chlorite; E = Illite in sandstones, in the first

stages of weathering and in hydrothermal events of granitic rocks.  $MR^3 = Na+K+2Ca$ ;  $2R^3 = (Al_{(t)} - MR^3)/2$ ;  $3R^2 = (Fe+Mg)/3$ .

The ternary diagram proposed by Guidotti (1987) shows the white mica composition in function of the  $Al^{IV}$  -  $Al^{VI}$  -  $Fe_{(t)} + Mg$  contents (Fig. 31), where the "White Mica 1" presents a muscovite composition, given the low exchange of Fe or Mg and Al. The "White Mica 3 and 5" have a phengite tending to a ferri-muscovite composition. The "White Mica 2" and "4" are phengite with a tendency toward ferri-phengite, indicating Fe and Mg enrichment.

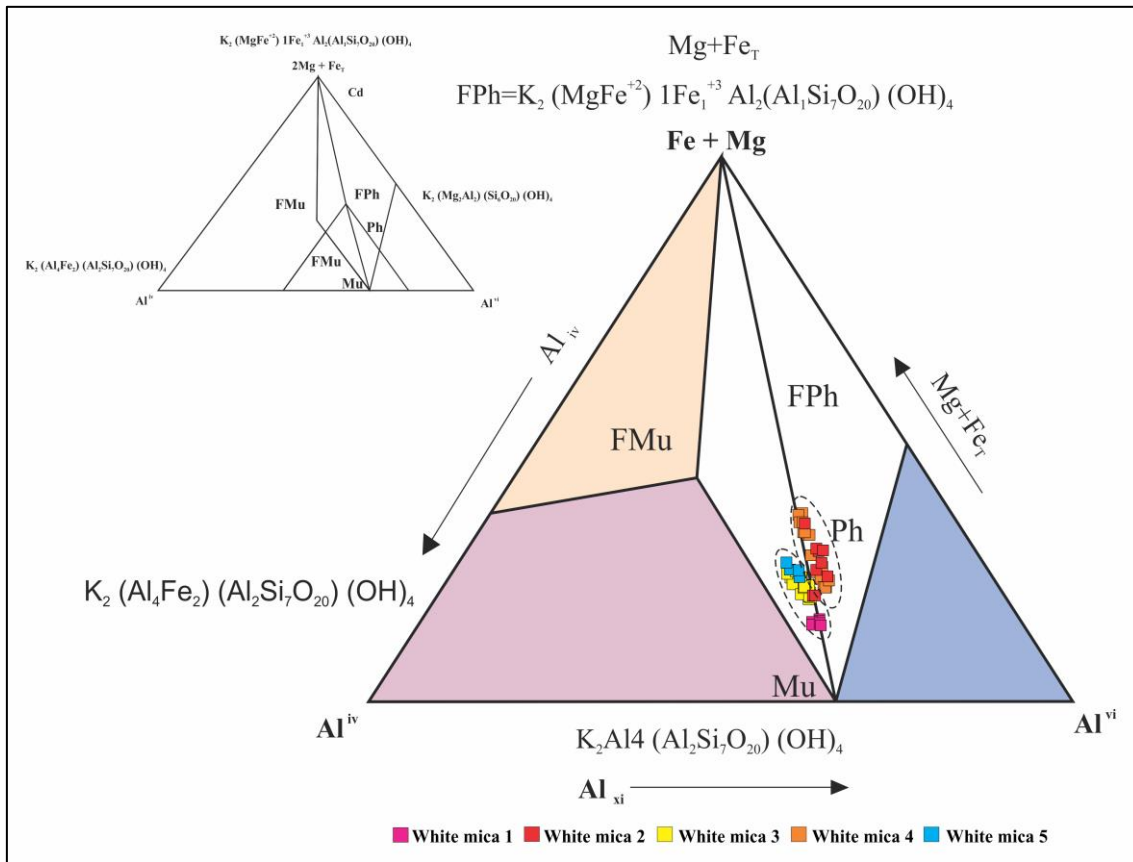


**Figure 31:** Representation of the Paraiba white micas chemical composition using the  $Al^{IV}$  -  $Al^{VI}$  -  $Fe_{(t)} + Mg$ , ternary diagram proposed by Guidotti (1987). It is possible to see the same two compositional clusters previously observed in figure 28. FMu = Ferri-Muscovite; Mu = Muscovite; Ph = Phengite; FPh = Ferri-Phengite; Mu = Muscovite.

## 6.2. Biotite – Phlogopite

Some points in biotite crystals host by the phyllonite were analysed with the electron microprobe, with a base of 11O, aiming to determine the hydrothermal biotite compositional variations in contrast with the igneous biotite belonging to the Paraiba tonalite.

Two points were excluded from the analysis because they were out of the compositional interval study range of 91.24 to 96.71 wt%. Values below 91.24% suggest high amounts of structural water or a high altered crystal.

A total of six samples corresponding to the Paraíba main section were analysed for biotite. Thus, for the bore-hole 020, the samples 019 and 027 were chosen, related to the "Paraibinha" and "Paraíba" veins, respectively. The first one, located at 95 m depth from surface, presents fine to medium-grained biotite crystals with sizes between 40 and 100  $\mu\text{m}$  and Fe, Mg and Ti contents of 0.79, 1.86 and 0.01 a.p.f., respectively. The 027 sample, located at 145 m depth from surface presents crystal biotite sizes between 100 and 200  $\mu\text{m}$  and Fe, Mg and Ti contents of 0.81, 1.74 and 0.02 a.p.f. respectively. For the bore-hole 041 were analyzed the samples 003 and 016. The first one, related to the Paraíba tonalite, is located at 70 m depth from surface, presents subhedral biotite crystals with sizes between 400 to 1500  $\mu\text{m}$  and Fe, Mg and Ti contents of 1, 1.48 and 0.13 a.p.f. respectively. The sample 016, related to the "Paraibinha" phyllonite, is located 325 m depth from surface and presents zoned biotite crystals with 80 to 300  $\mu\text{m}$  in size. Electron microprobe analysis shows clear sectors with Ti-Al-rich and low Mg sectors (0.03 a.p.f. of Ti, 1.0 of Al and 2.2 of Mg) and dark sectors with Mg-high and Ti-Al-low (0.002 a.p.f. of Ti, 0.75 of Al and 2.4 of Mg). Finally, the borehole 059 is represented by the samples 041 and 046. The first one, located 272 m depth from surface, presents medium-grained biotite crystals with sizes between 100 and 150  $\mu\text{m}$  and Fe, Mg and Ti contents of 0.67, 2.11 and 0.01 a.p.f. respectively. The sample 046 is located 340 m depth from surface, presents fine biotite crystals with approximate 40  $\mu\text{m}$  size and Fe, Mg and Ti contents of 0.82, 1.90 and 0.01 a.p.f. respectively.

All the biotite samples were compared and analysed using the  $\text{Al}^{\text{IV}}$  vs #Fe Tamizel (2014) diagram (Fig. 32). It was observed that all the phyllonite biotite crystals present low Fe/(Fe + Mg) ratio, suggesting high Mg contents in comparison to the igneous biotite (BH041-003 sample). Almost all the analysed crystals have a phlogopite composition and present variations depending on the phyllonite in which the sample was taken and its depth.

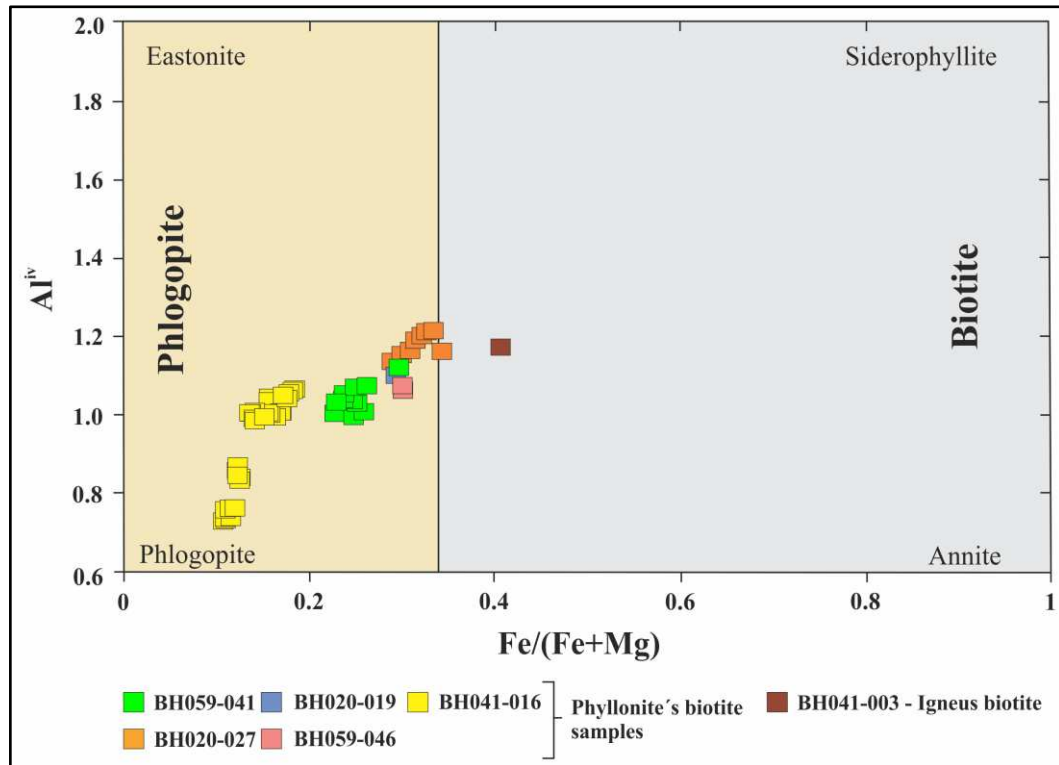


**Figure 32:** Representation of the Paraíba's biotite and phlogopite chemical composition using the  $Al^{iv}$  vs  $Fe\#$  diagram proposed by Tamizel (2014).

According to nomenclature proposed by Foster (1962), the classification for these trioctahedral micas can be defined using the  $Mg - (Al^{VI} + Fe^{3+} + Ti) - (Fe^{2+} + Mn)$  ternary diagram (Fig. 33). As seen in the previous diagram, it is observed that the igneous biotite (BH041-003 sample) is classified as Mg-rich biotite. Besides, there is a large group with a transitional composition between Mg-rich biotites to phlogopite and one group with a clear phlogopite composition.

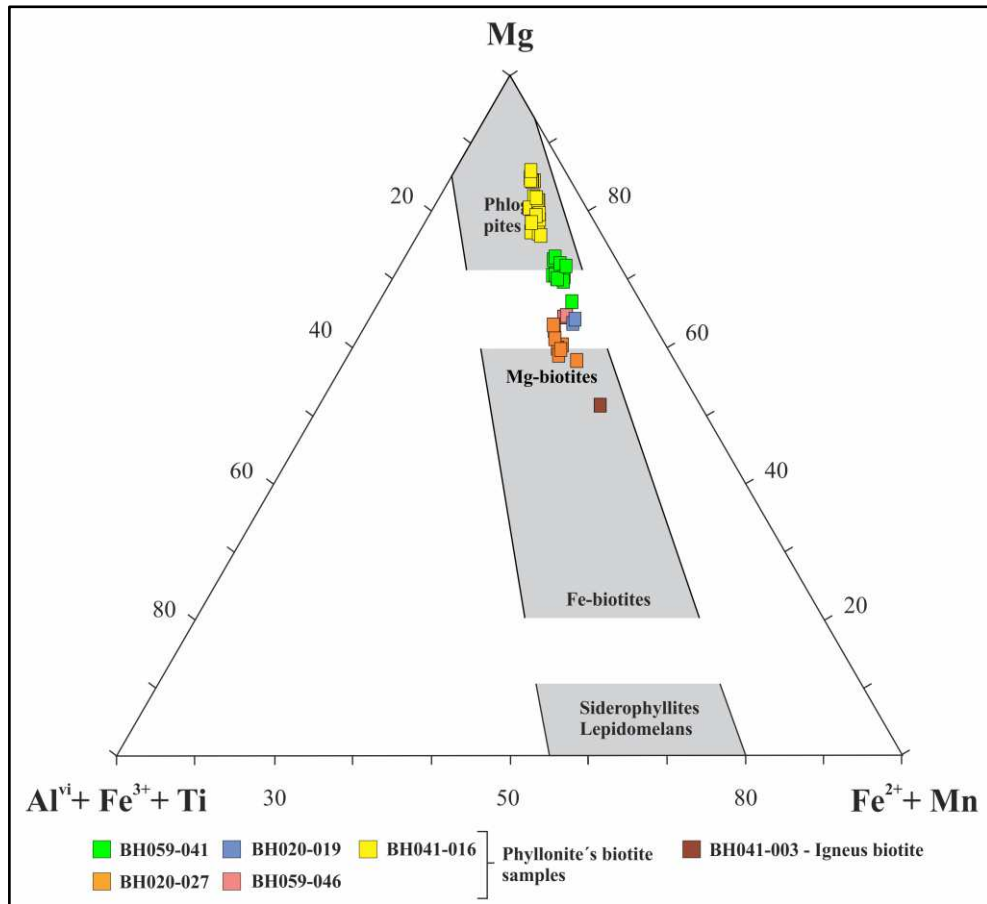


**Figure 33:** Representation of biotite and phlogopite from Paraíba deposit chemical composition using the ternary diagram of classification of trioctahedral micas given by Mg - ( $\text{Al}^{\text{VI}} + \text{Fe}^{3+} + \text{Ti}$ ) - ( $\text{Fe}^{2+} + \text{Mn}$ ) proposed by Foster (1962).

Finally, the same samples were analysed with the ternary diagram proposed by Nachit *et al.* (2005). It was used  $10 \times \text{TiO}_2 - (\text{FeO}_{(\text{i})} + \text{MnO}) - \text{MgO}$  as end-members to analyse and distinguish primary biotite from others re-equilibrated and secondary ones (Fig. 34). This diagram indicates that the igneous biotite has a re-equilibrated to primary biotite composition, indicating that those grains were altered. On the other hand, the Mg-rich and Ti-poor phyllonites biotite crystals are within the secondary and re-equilibrated biotite zone.

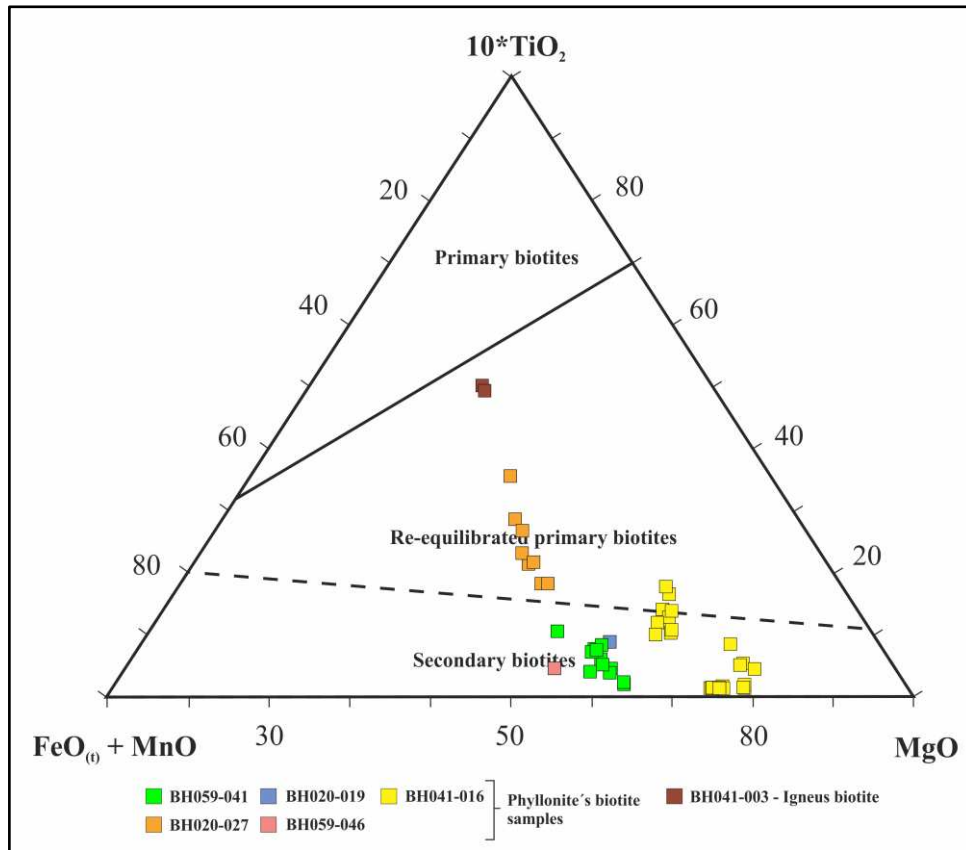


**Figure 34:** Representation of the Paraíba's biotite and phlogopite chemical composition using the ternary diagram proposed by Nachit *et al.* (2005), that allow distinguishing igneous primary biotite from re-equilibrated and secondaries ones.

### 6.3. Epidote

The epidote is considered of great importance within the Paraíba deposit due to its relationship with the mineralized zones. In this way, 12 epidote crystals were analysed with electron microprobe, with a base of 12.5 O, aiming to determine compositional variations among different hydrothermal alterations zones. The analysed epidote crystals are related to the propylitic alteration (sample BH041-003) and the epidotization. For this latter, crystals associated with the hydrothermal breccia matrix (sample BH041-012) and with the phyllonite (sample BH059-046) were analysed. The sample BH041-003 presents anhedral to subhedral epidote crystals, sizes between 25 and 100  $\mu\text{m}$  and Fe and Al contents of 0.85 and 2.18 a.p.f respectively. The epidote of the BH041-012 sample is anhedral, with sizes that rarely exceed 25  $\mu\text{m}$  and Fe and Al contents of 0.85 and 2.16 a.p.f respectively. For its part, the BH059-046 sample presents prismatic epidote crystals with great sizes, from 100 to 750  $\mu\text{m}$ , and Fe and Al contents of 0.80 and 2.21 respectively.

According to Kartashov (2014), the epidote crystals of BH041-003 (tonalite-propylitic alteration) and BH041-012 (breccia-epidotization) samples have a classical epidote composition with similar amounts of Fe and Al in their structure. However, the sample BH059-046 (phylionite-epidotization) presents epidote crystals with varied composition, some of them have Al-high and Fe-low, indicating a compositional tendency towards the epidote clinozoisite variety (Fig. 35).

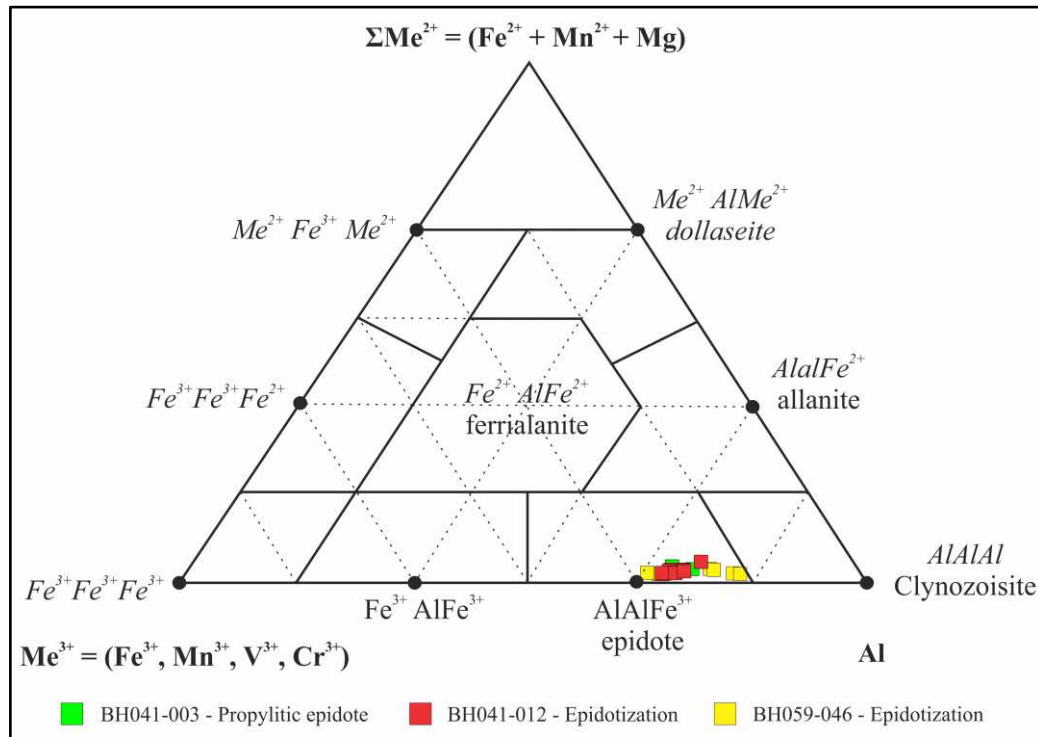


**Figure 35:** Representation of the Paraíba's epidote chemical composition using the ternary diagram proposed by Kartashov (2014).

#### 6.4. Chlorite

Chlorite crystals are closely related to mineralized zones, especially in phylionite areas. In this way, mineral chemistry studies by electron microprobe were carried out in the three chlorite groups previously described in the paragenetic table. The analyses were made on the base of 14 equivalent oxygen atoms, in an anhydrous base and separating the  $\text{Fe}^{2+}$  from  $\text{Fe}^{3+}$ . From a total of 49 measures in chlorite crystals, 11 of them were excluded from the analysis due to their abnormal Si content and their total weight percentage (wt%). According to that, lower values than 83.07 wt% imply highly altered crystals or large amounts of water in their structure. The Chlorite 1, associated with the alteration of biotite and phlogopite crystals from phylionite, are anhedral to subhedral, with sizes between 120 and 200  $\mu\text{m}$  and Fe and Mg contents of 1.42 and 3.16 a.p.f respectively. The Chlorite 2, related to the

propylitic alteration, is anhedral to subhedral, with grain sizes from 200 to 750  $\mu\text{m}$  and Fe and Mg contents of 1.72 and 2.87 respectively. The Chlorite 3, associated with the final evolution stage, is subhedral to euhedral, with greater sizes, between 200  $\mu\text{m}$  and 1 mm, and Fe and Mg contents of 1.43 and 3.32 respectively.

Using the Si vs  $\text{Fe}^{2+}/(\text{Fe}^{2+} + \text{Mg}^{2+})$  diagram, proposed by Foster (1962), it was possible to determine a Brunsyigite to slightly Ripidolite composition for Chlorite 1; a compositional trend from Ripidolite to Diabanite and a greater Fe/(Fe+Mg) ratio for Chlorite 2; and a Brunsyigite to Diabanite composition, with light enrichment in Mg for Chlorite 3 (Fig. 36).

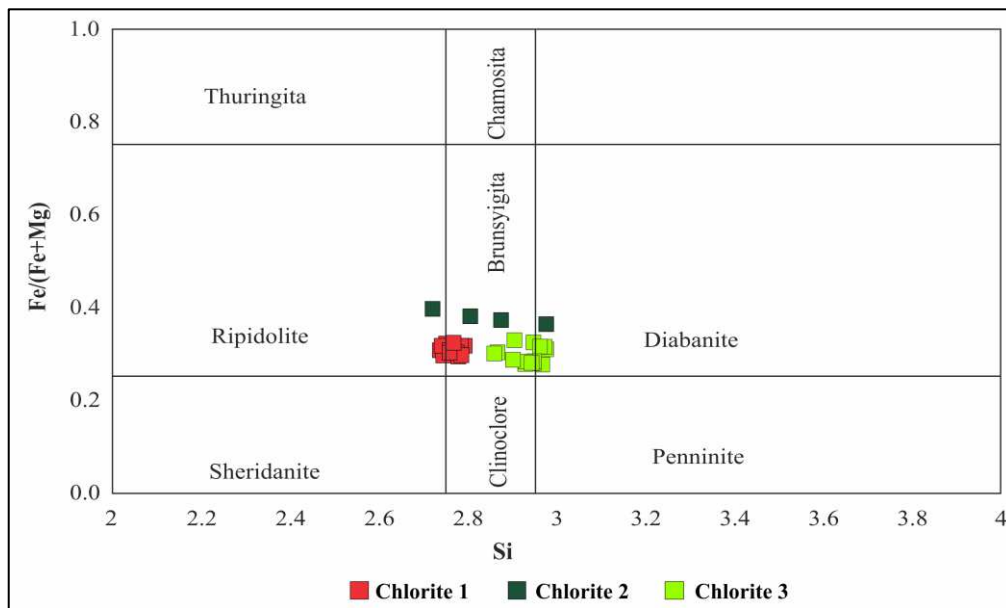


**Figure 36:** Representation of the chlorite's composition from the Paraíba deposit according to the ratio proposed by Foster (1962) between Si vs  $\text{Fe}^{2+}/(\text{Fe}^{2+} + \text{Mg}^{2+})$ .

The data was also plotted into the  $\text{Fe}^{2+}/(\text{Fe}^{2+} + \text{Mg}^{2+})$  vs  $\text{Al}^{\text{IV}}/(\text{Si} + \text{Al}^{\text{IV}})$  diagram proposed by Ciesielczuk (2012) (Fig. 37). According to it, the Chlorite 1 is within the field of Fe-Al chamosite; Chlorite 2 presents a compositional trend from Fe-rich clinocllore to Fe-Al rich chamosite; and Chlorite 3 has a similar pattern but with a lower Fe/(Fe+Mg) ratio, indicating greater Mg quantities in its structure.

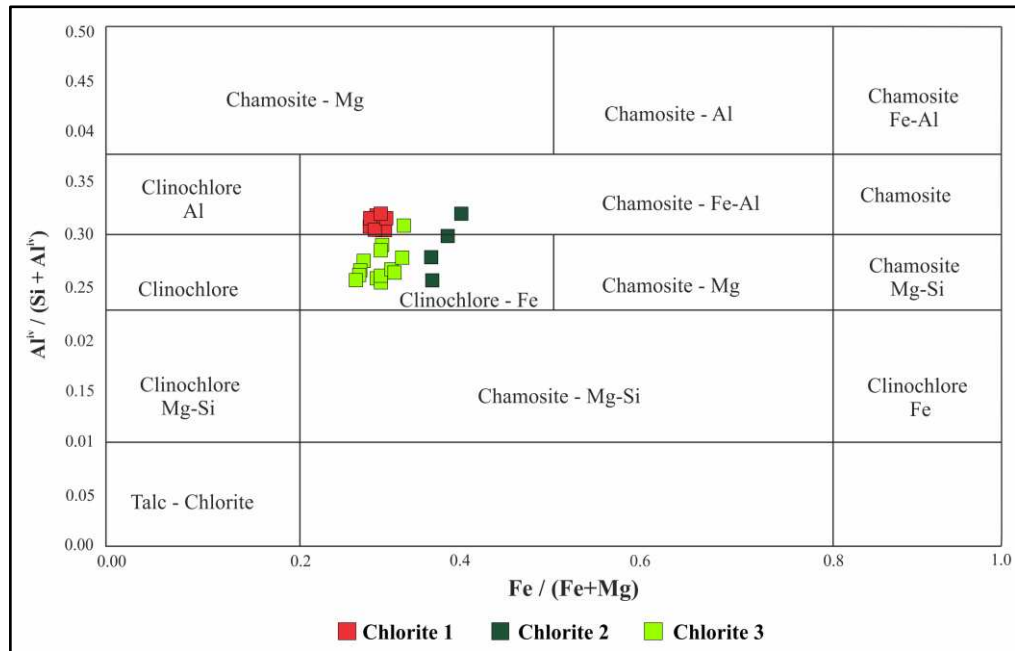


**Figure 37:** Representation of the chlorite's composition from the Paraíba deposit according to the ratio proposed by Ciesielczuk (2012) between  $\#Al^{IV}$  vs  $\#Fe$ .

According to Foster (1962), variations in FeO and MgO concentrations in the chlorite groups, involve substitution of  $Fe^{2+}$  for  $Mg^{2+}$  in the octahedral layers as a consequence of the mineralizing fluid composition and the oxygen fugacity ( $f_{O_2}$ ). This cation substitution was recognized by a negative linear correlation between the chlorite samples. Thus, the Chlorite 1 and 3 present an intermediate Mg-Fe composition, whereas the Chlorite 2 presents a Fe-Mg intermediate composition (Fig. 38).

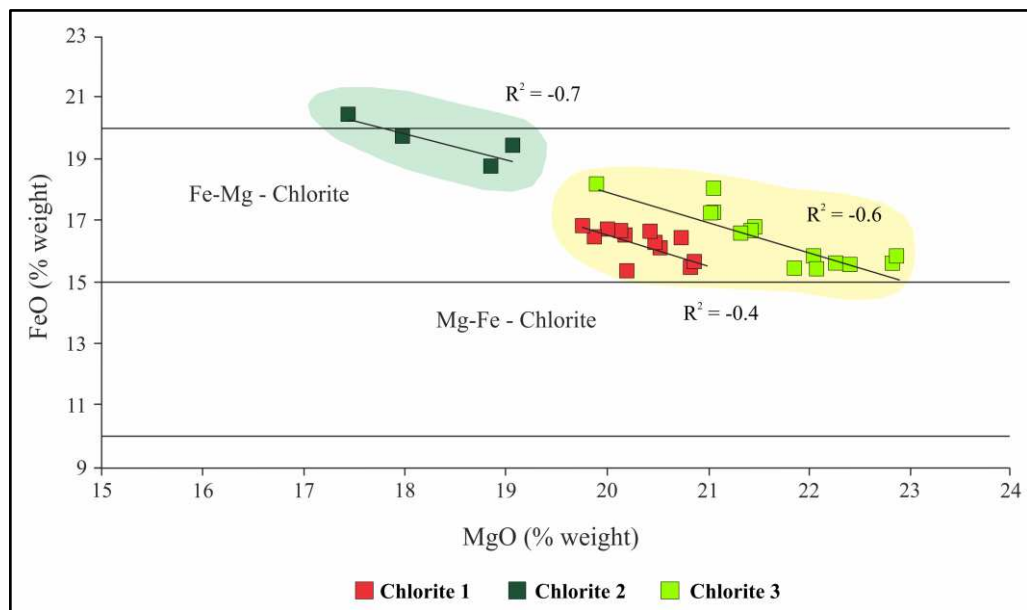


**Figure 38:** Representation of the variations in the concentration of FeO and MgO in the group of chlorites, implying the substitution of  $Fe^{2+}$  by  $Mg^{2+}$  in the octahedral layers, according to Foster (1962).

The  $\text{Al}^{\text{IV}}$  content in the chlorites of the Paraíba deposit varies from 1 to 1.28, and the ratios  $\text{Fe}/(\text{Fe} + \text{Mg})$  range between 0.28 and 0.39. According to Foster (1962), values close or equal to 1 in the  $\text{Al}^{\text{IV}}/\text{Al}^{\text{VI}}$  ratio indicate the substitution of Si for  $\text{Al}^{\text{IV}}$ , while the content of  $\text{Al}^{\text{IV}}$  is directly proportional to the  $\text{Fe}/(\text{Fe} + \text{Mg})$  ratio (Fig. 39). This substitution was also recognized by Zang and Fyfe (1995).

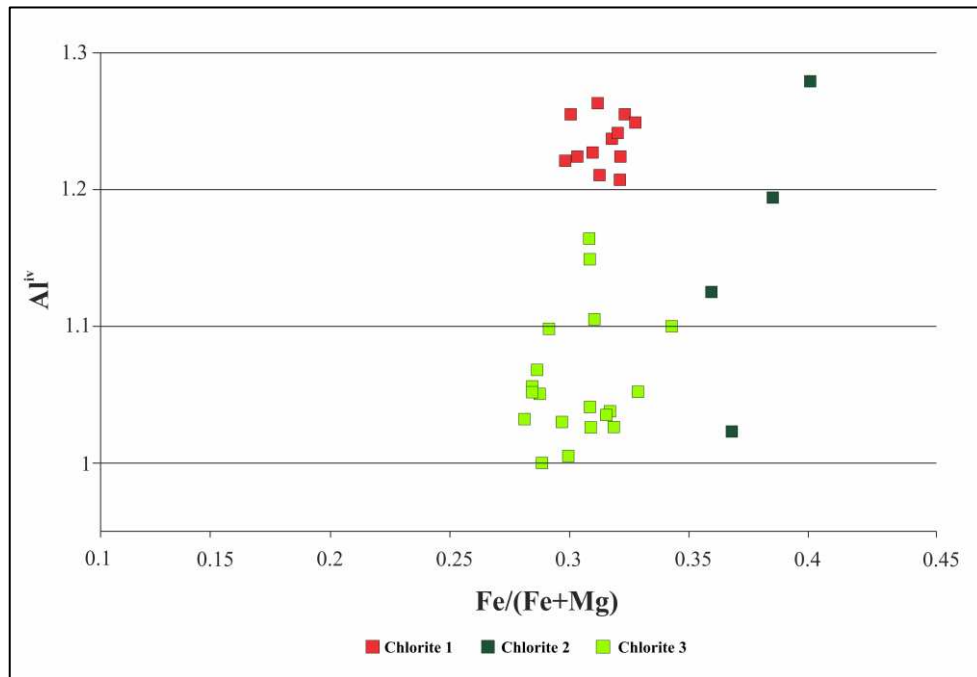


**Figure 39:** Correlation diagram between  $\text{Fe}/(\text{Fe} + \text{Mg})$  vs  $\text{Al}^{\text{IV}}$  for chlorite samples from the Paraíba deposit, according to Foster (1962) and Zang and Fyfe (1995).

#### 6.4.1. Chlorite crystallization temperature

The chlorite crystallization temperatures were calculated following the recommendations and equations of Bourdelle *et al.* (2013) and Inoue *et al.* (2009). Both consist of semi-empirical methods that do not consider pressure and non-ideal conditions, were created and for temperatures up to 350-400 °C and an error of  $\pm 20$  °C degrees is expected in their estimates. These geothermometers are based on the end-member ratio activities to directly relate the temperature to the constant equilibrium between quartz and chlorite.

Inoue *et al.* (2009) chose the magnesian endmembers of Al-free Mg-chlorite, conrundophilite and sudoite, and the ferrous endmember of chamosite, while Bourdelle *et al.* (2013) chose the magnesium and ferric endmembers of Al-free chlorite, amesite and sudoite.

Following the Inoue *et al.* (2009) considerations, there were obtained the crystallization temperatures for the three chlorite groups (Fig. 40). The Chlorite 1 (n=12 measures), presents low variations between the maximum and minimum temperature and a geometric mean temperature at 396 °C. The Chlorite 2 (n=4 measures), presents the widest range of temperatures among the three groups and a geometric mean temperature at 314 °C. Finally, the Chlorite 3 group (n=23 measures), presents intermediate temperatures, with a geometric mean of 334 °C.

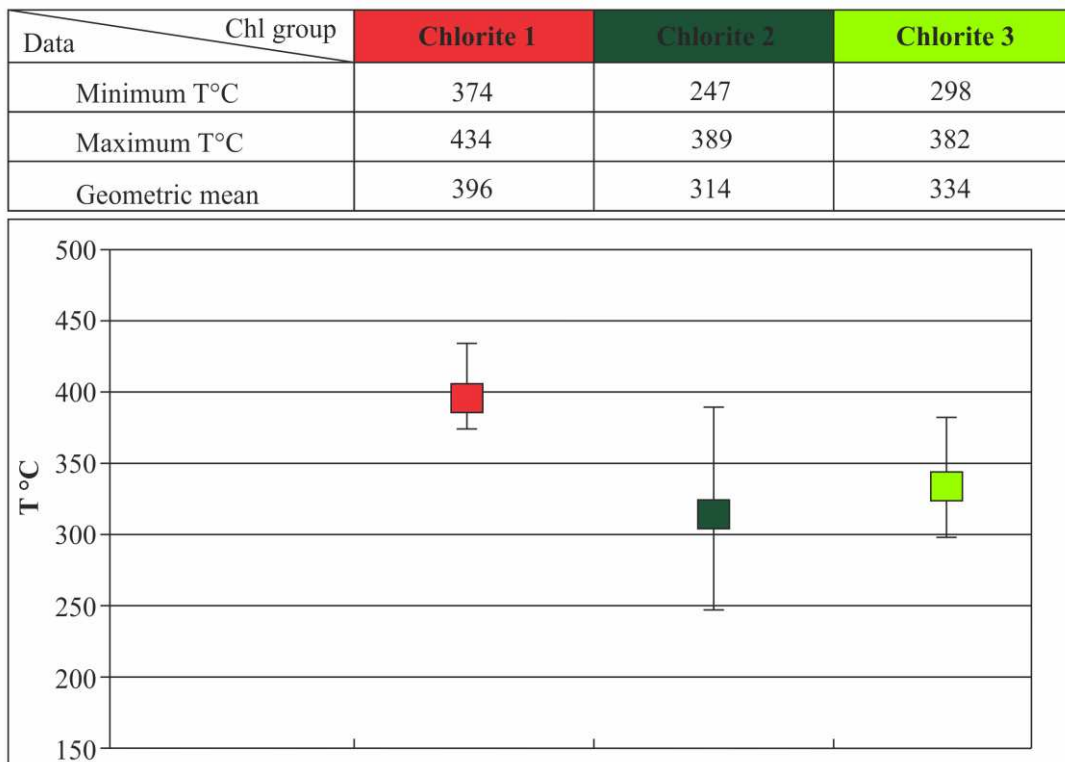


**Figure 40:** Chlorites crystallization temperatures from the Paraíba deposit, calculated using the Inoue *et al.* (2009) geo-thermometer.

On the other hand, temperatures can be calculated following the recommendations proposed by Bourdelle *et al.* (2013) and using the Si vs  $R^{2+}$  diagram proposed by Wiewióra and Weiss (1990), in which  $R^{2+}$  is the sum of  $Fe_{(t)} + Mg + Mn + Ca$ . The results are presented in figure 41, presuming that, in comparison with the data obtained by Inoue *et al.* (2009), both methods are concordant.

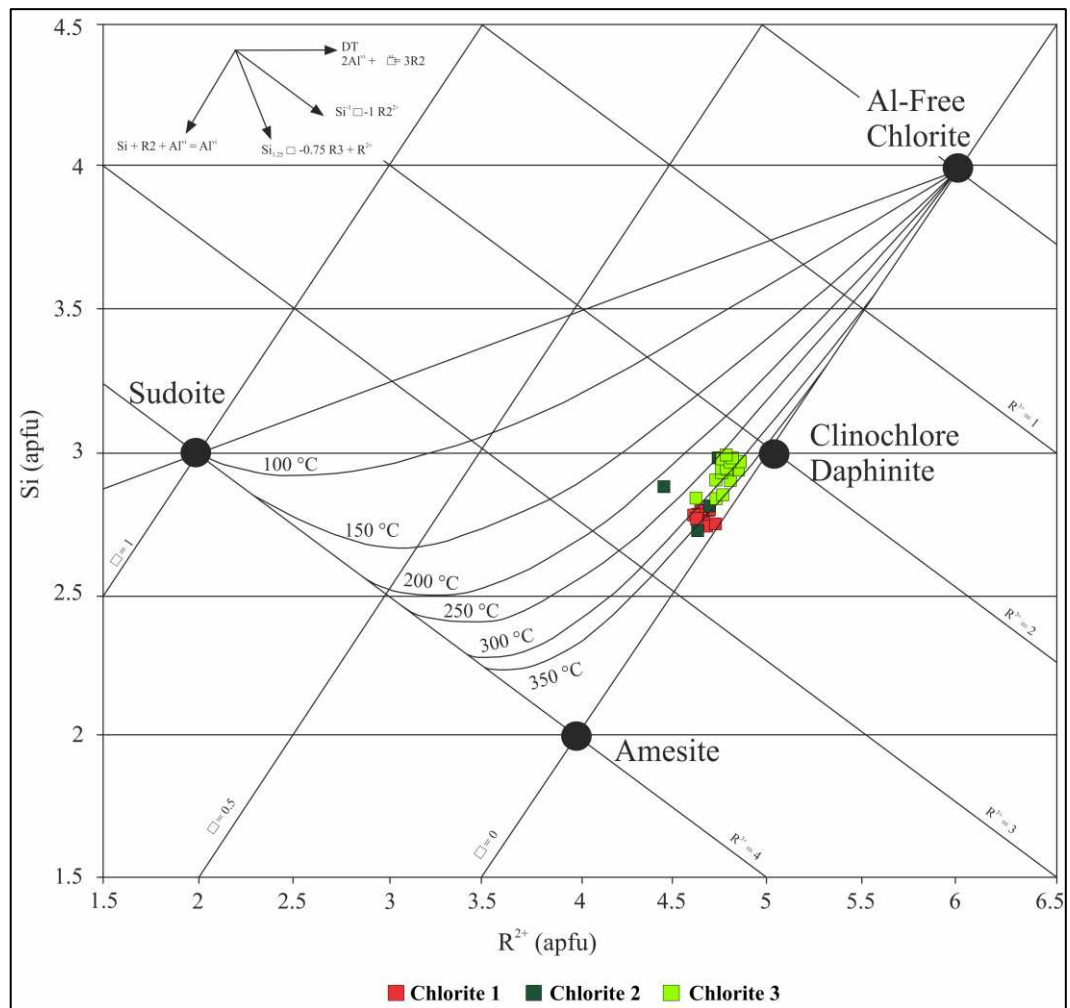


**Figure 41:** Chlorites crystallization temperatures from the Paraíba deposit, calculated using the Bourdelle *et al.* (2013) geo-thermometer on Wiewióra and Weiss (1990) diagram.

## 7. DISCUSSION

### 7.1. Reflectance spectroscopy

#### 7.1.1. White mica

Spectrum-mineralogical analysis of white micas in the bore-holes 020, 041 and 059 allowed the identification of a variation in the absorption position, with values from 2196 to 2225 nm. Two chemically distinct white mica populations were determined from the analysis of a histogram correlating the number of samples with absorption position (Fig. 42). A smaller group with a composition varying from tending to paragonite (2196 nm) to normal potassic (2208 nm) and a larger group with a normal potassic (2208 nm) to phengite composition (2225 nm). The higher Au values are related to the largest group, especially at the tail end of the Gaussian curve, between 2214 and 2225 nm (Fig. 42a). Higher Cu contents are also related to this group, but are homogeneously distributed along the Gaussian curve (Fig. 42b).

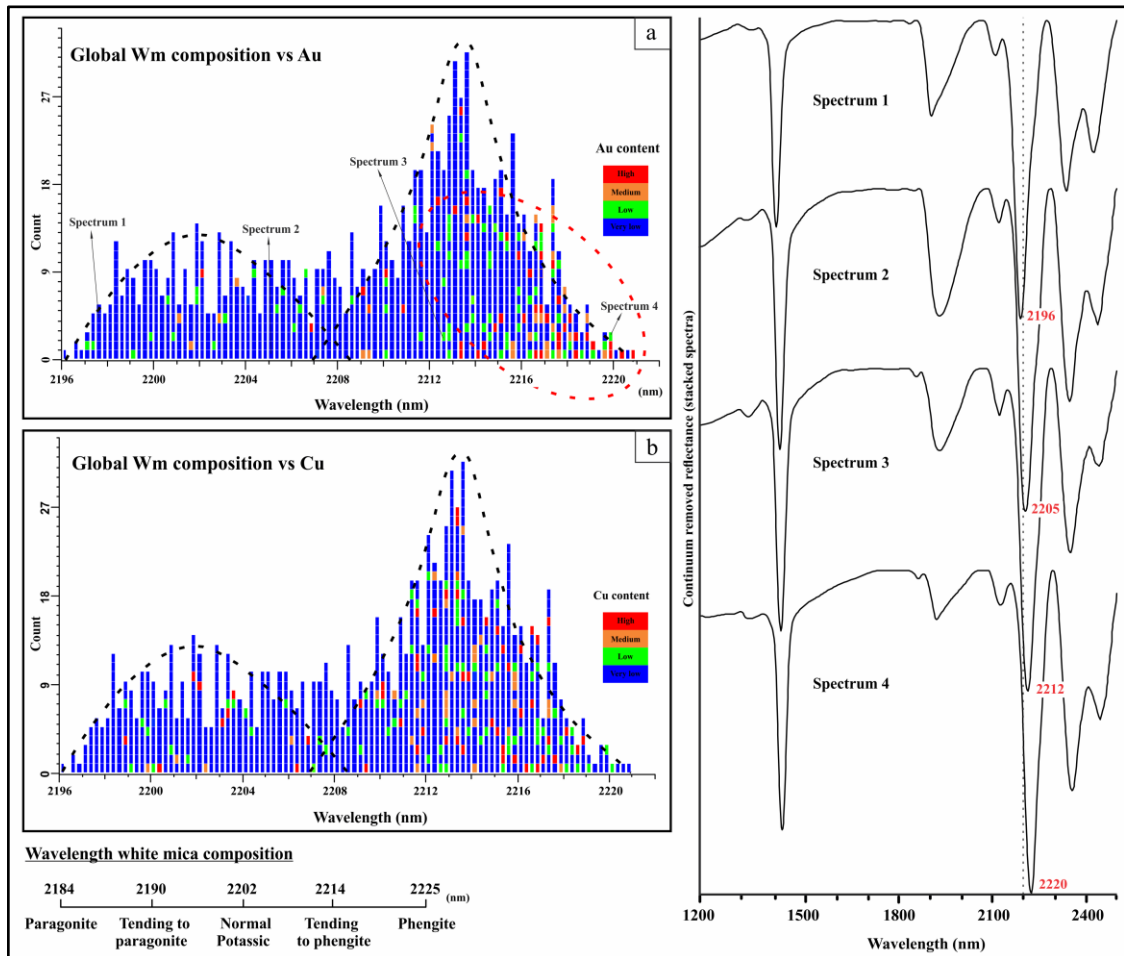


**Figure 42:** a) Histogram of white mica composition for all samples analysed and Au content in colours. It shows the relationship between the two groups and the higher Au values,

evidencing a trend in wavelengths from 2214 to 2224 nm; b) Histogram of white mica composition for all samples analysed and Cu content in colours. It shows a better correlation with the larger group but it was not possible to observe a specific trend with the highest Cu values. The spectra of white mica with different composition are show at right.

In the Paraíba deposit, the CI increases in the mineralized zones, due to the significant temperature increment, reaching low (>4 CI) to very low (>9 CI) water contents in the muscovite crystalline structure. The calculated CI limits were up to 0.5 for pure smectite, from 0.5 to 1 for smectite/illite, 1 to 2 for illite/smectite, 2 to 4 for pure illite and finally 4 to 15 for pure muscovite (Fig. 43).

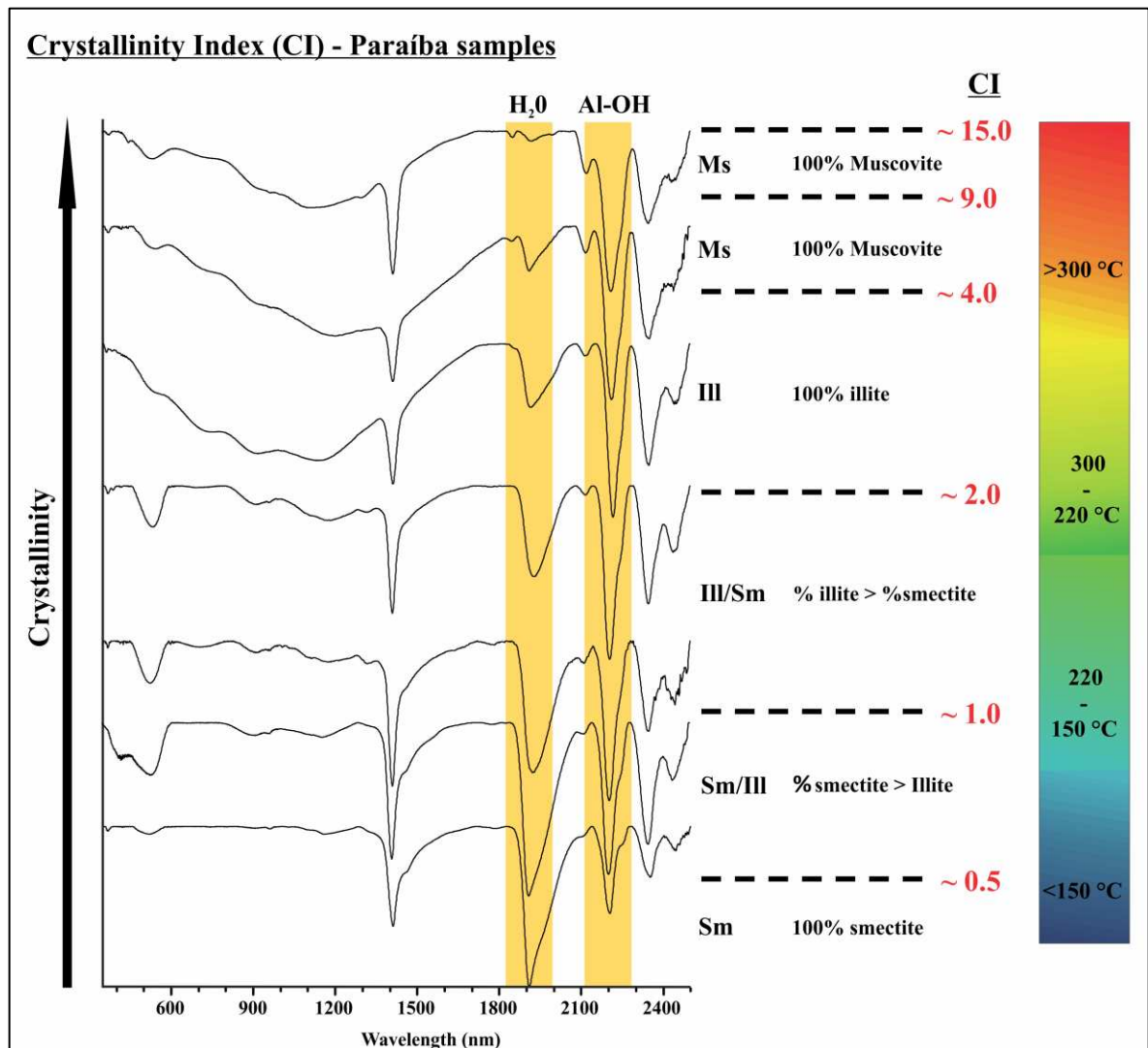


**Figure 43:** White mica spectra of the Paraíba deposit with different crystallinities and different mixture proportions of illite-smectite interstratifications. The crystallinity index (CI) limit values are shown in red, calculated by ratioing the depth of Al-OH absorption at 2200 nm by the water absorption at 1900 nm (based on Pontual *et al.* 2008 and Ducart and Stolf, 2018).

For a better analysis, the borehole BH041, which better represents the Paraíba deposit, was studied to examine the white mica abundance, composition, and crystallinity

variation. The Striplog, shown in figure 44, exhibits these parameters according to the depth and its correlation with Au and Cu values.

Along the BH041 were found 6 zones with great economic importance. Five of them are related to Au quartz veins and the other to the hydrothermal breccia (Table 5).

Depth interval (m)	Alteration zone	Max Au (ppb)	Average Au (ppb)	Max Cu (ppm)	Average Cu (ppm)
60 - 120	Quartz vein	1644	41	450	45
210 - 250	Breccia	212	23	2900	300
300 - 320	Quartz vein	100	37	190	90
340 - 350	Quartz vein	100	38	110	60
360 - 380	Paraibinha quartz vein	3264	325	343	80
400 - 420	Paraíba quartz vein	31325	2490	1800	345

**Table 5:** Location of the 6 zones of interest of the borehole BH041 and the hydrothermal alteration associated.

Analysing the automatic recognition graphic (“TSG-summary”), created with TSG 8 software, it is possible to recognise the general mineralogy of the borehole. At first glance, it is clearly discerned the regolith layer by the kaolinite occurrence. The presence of biotite, phlogopite, and chlorite are evidencing the phyllonite, while epidote-rich zones are related to the breccia lithotype. In general, it is observed a high presence of white mica all along the borehole.

White mica analysis reveals an abundance increase in all zones, especially in the breccia zone, which is characterized by the presence of “White Mica 4”, related to the sericitic alteration (Fig. 21). The Au quartz veins present relative white mica abundance as it is formed from phyllonite biotite and phlogopite crystals alteration, so its abundance is directly related to the hydrothermal alteration intensity. Additionally, the abundance data was correlated to the white mica composition, established from the 2200 nm flexion position. Thus, it was possible to observe that the phengite mica abundance increase with absorption features between 2210 and 2225 nm (White mica 2), is associated with the Au-rich quartz veins, and the tending to phengite to phengite mica with absorption features between 2213 and 2221 nm (White mica 4) is associated with the brecciated zone. In addition, the Au and Cu-rich zones present an increase in white mica crystallinity index, evidencing zones of higher temperatures within the system.

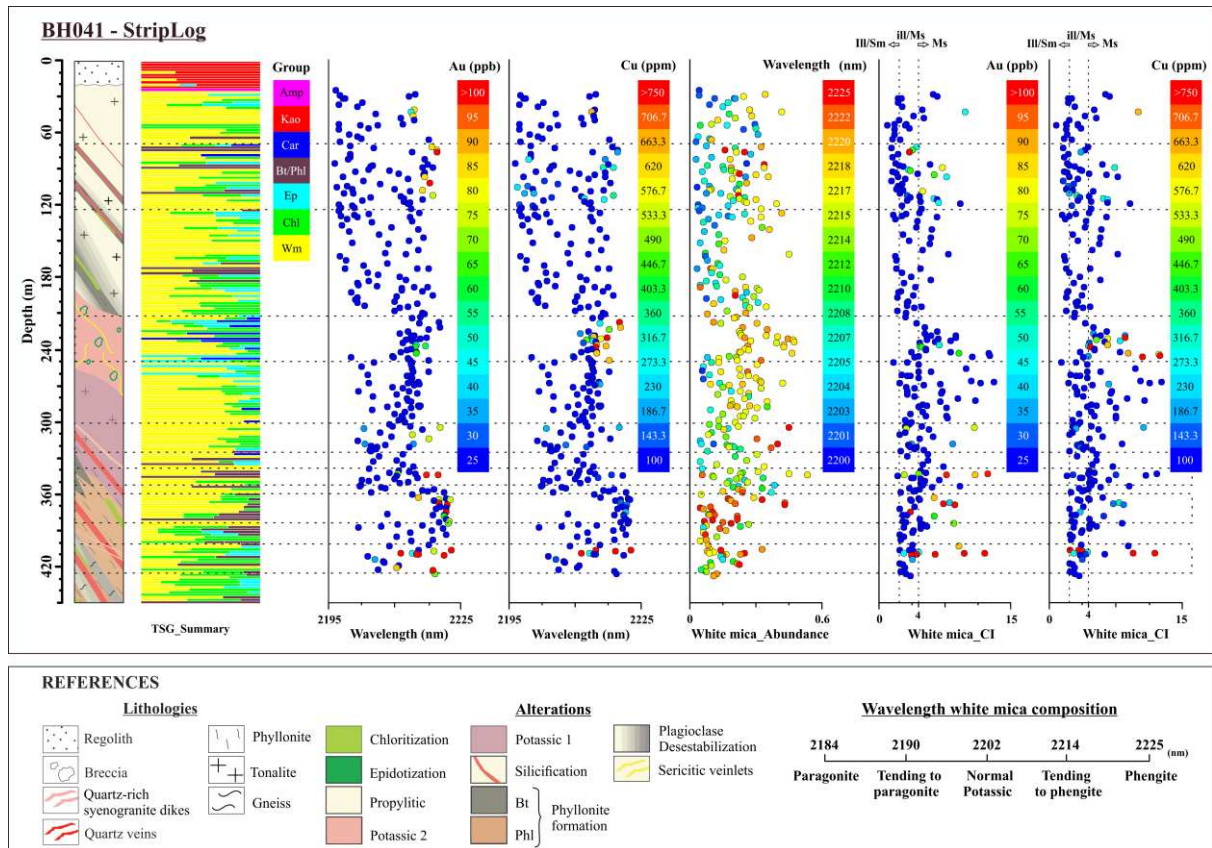


**Figure 44:** BH041 StripLog, showing the relationship between the white mica spectral parameters, the Au-Cu values, and their association with the main hydrothermal alterations and the summary TSG 8 interpretation.

The separation and interpretation of the five white mica groups in the bore-hole 041 strip-log were only possible with the integration of spectral techniques, petrography and electron microprobe (Fig. 45). White mica 1 is present in the first meter of the borehole up to a depth of 180 m, with wavelengths between 2198 and 2207 nm and without a relationship with the mineralization. White mica 2 has a considerably spectral range, from 2210 to 2225 nm, with tending to phengite to phengite composition. Although, this is the unique white mica group that has principal absorption features higher than 2221 nm, make them easy to identify and being useful as a vector to mineralized quartz veins. White mica 3 has wavelengths between 2207 and 2215 nm and do not have any relationship with the mineralization. White Mica 4 present a phengite composition with wavelengths from 2213 to 2221 nm, and, similar to White Mica 2, has great importance as a vector for Cu and Mo-rich zones. Finally, White Mica 5, related to barren-late venules has a tending to phengite composition with feature absorptions positions between 2212 and 2214 nm, and do not have importance as a vector.

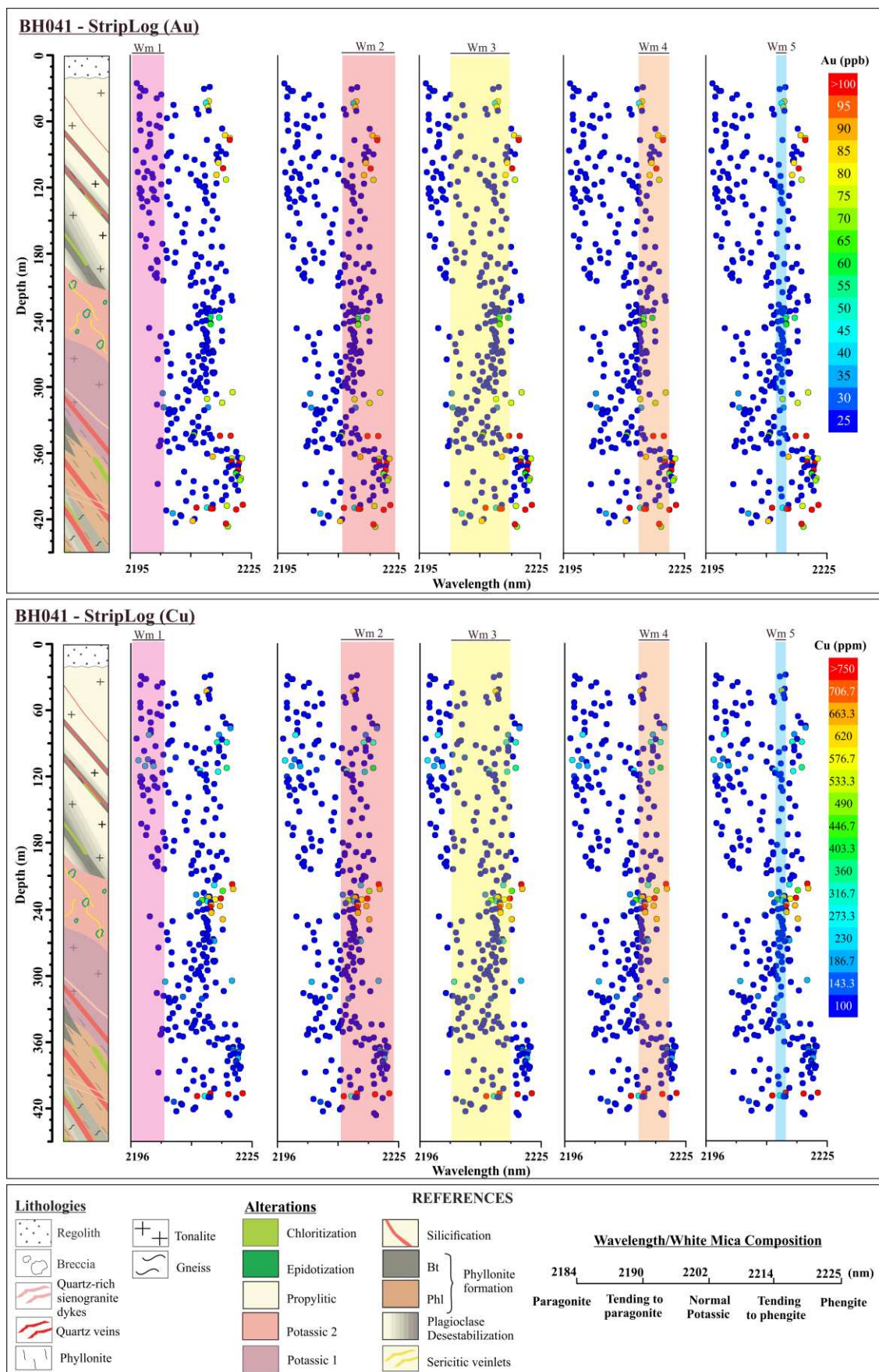


**Figure 45:** Strip-log from the borehole BH041, showing in detail the white mica composition and its relationship with the lithotypes, hydrothermal alterations and mineralization.

### 7.1.2. Chlorite

In the Paraíba deposit chlorite takes part of different alteration zones: (i) it is formed from the alteration of biotite and phlogopite crystals from phyllonite (“Chl 1”); (ii) is part of the propylitic alteration zones, which represent the most distal signature of mineralization, detectable hundreds of meters away from the main ore body (“Chl 2”); (iii) and also is part of the phyllonite 'pervasive' chloritization (“Chlorite 3”). Despite chlorite crystals occur late respect to mineralization it could be used as a vector as well, because it is located and altering phyllonites, which are related to ore zones (Bishop *et al.* 2008, Cudahy *et al.* 2010, Cooke *et al.* 2017).

Is possible to identify Mg- or Fe-rich chlorite using two absorption features: (i) the ~2250 nm feature between 2242 and 2262 nm (“FeOH” feature); and (ii) the ~2350 nm feature between 2325 and 2355 nm (“MgOH” feature). In both features, the increasing Fe content correlated with increasing wavelength (Neal *et al.* 2018).

In the Paraíba deposit, the chlorite is intimately related to epidote crystals, especially in areas with high propylitic alteration and present overlapping features in the region of 2350 nm. The obtained spectral analysis was plotted in histograms, evidencing an intermediate composition with a predominance of Mg-rich samples. These data are concordant with those observed with the mineral chemistry, in which the chlorite generated from the phyllonite alteration (“Chl 1”) and chlorites from the chloritization alteration (“Chl 3”) present Mg enrichment. Chlorite crystals generated from propylitic alteration (“Chl 2”) present Fe enrichment. In this sense, Chlorites 1 and 3, related to phyllonite areas, present correlation with high Au and Cu contents (Fig. 46a, b) and therefore can be used as a vector.

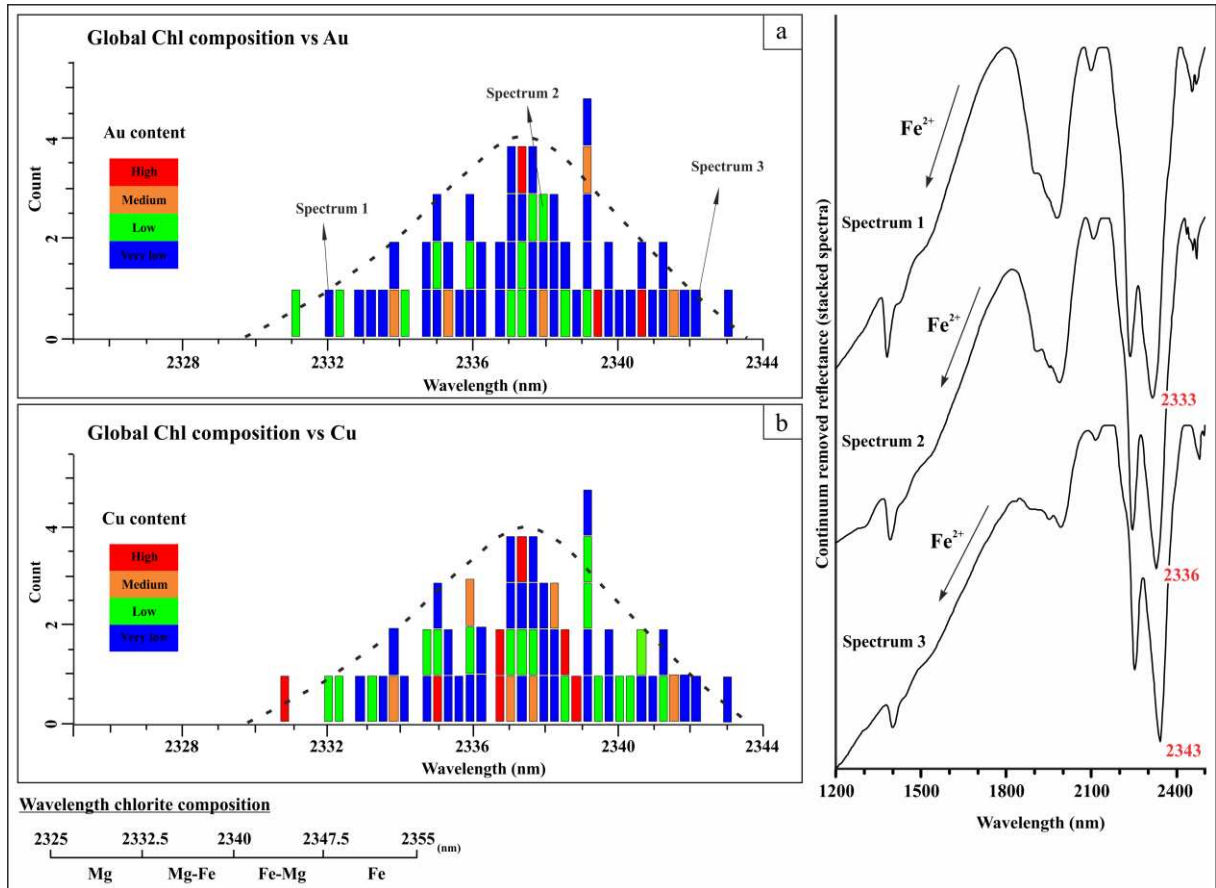


**Figure 46:** Global chlorite composition analysis according to wavelength position and their relationship with the Au and Cu values.

### 7.1.3. Epidote

Histogram plot of epidote absorption feature around 1545 nm shows an apparent spatial association with areas of copper mineralization (Fig. 47). A variation of 9 nm in the feature position was also observed, positioning almost all samples within the epidote field, while in some cases where the absorption feature reaches 1552 nm could be classified as clinozoisite according to Roache *et al.* (2011). This study also demonstrates a high correlation between the spectral data and the electron microprobe results (Fig. 35) and represent another mineral that could be used as a vector.

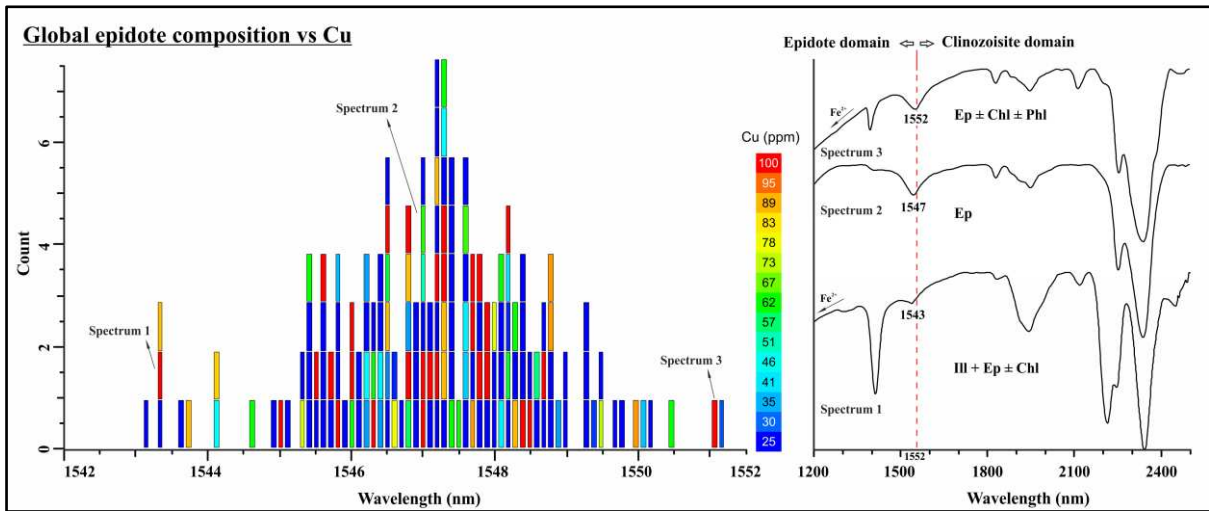


**Figure 47:** Global epidote composition analysis according to ~1550 wavelength position and their relationship with the Cu values.

## 7.2. Validating reflectance spectroscopy and mineral chemistry

Figures 48 and 49 show the correlation between main absorption wavelength positions of white mica and chlorite with cation contents. Thus, the 2200 nm feature was compared with the Al-OH bond and the cationic substitution of  $[\text{Si}^{4+} + (\text{Fe}^{2+} + \text{Mg}^{2+})]$ , whereas the 2340 nm feature was compared with  $\text{Mg}/(\text{Mg}/\text{Fe})$  and  $\text{Fe}/(\text{Fe} + \text{Mg})$  contents for white mica and chlorite, respectively.

Despite the similarities between Al and cation contents among all groups, it is possible to identify a linear relationship between such parameters. In Figure 48a, it is shown the longer wavelengths, the higher Si, Fe, and Mg contents, while in Figure 48b, it is observed that the Al-rich samples indicate minor cationic exchanges and therefore a minor crystalline structure weakening, showing absorption features in shorter wavelengths. On the other hand, Figure 49a shows that greater Mg values correlate with shorter wavelength feature position. In Figure 49b it is possible to recognise that when the Fe values increase, the wavelength feature position is longer.

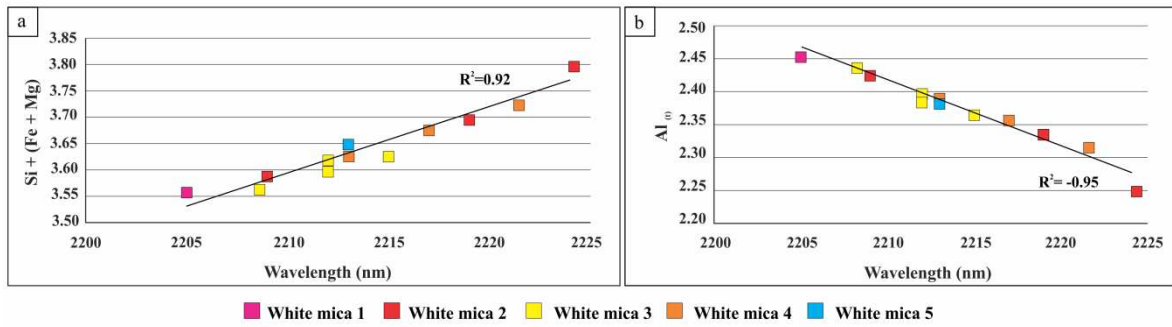


**Figure 48:** a) Correlation between Si + [Fe + Mg] and b)  $Al_{(IV)}$  contents of white mica (from EPMA data, for 110 atoms) and position of 2200 nm absorption feature.

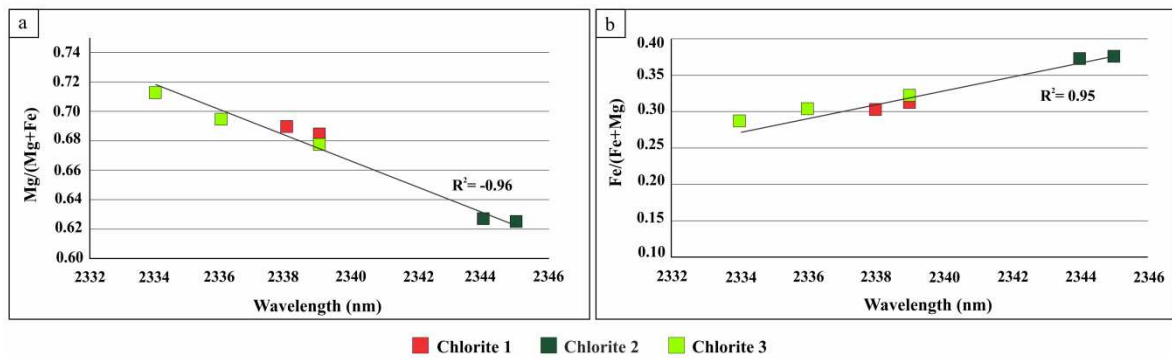


**Figure 49:** a) Correlation between #Mg; b) #Fe<sub>(IV)</sub> contents of chlorites (from EPMA data, for 140 atoms) and position of 2340 nm absorption feature.

### 7.3. Chlorite crystallization temperature and fluid inclusions correlation

The chlorite crystallization temperatures were calculated following the recommendations and equations of Bourdelle *et al.* (2013) and Inoue *et al.* (2009). The temperatures obtained for each group were: (i) Chlorite 1, generated from the alteration of the biotite from the phyllonite, with minimum temperature of 377 °C and maximum of 433 °C, with a geometric average of 396 °C; (ii) chlorite 2, related to the propylitic alteration, with minimum and maximum temperatures of 247 and 389 °C respectively, with a geometric mean of 389 °C; (iii) chlorite 3, associated with the chloritization, with minimum temperatures of 298 °C and maximum of 382 °C, with a geometric median of 334 °C. In contrast with previous fluids inclusions thermometric studies from Assis (2006) and Silva and Abram (2008), it is observed that aqueous inclusions and mixed H<sub>2</sub>O–CO<sub>2</sub> inclusions have broadly similar homogenization temperatures to the chlorite of groups II and III. However, group 1 presents higher temperatures, suggesting a previous stage of greater temperatures within the system. Additionally, the temperatures obtained for groups 1 and 3 are in accordance with Silva and Abram (2008) and Trevisan (2015), who estimated maximum and minimum

temperatures between 209 and 340 °C, and 314 and 332 °C respectively, from chlorite crystals adjacent to the principal mineralized veins from the Paraíba deposit.

#### 7.4. White mica, chlorite and biotite comparison

Table 6 resumed the principal characteristics of the five white mica groups identified in the Paraíba deposit. It shows that the chemical classification varies from muscovite to phengite according to different authors; pervasive to fissural hydrothermal alteration styles and grain sizes varying between 05 and 1000 µm according to white mica type and origin.

It is observed that the highest Al values are related to White Mica 1, evidencing a minor Si + [Fe + Mg] exchange, and White Mica 3 and 5 present lower Al values but are Fe-rich and Mg-poor. White Mica 2 and 4, associated with ore zones, present the lowest Al contents and are Mg-rich and Fe-poor. Such compositional variations are evidenced by wavelengths changes at 2200 Al-OH absorption, the higher the Al contents, the shorter the wavelength.

White Mica Characteristics	● White Mica 1	● White Mica 2	● White Mica 3	● White Mica 4	● White Mica 5
<b>Tappert (2013)</b>	Phengite	Phengite/Mg phengite	Phengite	Mg phengite	Phengite
<b>Velde (1985)</b>	Muscovite	Phengite	Muscovite	Phengite	Muscovite
<b>Guidottti (1987)</b>	Muscovite	Phengite	Muscovite/Fe-Muscovite	Phengite	Muscovite/Fe-Muscovite
<b>Alteration Style</b>	Pervasive	Selective pervasive	Pervasive	Fissural	Fissural
<b>Grain Size (µm)</b>	05-80	50-200	200-1000	50-150	20-100
<b>Stage</b>	Pre-ore stage 1	Post-ore stage 1	Pre-ore stage 2	Ore - stage 2	Post-ore stage 2
<b>Al<sub>(t)</sub></b>	2.45	2.32	2.39	2.35	2.38
<b>Fe<sub>(t)</sub></b>	0.19	0.15	0.23	0.15	0.24
<b>Si</b>	3.19	3.25	3.16	3.21	3.14
<b>Mg</b>	0.18	0.31	0.21	0.31	0.27
<b>Absorption Feature (nm)</b>	2198-2207	2210-2225	2207-2215	2213-2221	2212-2214

**Table 6:** Main attributes identified for white mica groups.

The Table 7 summarizes the three chlorite groups defined at Paraíba deposit. It shows the chlorite classification according to different authors nomenclature, basing on its #Fe and Si content and the  $Al^{IV}/(Si + Al^{VI})$  ratio. Different alteration styles, from selective to pervasive and grain sizes varying from 120 to 1000 µm, are also shown. Compositionally, Chlorite 1 and 3 present similar Fe and Mg contents, while chlorite 2 is Fe-rich and Mg-poor.

Regarding the crystallization temperatures, the highest values are represented by Chlorite 1, due to its relationship with the phyllonite formation, whereas Chlorite 2 shows the

lowest and most varied temperatures, evidencing a peak and the subsequent decrease of the propylitic alteration isotherms. The chlorite 3 represents an alteration related to low-temperature processes, associated to an evolved system.

Chlorite group Characteristics	● Chlorite 1	● Chlorite 2	● Chlorite 3
Foster (1962)	Brunsygite/Ripidolite	Brunsygite/Ripidolite/Diabanite	Brunsygite/Diabanite
Ciesielczuk (2012)	Chamosite Fe-Al	Clinochlore Fe/Chamosite Fe-Al	Clinochlore Fe/Chamosite Fe-Al
Wiewióra and Weiss (1990)	Clinochlore/Diaphinite	Clinochlore/Diaphinite	Clinochlore/Diaphinite
Alteration Style	Selective pervasive	Pervasive	Selective pervasive
Grain Size (µm)	120 - 200	200 - 750	200 - 1000
Stage	Post-ore stage 1	Ore stage 2	Post-ore stage 2
Cristalization Temperature (°C)	396	314	334
Fe <sub>(t)</sub>	1.42	1.72	1.43
Mg	3.16	2.87	3.32
Si	2.77	2.84	2.94
Absorption Feature (nm)	2337	2345	2335

**Table 7:** Main attributes identified for chlorite groups.

The principal chemical characteristics between igneous and hydrothermal biotite are shown in Table 8. The table shows a chemical classification according to its Al<sup>IV</sup>, #Fe, Mg contents and grain sizes classification.

Biotite sample Characteristics	● BH020-019	● BH020-027	● BH041-016	● BH059-041	● BH059-046	● BH041-003
Bt type	Hydrothermal	Hydrothermal	Hydrothermal	Hydrothermal	Hydrothermal	Igneous
Tamizel (2014)	Phlogopite	Phlogopite	Phlogopite	Phlogopite	Phlogopite	Biotite
Foster (1962)	Phlogopite/Mg-Biotite	Phlogopite/Mg-Biotite	Phlogopite	Phlogopite/Mg-Biotite	Phlogopite/Mg-Biotite	Mg-Biotite
Nachit <i>et al.</i> (2005)	Secondary Biotite	Re-equilibrated primary Biotite	Secondary Biotite	Secondary Biotite	Secondary Biotite	Re-equilibrated primary Biotite
Grain Size (µm)	40 - 100	100 - 200	80 - 300	100 - 150	40	400 - 1500
Depth from surface (m)	95	145	325	272	340	70
Fe <sub>(t)</sub>	0.79	0.81	0.40	0.67	0.82	1.00
Mg	1.86	1.74	2.37	2.11	1.90	1.48
Ti	0.02	0.06	0.01	0.01	0.01	0.13

**Table 8:** Main attributes identified for biotite groups.

The relationship between Mg content and depth (from actual surface) shows higher Mg values at greater depth, evidenced by an increase in the phlogopite crystals abundance. Such vertical zonation can be related to (i) an increase in temperature with an increase in depth (Guidotti *et al.* 1988); (ii) the presence of a mafic unit in depth, (iii) P and T increment, associated with the shear zone, (iv) compositional changes of the hydrothermal-

metamorphic fluid, (vi) vertical zonation caused by the intrusion of the porphyritic syenogranite unit (Fig. 50).

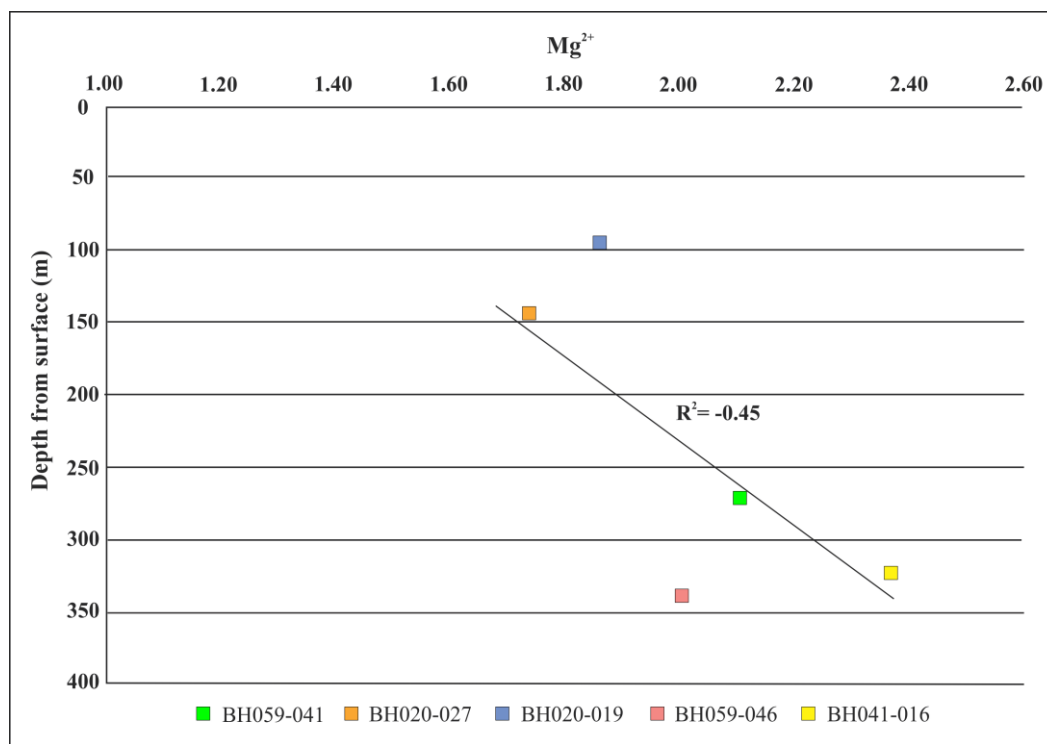


**Figure 50:** Relationship between the biotite Mg contents and its variation with respect to depth from the actual surface.

## 7.5. Timing and mineral evolution

Orogenic belts are extremely complex regions, in which Au deposits can be generated or modified along its evolution story. These regions commonly host different types of auriferous deposits which can be superposed generating controversies about its origin (Groves *et al.* 2003). The orogenic Au deposits are developed in areas with moderate to high-T and low to moderate P metamorphism (Powell *et al.* 1991), with consequent generation of large volumes of granitic melts. Therefore, a spatial relationship with certain intrusions is also expected for these deposits and there is a possibility of a genetic connection (Groves *et al.* 2003).

The principal characteristics of orogenic Au deposits around the world were studied by numerous authors (Groves *et al.* 1998, Goldfarb *et al.* 2001, Groves *et al.* 2003). Some deposit examples are Mount York, Bamboo, Zolotaya and Blue Spec in Pilbara craton; Golden Mile, Norseman, and Jundee in Yilgarn craton; Morro Velho, Raposos and Santana in

the greenstone belt of Rio das Velhas in São Francisco craton, Brazil; among many others. The orogenic auriferous deposits are characterized by: (i) late Archean (2.8 to 2.55 Ga) and Paleoproterozoic (2.1-1.8) ages, related to thermal events associated with the growth of new continental crust; (ii) an origin related to the last phase of the deformational-magmatic-metamorphic history of the orogen (Groves *et al.* 2000); (iii) host rocks with regional metamorphism in greenschist and low amphibolite facies; (iv) ore is developed syn-kinematically with, at least, one stage of the main penetrative deformation of the country rock; (v) strong structural control involving shear zones, generally located in sub-vertical faults; (vi) vertical dimensions up to 1 – 2 km; (vii) lateral zonation, characterized by a strong alteration of the host rock, and, due to the temperature variations, the proximal wall-rock alteration assemblages typically vary from sericite-carbonate-pyrite, to biotite-amphibolite-pyrrhotite and biotite/phlogopite at deeper crustal levels (Ridley *et al.* 2000); (viii) mineral assemblage characterized by quartz, carbonate, mica, albite, chlorite, epidote and pyrite; (ix) Au associated with Ag  $\pm$  As  $\pm$  B  $\pm$  Bi  $\pm$  Te, although it can be associated with lesser quantities of Cu, Mo, Pb, Sn y Zn; (x) low S contents (<5%); (xi) low salinity fluids, close to neutral, H<sub>2</sub>O-CO<sub>2</sub>  $\pm$  CH<sub>4</sub>  $\pm$  N<sub>2</sub>; (xii) generally associated with mafic to ultramafic intrusions; and (xiii) relatively high contents of arsenopyrite.

On the other hand, other authors suggested that some Au deposit, located in metamorphic belts with similar characteristics to orogenic deposits, but with a spatial and temporal relationship with granitic intrusions, might be named as ‘intrusion-related’ (Sillitoe 1991, Sillitoe and Thompson 1998, Thompson and Newberry 2000, Lang *et al.* 2000). With the aim to separate these two types of deposits, Lang *et al.* (2000) synthesized the principal characteristics of the intrusion-related gold deposit, using the studies previously made by Sillitoe (1991) and Newberry *et al.* (1995), among others. These characteristics are: (1) metaluminous, subalkaline intrusions of intermediate to felsic composition; (2) high salinity and low-CO<sub>2</sub>-bearing hydrothermal fluids, although the coexistence of aqueous bi-phase and aquo-carbonatic fluid inclusions is possible; (3) a metal assemblage that variably includes Au with anomalous base-metal concentrations; (4) comparatively restricted zones of hydrothermal alterations within granitoids; (5) a continental tectonic setting well inboard of inferred or recognized convergent plate boundaries; (6) a location in magmatic provinces best known for W and/or Sn deposits; and (7) restricted hydrothermal system. Besides these characteristics, another criterion can be used to differentiate the two deposit types: timing of the mineralization, if the deposit is structurally-controlled. In Au orogenic deposits, the

mineralization is synchronous with the penetrative structures (ductile) development, while in intrusion-related deposits it is late respect to the deformation.

A checklist, based on Groves *et al.* 2003, with the principal characteristics of the Paraíba deposit, was made (Table 9). This analysis used information obtained in this thesis and other taken from previous works from Abreu Filho *et al.* (1992), Paes de Barros (1994), Siqueira (1997), Souza *et al.* (2005), Moreton and Martins (2005), Assis (2006), Paes de Barros (2007), Silva and Abram (2008), Trevisan (2015) and Bartolomeu (2016). Summarising the obtained data, the Paraíba deposit presents the following characteristics:

- (i) Paleoproterozoic age. Paraíba tonalite dated at  $2.014 \text{ Ga} \pm 5.1 \text{ Ma}$  (U-Pb) by Trevisan (2015) and the Au-rich quartz vein at  $1.841 \text{ Ga} \pm 22 \text{ Ma}$  (Ar-Ar) by Santos (2011).
- (ii) Located in a magmatic arc region.
- (iii) Spatially associated with a syenogranite porphyritic intrusion (Syenogranite age have not published yet).
- (iv) Presents lenticulars and branched sulphides-gold-rich quartz veins with approximately 1,500 m in length and 0.3 - 1.5 m thickness emplaced in a shear zone, and also brecciated zones and diverse hydrothermal alterations.
- (v) Overlapping events, evidenced by the syenogranite porphyry intrusion cross-cutting the Au-rich veins, while the magmatic-hydrothermal alterations are not affected by younger alterations.
- (vi) The Au-rich quartz veins can be late to syntectonic (greenschist to low amphibolite facies), possibly emplaced in brittle-ductile regime, whereas the magmatic-hydrothermal alterations and disseminated and venular Cu-Mo mineralization might be post-tectonic.
- (vii) Principal quartz veins with a metal association of  $\text{Au} \pm \text{Cu}$  ( $\text{Bi} \pm \text{Te} \pm \text{Mo} \pm \text{Ag}$ ), and the disseminated and late veins mineralization with a metal association of  $\text{Cu} + \text{Mo} \pm \text{Zn} \pm \text{Pb}$ .
- (viii) Absence of arsenopyrite.
- (ix) Sulphur content  $>5\%$ .
- (x) The metamorphic-hydrothermal alteration halo, which occurs close to the auriferous veins, is composed of biotite and phlogopite, white mica, carbonate, and pyrite. The syenogranite is related to potassic, sericitic, propylitic, epidotization and chloritization alteration halos.
- (xi) Greenschist to low amphibolite metamorphic grade.
- (xii) Fluid inclusion of variable composition and salinity (Assis 2006, Paes de Barros 2007, Silva and Abram 2008 and Trevisan 2015). The coexistence of fluids rich in  $\text{CO}_2$  and low salinity with aqueous fluid with high salinity suggests a magmatic or metamorphic system as a source of those fluids (Assis 2006, Paes de Barros 2007, Silva and Abram 2008). Regarding

temperature conditions, these authors obtained maximum temperatures of 360 °C, approximately. In this thesis, the obtained temperatures were 396, 314 and 334 °C for Chlorite 1, 2 and 3 respectively.

Critical characteristics	Orogenic gold deposits	Intrusion-related gold deposits
Age range	✓ Middle Archean to Tertiary; peaks in Late Archean, Paleoproterozoic and Phanerozoic	Mainly Phanerozoic, some Proterozoic; rare Late Archean ✓
Tectonic setting	✓ Deformed continental margin mainly of allochthonous terranes	Pericratonic terranes of the miogecline margin ✓
Structural setting	✓ Commonly structural highs during later stages of compression and transtension	Compressional to extensional transition in fold and thrust belts ✓
Host rocks	✓ Variable, mainly mafic volcanic or intrusive rocks or geywacke-slate	Major examples in granitoid intrusions; some in sedimentary rocks ✓
Metamorphic grade of host rocks	✓ Mainly greenschist facies to amphibolite	Mainly subgreenschist to greenschist facies ✓
Association with intrusions	❓ Commonly felsic to lamprophyre dikes or continental margin batholiths	Strong association with granitoid stock; lamprophyre dikes ✓
Mineralization style	✓ Variable, large veins, veins array, saddle reefs, replacement of Fe-rich rocks	Commonly sheeted veins, lesser breccias, veins, and disseminations ✓
Timing of mineralization	✓ Late-tectonic; post-(greenschist) to syn-(amphibolite) metamorphic peak	Very late tectonic; postregional metamorphic peak ❓
Structural complexity of ore bodies	✓ Complexity common, particularly in brittle-ductile regimes	Mainly simple vein arrays in relatively brittle regimes ✓
Evidence of overprinting	✓ Strong overprinting in larger deposits; multiple veining events	Minor evidence of overprinting by late structures ✓
Metal association	✗ Au-Ag ± As ± B ± Bi ± Sb ± Te ± W	Au-Ag ± As ± B ± Bi ± Sb ± Te ± W (Pb-Zn distal) ✗
Metal zoning	✗ Small lateral zonation in comparison with vertical extent	Strong district-scale zoning Au-W/Sn-Ag/Pb/Zn ✗
Proximal alteration	✓ Varies with metamorphic grades, normally mica-carbonate-Fe sulfide	Mica-K, feldspar, carbonate, chlorite, Fe-sulfide ✓
P-T Conditions	✓ 0.5-4.5 kbar, 220°-600°C Normally 1.5 ± 0.5 kbars, 350° ± 50°C	0.5-1.5 kbar, 200°-400°C for Au-rich systems ✓
Ore fluids	✗ Low-salinity H <sub>2</sub> O-CO <sub>2</sub> ± CH <sub>4</sub> ± N <sub>2</sub>	Variable-salinity H <sub>2</sub> O-CO <sub>2</sub> , very minor CH <sub>4</sub> ± N <sub>2</sub> ✗
Proposed heat sources	❓ Varied; asthenosphere upwelling to midcrust granitoids	High-level granitoid in gold district ✓
Proposed metal sources	✓ Subducted/subcreted crust and/or supracrustal rocks and/or deep granitoids	High-level granitoids and/or supracrustal rocks ✓

**Table 9:** Comparison of orogenic gold and intrusion-related gold deposits in terms of their critical regional-to deposit-scale characteristics and its relationship with the Paraíba deposit features. Concordant features are marked with a green tick, partially concordant with an orange tick, no-

concordant with a red tick, and features for which there is no update information with a blue interrogation symbol. (Modified from Groves *et al.* 2003).

(xiii) Pressure conditions estimated by Assis (2006) from 1.0 to 3.6 Kbar, proposing a formation depth of 3-10.8 km for the Paraíba deposit.

(xiv) The heat and metal source of the Paraíba deposit is still questionable.

Despite having a large amount of data and studies conducted over the years, this work does not allow us to conclude that the Paraíba deposit is related to a specific deposit type. Nevertheless, a possible metamorphic-hydrothermal origin is suggested for the auriferous quartz veins, whereas for the disseminated Cu and Mo mineralization is proposed a magmatic-hydrothermal origin, possibly associated with the syenogranite porphyry intrusion. Taking this into account, it is proposed a possible evolutionary story of the Paraíba deposit that can be summarized in 6 main stages (Fig. 51).

**Stage 1:** In a first stage, the gneiss basement, dated from  $2,816 \pm 4$  (U-Pb) to  $1.98 \pm 8.8$  Ma (U-Pb) by Souza *et al.* (2005), Paes de Barros (2007) and Assis (2015), is intruded by the tonalite dated by Trevisan (2015) in  $2.014 \pm 5.1$  (U-Pb).

**Stage 2:** This stage characterizes the beginning of the deformational phase, which evolves towards a dextral shear zone and a subsequent phyllonite formation. The shear zone formation causes the feldspar destabilization, mainly represented by plagioclase, and the consequent White Mica 1 formation, being more evident at higher strain zones.

**Stage 3:** With the increase of deformational tension, grain size reduction takes place. A critical rise in hydrostatic pressure within the grains triggers the destabilization of the primary crystals, and consequent phyllosilicate neoformation, represented exclusively by Mg-rich biotite and phlogopite crystals and the development of a strong foliation in response to the new metamorphic-hydrothermal conditions. The concentration of biotite and phlogopite presents marked vertical zoning, evidenced by the increase in Mg concentrations at greater depths. Using this foliated zone, the intrusion of successive Si-sulphides-rich fluid pulses generated the Au  $\pm$  Cu (Bi  $\pm$  Te  $\pm$  Mo  $\pm$  Ag) rich veins, related to the "ore stage 1".

**Stage 4:** After the deformation stops, the intrusion of the basic units takes place. They are represented by centimetric to metric mafic dykes and a gabbroic composition dyke of 40 m width. No field evidence has been found showing these units cut by the principal veins, and neither of them show evidence of deformation.

**Stage 5:** Once the deformational phase and the mafic units intrusion conclude, the emplacement of a mineralized Cu-Mo porphyritic syenogranite unit takes part. As a

consequence, according to depth and distance respect to the intrusive body, different hydrothermal alterations are generated: (i) a calcic alteration area with a fissural style and spatially restricted, assuming that the source of this alteration is in depth; (ii) a potassic alteration, represented by a Bt-Mgt-rich zone and (iii) another potassic alteration, evidenced by large amounts of microcline.

**Stage 6:** Cutting all the lithologies and the previous alterations discordantly, a sericitic alteration takes place. It is represented by quartz veins associated with white mica ("White mica 4"), chalcopyrite, pyrite and molybdenite. In the following phase, a pervasive propylitic alteration occurs, characterized by the typical pistachio colour and a mineral assemblage of chlorite + epidote + calcite as well as disseminated pyrite and chalcopyrite.

Subsequently and overlapping the propylitic alteration, a strong increase in epidote crystallization is observed, mainly in a fissural style, drawing on weakness areas previously generated, as phyllonite foliation for example (Fig. 24). This alteration is responsible for the hydrothermal breccia generation, being part of the matrix (Figs. 18f and 23). The epidotization is strongly related to significant amounts of disseminated chalcopyrite and molybdenite, as well as smaller proportions of pyrite, and form with the sericitic alteration the "ore stage 2".

Finally, an alteration related to low-temperature processes, associated with an evolved system takes place. It is characterized by an intense and pervasive chloritization, which affect phyllosilicates, as phyllonite-rich zones. Besides, this alteration is associated, temporally, with centimetric to millimetric barren muscovite + quartz, calcite, calcite + quartz, and fluorite + quartz veins and veinlets.

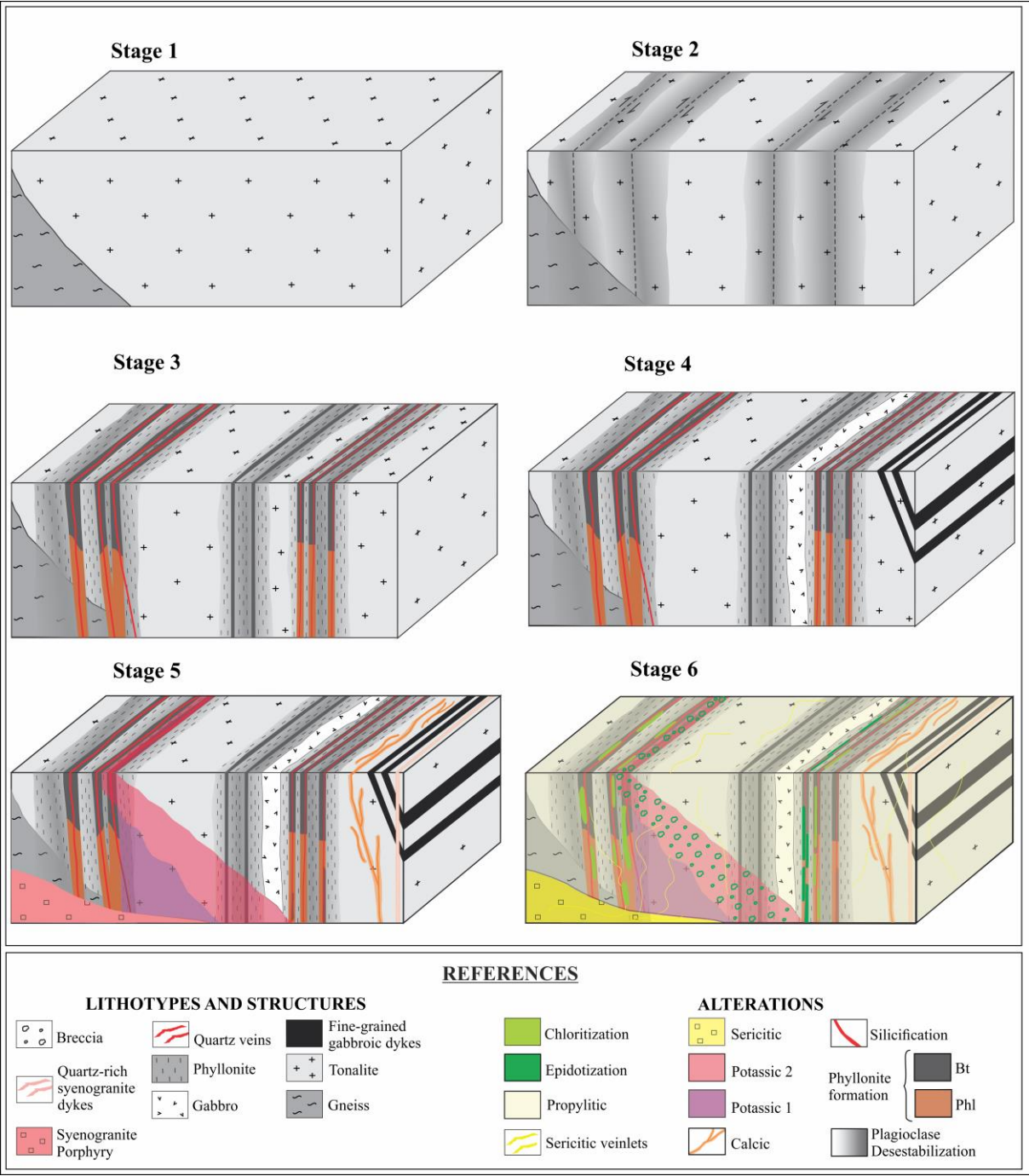


**Figure 51:** Proposed evolutionary history of the Parafba deposit summarized in 6 main stages.

## 8. CONCLUSIONS

---

The Paraíba deposit is formed by two different mineralization processes, named in this work as ore stage 1 and ore stage 2. The first one, with a possible metamorphic-hydrothermal origin, is related to Au-rich quartz veins and located in a ductile environment in a dextral shear zone. The shear zone evolution leads to the generation of white micas and, subsequently, to the phyllonite formation, represented by a mineral assemblage given by biotite, phlogopite and carbonate. The second event, associated with a magmatic-hydrothermal stage, is related to a porphyritic syenogranite unit intrusion and the subsequent generation of several hydrothermal alteration zones, hydrothermal breccia and Cu and Mo mineralizations.

The spectral analysis, integrated with field geological description, petrography and mineral chemistry, allows the identification of the following minerals groups: (i) five groups of white mica, called here as White Mica 1, 2, 3, 4 and 5; (ii) three chlorite groups, called here as Chlorite 1, 2 and 3; (iii) epidote with different compositions; and (iv) biotite with different compositions and vertical Mg-contents zonation. These white mica, chlorite and epidote have different compositions and crystallinity degrees. This variation could be attributed to physico-chemical parameters occurring during the hydrothermal alteration processes, possibly including pH, composition of hydrothermal fluids, water/rock ratios, and temperature.

The spectral studies showed that the five white mica groups have the following compositions: normal potassic for White Mica 1 (2198-2207 nm), tending to phengite for White Mica 2 (2210-2225 nm), tending to phengite for White Mica 3 (2207-2215 nm), tending to phengite to phengite for White Mica 4 (2213-2221 nm), and tending to phengite for White Mica 5 (2212-2214 nm). The differentiation among them was only possible from the integration with other conventional methods. However, the combined use of the composition, abundance and crystallinity spectral parameters for white mica represent a very strong proxy to mineralized zones. The importance resides in that the Au-Cu-Mo mineralization is associated with Al-poor and Mg-rich white micas with tending-to-phengite to phengite composition (wavelengths from 2210 to 2225 nm), higher abundance, and higher crystallinity index ( $CI > 4$ ). In this sense, the White Mica 2 and White Mica 4 are directly related to Au and Cu-Mo mineralization, respectively, whereas the Al- and Fe-rich White Mica 1, 3 and 5 do not present relationship with ore zones.

Chlorite groups 1 and 3, with a Mg-rich composition (Mg-OH absorption between 2225 and 2240 nm), are related to chloritization of phyllonite. On the other hand, chlorite 2, with a Fe-rich composition (Mg-OH absorption between 2340 and 2347.5 nm), are associated to propylitic alteration. The spatial relationship between epidotized zones and high Cu contents was established using spectral data. Besides, these data show compositions from epidote to tending to clinozoisite. However, it was not possible to correlate a specific composition with the highest Cu contents.

The reflectance spectroscopy allowed determined a phyllonite vertical zonation, where the Mg content in biotite increases in depth. This fact is evidenced by large amounts of phlogopite at deeper deposit levels. The causes of this increase in Mg concentration have not yet been clarified. More studies should be carried out to determine its genetic implications and if they are related to Au-rich levels or not.

The application of punctual and imaging spectral techniques helped in the mineralogical classification of different hydrothermal alteration zones and definition of mineral vectoring tools for exploration at the Paraíba deposit. These data, integrated with field and petrographic descriptions, permitted the creation of lithologic and hydrothermal alteration sections and the determination of the system hydrothermal evolution. This study demonstrates the importance of combining spectral analysis to conventional techniques for the study of hydrothermal alteration systems within old and complex terrains, such as those found in Alta Floresta Mineral Province.

## 9. REFERENCES

---

- Abreu-Filho W., Paes de Barros A.J., Barreto-Filho J.A., 1992. Projeto ouro gemas. Relatório anual da área piloto da reserva garimpeira de Peixoto de Azevedo. Relatório anual DNPM, CPRM, Cuiabá, 31p.
- Almeida F.F.M. 1978. Tectonic map of South América, 1:5.000.000 - Explanatory note. Brasília: DNPM, 1978. 23 p. Trabalho elaborado em parceria com CGMW e UNESCO.
- Almeneida F.F.M, Hasui Y., Brito Neves B.B. 1976. The upper Precambrian of South American, Boletim IGC-USP, 7:45-80.
- Assis R.R. 2015. Depósitos auríferos associados ao magmatismo félsico da Província de Alta Floresta (MT), Cráton Amazônico: idade das mineralizações, geoquímica e fonte dos fluidos. Tese de Doutorado, Instituto de Geociências, Universidade Estadual de Campinas, 363p.
- Assis R.R. 2011. Depósitos auríferos associados ao magmatismo granítico do setor leste da Província de Alta Floresta (MT), Cráton Amazônico: tipologia das mineralizações, modelos genéticos e implicações prospectivas. Dissertação de Mestrado, Instituto de Geociências, Universidade Estadual de Campinas. Campinas, Brasil, 373 p.
- Assis R.R. 2008. Contexto geológico e associação paragenética das mineralizações auríferas de União do Norte, região de Peixoto de Azevedo, Província de Alta Floresta (MT). Trabalho de Conclusão de Curso, Instituto de Geociências, Universidade Estadual de Campinas, 81p.
- Assis R.R. 2006. Estudo de inclusões fluidas nos depósitos auríferos de Novo Mundo e Santa Helena na região de Teles Pires - Peixoto de Azevedo (Mato Grosso), Província de Alta Floresta. Instituto de Geociências, Universidade Estadual de Campinas; Relatório PIBIC/ CNPq; 18p.
- Assis R.R., Xavier R.P., Paes de Barros A. J., Barbuena D., Trevisan V.G., Ramos G. S., Teixeira R.V., Miguel-Jr E., Rodrigues R. M., Stabile-Jr A., dos Santos T. J. S., Miranda G. M. T., Barros M. A., Pinho F. E. C. 2014. Depósitos de Au e Au+metais base associados a sistemas graníticos Paleoproterozóicos do setor leste da Província Aurífera de Alta Floresta (MT), Cráton Amazônico. In: Jort H. and Silva M.G. (eds.).

Metalogenia das Províncias Tectônicas Brasileiras: Província de Alta Floresta. Serviço Geológico do Brasil, CPRM.

- Assis, R., Xavier R., Paes de Barros J.A., Rodrigues M.R., Teixeira R., Trevisan V., Ramos G., Miguel Jr E. 2012. Gold copper and gold + base metal deposits associated with granitic systems from the eastern sector of the Alta Floresta Gold Province (MT), Amazon Craton.
- Bartolomeu J.O. 2016. Sistemas Au-(Cu) Associados a Intrusões de Pórfiros na Província Aurífera de Alta Floresta, Sul do Cráton Amazônico: O Caso do Depósito Paraíba. Trabalho de Conclusão de Curso, Instituto de Geociências, Universidade Estadual de Campinas. 63p.
- Bierwirth P., Huston D., Blewett, R. 2002. Hyperspectral Mapping of Mineral Assemblages Associated with Gold Mineralization in the Central Pilbara, Western Australia. *Economic Geology*, 97(4), 819–826.doi:10.2113/gsecongeo.97.4.819
- Bishop J.L., Lane M.D., Dyar M.D., Brown A.J. 2008. Reflectance and emission spectroscopy study of four groups of phyllosilicates: smectites, kaolinite-serpentines, chlorites and micas. *Clay Miner.* 43, 35–54.
- Boardman J. W. 1993. Automating spectral unmixing of AVIRIS data using convex geometry concepts (vol. 1). In *Summaries 4th Annual JPL Airborne Geoscience Workshop*, pp. 11–14.
- Boardman J. W., Kruse F. A. 2011. Analysis of imaging spectrometer data using N - dimensional geometry and a mixture-tuned matched filtering approach. *IEEE Transactions on Geoscience and Remote Sensing*, 49(11), 4138– 4152.
- Boardman J. W., Kruse F. A., Green, R. O. 1995. Mapping target signatures via partial unmixing of AVIRIS data. In *Summaries of the Fifth Annual JPL Airborne Earth Science Workshop. 1: AVIRIS Workshop* (pp. 23–26).
- Bourdelle F., Parra T., Chopin C., Beyssac O. 2013. A new chlorite geothermometer for diagenetic to low-grade metamorphic conditions. *Contrib Mineral Petrol*, 165:723–735

- Chmielowski R.M., Jansson N., Fjellerad Persson M., Fagerström P. 2016, 3D modelling of hydrothermal alteration associated with VHMS deposits in the Kristineberg area, Skellefte district, northern Sweden: *Mineralium Deposita*, v. 51, p. 113–130.
- Ciesielczuk J. 2012. Chlorite of hydrothermal origin in the Strzelin and Borów granites (Fore-Sudetic Block, Poland). *Geological Quarterly*, 56(2): 333-344.
- Clark R. N. 1999. *Spectroscopy of Rocks and Minerals, and Principles of Spectroscopy*. Geological Survey Denver, Colorado. *Remote Sensing for the Earth Sciences: Manual of Remote Sensing*, 3 ed., Vol. 3, chapter 1.
- Clark R.N., Swayze G.A., Wise R., Livo E., Hoefen T., Kokaly R., Sutley S.J. 2007. USGS digital spectral library. In: U.S. Geological Survey, *Digital Data Series*, 231 pp.
- Clark R.N., Swayze G.A., Gallagher A., King T.V.V., Calvin W.M., 1993. The USGS Geological Survey Digital Spectral Library: Version 1: 0.2 to 3.0  $\mu\text{m}$  [EUA]: U.S. Geological Survey. *Open File Report*, 592.
- Clark R.N., King T.V.V., Klejwa M., Sways, G.A. 1990. High spectral resolution reflectance spectroscopy of minerals. *J. Geophys. Res.* 95, 12,653-12,680.
- Clark R.N., Roush T.L. 1984. Reflectance spectroscopy: quantitative analysis techniques for remote sensing applications. *J. Geophys. Res. Solid Earth* 89, 6329–6340.
- Cooke D R, Agnew P, Hollings P. 2017. Porphyry indicator minerals (PIMS) and porphyry vectoring and fertility tools (PVFTS)-indicators of mineralization styles and recorders of hypogene geochemical dispersion halos. In: *Exploration 17: Sixth Decennial International Conference on Mineral Exploration*. Toronto Division of Exploration and Mining, Sydney, Australia.
- Corbett G.J., Leach T.M. 1997. Southwest Pacific gold-copper systems: Structure, alteration and mineralization. *Special publication 6*, Society of Economic Geologists, 238p.
- Cordani U.G., Teixeira W. 2007. Proterozoic accretionary belts in the Amazonian Craton. In: Hatcher, R.D., Jr., Carlson, M.P., McBride, J.H., and Martínez-Catalán, J.R. (eds.), 4-D,

Framework of Continental Crust: Geological Society of America Memoir 2000, 297-320.

Cordani U.G., Teixeira W., Tassinari C.C.G., Kawashita K., Sato K. 1988. The growth of the Brazilian Shield. *Episodes*, 11:163-167.

Cudahy T., Jones M., Thomas M., Cocks P., Agustin F., Caccetta M., Hewson R., Verrall M., Rodger A. 2010. Mapping soil surface mineralogy at Tick Hill northwestern Queensland, Australia, using airborne hyperspectral imagery. In: Viscarra Rossel, R.A., McBratney A.B., and Minansy B., (eds.), *proximal soil sensing*: Berlin, Springer, p. 211-229.

Cudahy T., Jones M., Thomas M., Laukamp C., Caccetta M., Hewson R., Rodger A., Verrall M., 2008. Next Generation Mineral Mapping: Queensland Airborne HyMap and Satellite ASTER Surveys 2006–2008. Perth, publicly Available Report P2007/ 364. CSIRO Exploration and Mining (<http://c3dmm.csiro.au/NGMM/>, 152 p.).

Deer W.A., Howie R.A., Zussman J. 1992. *An introduction to rock-forming minerals*. 2nd Ed., Essex. Longman Scientific & Technical. 696p.

Doublier M.P., Roache A., Potel S. 2010. Application of SWIR spectroscopy in very low-grade metamorphic environments: a comparison with XRD methods: *Geol. Sur. Western Aus.*, 61p.

Ducart D.F. 2007. Alteração hidrotermal do prospecto aurífero cerro La Mina, Los Menucos, Patagonia Argentina: Geologia, sensoriamento remoto e isótopos estáveis. Tese de doutorado. 187p. Biblioteca IG-UNICAMP.

Ducart D.F and Stolf M. 2018. Secagem de amostras para estudos espectrais semi-quantitativos aplicados na exploração mineral. 49º Congresso Brasileiro de Geologia. Rio de Janeiro, 2018.

Ducart D. F., Silva A. M., Toledo, C. L. B., Assis L. M. 2016. Mapping iron oxides with Landsat-8/OLI and EO-1/Hyperion imagery from the Serra Norte iron deposits in the Carajás Mineral Province, Brazil. *Brazilian Journal of Geology*, 46(3), 331–349.

- Ducart D.F., Silva A., Bemfica Toledo C.L., Prado E. 2015. Caracterização espectral quantitativa do minério de ferro na Mina N4, Província Mineral de Carajás, a partir de imagens Landsat 8 e Hyperion. In: XVII Simpósio Brasileiro de Sensoriamento Remoto - SBSR, At João Pessoa-PB, Brasil, Volume: Anais.
- Duke E.F. 1994. Near infrared spectra of muscovite, Tschermak substitution, and metamorphic reaction progress: Implications for remote sensing: *Geology*, v.22, p 621-624.
- Farmer V. C. 1974. *The Infrared Spectra of Minerals*. Mineralogical Society, London
- Economic Geology (2017) 112 (5): 1153-1176.
- Foster M. D. 1962. Interpretation of the composition and a classification of the chlorites: U.S. Geological Survey Professional Paper 414-A, 33 pp.
- Gaffey S. J., McFadden L. A., Nash D., Pieters C. M. 1993. Ultraviolet, visible, and near-infrared reflectance spectroscopy: Laboratory spectra of geologic materials. In *Remote Geochemical Analysis Elemental and Mineralogical Composition*, 43-73.
- Goldfarb R.J., Groves D.I., Gardoll, S., 2001, Orogenic gold and geologic time: A global synthesis. *Ore Geology Reviews*, v. 18, p. 1–75.
- Green A.A., Berman M., Switzer P., Craig M.D. 1988. A transformation for ordering multispectral data in terms of image quality with implications for noise removal. *Geosci. Remote Sens. IEEE Trans.* 26, 65–74.
- Groves D.I., Goldfarb R.J., Robert F., Hart C.J.R. 2003. Gold deposits in metamorphic belts: overview of current understanding, outstanding problems, future research, and exploration significance. *Economic Geology*, 98, 1–29.
- Groves D.I., Goldfarb R.J., Knox-Robinson C.M., Ojala J., Gardoll S., Yun G., Holyland P. 2000. Late-kinematic timing of orogenic golddeposits and significance for computer-based exploration techniques with emphasis on the Yilgarn block, Western Australia. *Ore Geology Reviews*, v. 17, p. 1–38.

- Groves D.I., Goldfarb R.J., Gebre-Mariam M., Hagemann S.G., Robert F. 1998. Orogenic gold deposits: A proposed classification in the context of their crustal distribution and relationships to other deposit types. *Ore Geology Reviews*, 13: 7-27.
- Guidotti C.V., Cheney J., Henry D.J. 1988. Compositional variation of biotite as a function of metamorphic reactions and mineral assemblage in the pelitic schists of western Maine. *American Journal of Science* 288:270-292
- Halley S., Dilles J.H., Tosdal R.M. 2015. Footprints: Hydrothermal alteration and geochemical dispersion around porphyry copper deposits. *Society of Economic Geology Newsletter* 100, p. 1–29.
- Hapke B. 1993. *Theory of Reflectance and Emittance Spectroscopy*. Cambridge, 469 pp.
- Hauff P.L., Kruse F.A., Madrid, R.J. 1989. Gold exploration using illite polytypes defined by X-ray diffraction and reflectance spectroscopy: Gold Forum on Technology and Practices. “World Gold 89,” Society for Mining, Metallurgy and Exploration, Littleton, Colorado, Proceedings, p. 76–82.
- Hook S., Abbott E., Grove C., Kahle A., Palluconi F. 1999. Multispectral thermal infrared in geologic studies. In: A. Rencz (Ed.), *Manual of Remote Sensing*, New York, pp 59-110.
- Hunt G.R., 1977. Spectral signatures of particulate minerals in the visible and near infrared. *Geophysics* 42, 501–513.
- Inoue A., Meunier A., Patrier-Mas P., Rigault C., Beaufort D., Vieillard P. 2009. Application of chemical geothermometry to low-temperature trioctahedral chlorites. *Clays and Clay Minerals*, 57: 371–382.
- Jefferies S.P., Holdsworth R.E., Wibberley C.A.J, Shimamoto T., Spiers C.J., Niemeijer A.R., Lloyd G.E. 2006. The nature and importance of phyllonite development in crustal-scale fault cores: an example from the Median Tectonic Line, Japan. *Journal of Structural Geology* 28 (2006) 220–235.
- JICA/MMAJ. 2000. Metal Mining Agency of Japan/ Japan International Cooperation Agency. Report on the Mineral Exploration in the Alta Floresta Area, Brazil, Final Report, Projeto Alta Floresta – MT, Japan, March, 137 pp.

- Juliani C., Carneiro C.C., Carreiro-Araújo S.A., Fernandes C.M.D., Monteiro L.V.S., Crósta A.P. 2013. Estruturação dos arcos magmáticos paleoproterozóicos na porção sul do Cráton Amazônico: implicações geotectônicas e metalogenéticas. In: 13o Simpósio de Geologia da Amazônia, SBG –Núcleo Norte, Belém. (CD-ROM).
- Kartashov P. 2014. Classification diagram for REE-bearing members of the epidote group based on crystallochemical data. In: Workshop on accessory minerals. Univ Warsaw, pp. 19–21. <http://dx.doi.org/10.13140/2.1.4907.0089>.
- Lang J.R., Baker T. 2001. Intrusion-related gold systems: The present level of understanding. *Mineralium Deposita*, 36:477-489.
- Lang J.R., Baker T., Hart C.J.R., Mortensen J.K. 2000. An exploration model for intrusion-related gold systems: Society of Economic Geologists Newsletter, no. 40, p. 1–15.
- Laukamp C., Cudahy T., Cleverly J.S., Oliver N.H.S., Hewson R. 2011, Airborne hyperspectral imaging of hydrothermal alteration zones in granitoids of the Eastern fold belt, Mount Isa inlier, Australia. *Geochemistry: Exploration, Environment, Analysis*, v. 11, p. 3–24.
- Leite J.A.D., Saes G.S. 2003. Geocronologia Pb/Pb de zircões detríticos e análise estratigráfica das coberturas sedimentares proterozóicas do Sudoeste do Cráton Amazônico. *Geologia USP: Série Científica*, v. 3, n. 1, pp. 113-127.
- Madrucci V. 2000. Avaliação dos produtos integrados TM-Landsat, Radarsat e Gamaespectrométricos na caracterização tectônica e mapeamento geológico de área mineralizada em ouro na região de Alta Floresta-MT. Dissertação de Mestrado em Sensoriamento Remoto. INPE.
- Mason P. 2002. MMTG A-List Hyperspectral Data Processing Software. 920C, CSIRO, Division of Exploration and Mining, Sydney, Australia.
- Miguel Jr E. 2011. Controle Estrutural das mineralizações auríferas e idades U-Pb das rochas encaixantes ao longo do Lineamento Peru-Trairão: Província Aurífera de Alta Floresta, Mato Grosso. Dissertação de Mestrado, Universidade Estadual de Campinas, 86p.

- Miller C.F., Stoddard E.F., Bradfish L.J., Dollase W.A. 1981. Composition of plutonic muscovite: genetic implications. *Can. Mineral*, 19, 25-34.
- Moreira I.C. (in preparation). 2018. Petrogênese dos granitoides e rochas ortoderivadas do depósito Paraíba, domínio Peixoto de Azevedo, Província Aurífera de Alta Floresta, Cráton amazonas. Exame de qualificação para Mestrado. Universidade Estadual de Campinas - UNICAMP, 63p.
- Moreton L.C., Martins E.G. 2005. Geologia e Recursos Minerais de Alta Floresta. Vila Guarita. Escala 1:250.000. Brasília, Serviço Geológico do Brasil/CPRM, 68 p.
- Moreton L.C., MARTINS E.G. 2003. Geologia e Recursos Minerais da Folha Vila Guarita. Folha SC.21-Z-B. Estado de Mato Grosso. Escala 1:250.000. Brasília: CPRM.
- Moura M.A. 1998. O Maciço Granítico Matupá e o Depósito de Ouro Serrinha (MT): Petrologia, Alteração Hidrotermal e Metalogenia. Tese de Doutorado, Instituto de Geociências, Universidade de Brasília, 238p.
- Moura M.A., Botelho N.F., Olívio G.R., Kyser T.K. 2006. Granite-related Paleoproterozoic, Serrinha gold deposit, Southern Amazonia, Brazil: hydrothermal alteration, fluid inclusion and stable isotope constraints on genesis and evolution. *Economic Geology*, 101:585-605.
- Nachit H., Ibhi A., Abia E. H., Ohoud B. 2005. Discrimination between Primary Magmatic Biotites, Reequilibrated Biotites and Neoformed Biotites. *Comptes Rendus Geoscience*, Vol. 337, No. 16, 2005, pp. 1415-1420.
- Naleto J.L. 2018. Mapeamento hiperespectral de associações minerais relacionadas ao depósito de ouro de pedra branca, maciço de troia, Ceará.
- Neal L. C., Wilkinson J. J., Mason P. J., Chang, Z. 2018. Spectral characteristics of propylitic alteration minerals as a vectoring tool for porphyry copper deposits. *Journal of Geochemical Exploration*, 184, 179–198.
- Newberry R.J., McCoy D.I., Brew D.A. 1995. Plutonic-hosted gold ores in Alaska: Igneous versus metamorphic origin: *Resource Geology*, Special Issue no. 18, p. 57–100.

- Oliveira J.B. 2016. Sistemas a Au- (Cu) associados a intrusões de pórfiros na província aurífera de alta floresta, sul do cráton amazônico: o caso do depósito paraíba, trabalho de conclusão de curso. 63p. Biblioteca IG-UNICAMP.
- Paes de Barros A.J. 2007. Granitos da região de Peixoto de Azevedo - Novo Mundo e mineralizações auríferas – Província Aurífera Alta Floresta (MT).
- Paes de Barros A.J. 1994. Contribuição a geologia e controle das mineralizações auríferas de Peixoto de Azevedo - MT. Dissertação de Mestrado, Instituto de Geociências, Universidade de São Paulo, 145p.
- Passos, R.V.; Souza Filho, C. R.; Maria Netto, S. Caracterização da Geometria da Zona de Alteração Hidrotermal do Depósito Aurífero de Brumal, Quadrilátero Ferrífero MG. In: XL Congresso Brasileiro de Geologia, Belo Horizonte, 1998, Belo Horizonte. Boletim de Resumos, XL Congresso Brasileiro de Geologia, 1998. v. 1. p. 124-124.
- Phillips, G.N., Powell R. 2015. Hydrothermal alteration in the Witwatersrand goldfields: Ore Geology Reviews, v. 65, p. 245–273.
- Pimentel M.M. 2001. Resultados geocronológicos do Projeto Promin Alta Floresta. Brasília: UnB. Relatório Interno.
- Pinho M.A.S.B., Chemale-Jr F., Van Schumus W.R., Pinho F.E.C. 2003. U-Pb and Sm-Nd evidence for 1.76-1.77 Ga magmatism in the Moriru region, Mato Grosso, Brazil: implications for province boundaries in the SW Amazon Craton. Precambrian Research, 126(1) 1-25.
- Pontual S., Merry, N.J., Gamson P., 2008. GMEX - Spectral analysis guides for mineral exploration: spectral interpretation field manual. AusSpec International Ltd. 1, p. 188.
- Pontual S., Merry N., Gamson P. 1997. Spectral Interpretation Field Manual, Spectral Analysis Guide for Mineral Exploration, G-MEX Vol 1, AusSpec International.
- Poggi L., Ducart D.F. 2017. Análisis espectral de la alteración hidrotermal asociada al depósito de Au-Cu Paraíba, Mato Grosso, Brasil. XXXV Curso Latinoamericano de Metalogenia 2017. Poster session.

- Poggi L., Ducart D.F, Mesquita M. J., Moreira I. C. 2018. Mineralogical Characterization of the Paraíba Deposit (MT) Through Spectral Technologies. VIII Simposio Brasileiro de Exploração Mineral 2018. Poster session.
- Powell R., Will T.M., Phillips, G.N. 1991. Metamorphism in Archean greenstone belts: Calculated fluid compositions and implications for gold mineralization. *Journal of Metamorphic Geology*. v. 9, p. 141–150.
- Prochaska W., Bechtel A., Klotzli K. 1992. Phyllonite Formation and Alteration of Gneisses in Shear Zones (Gleinalmkristallin, Eastern Alps/Austria)\*. *Mineralogy and Petrology* 45:195-216.
- Renato Vieira Passos. Caracterização da Geometria de Zonas de Alteração Hidrotermal - Estudo de Caso no Depósito Aurífero de Brumal, Quadrilátero Ferrífero, Minas Gerais. 1999. Dissertação (Mestrado em Geociências) - Universidade Estadual de Campinas, Coordenação de Aperfeiçoamento de Pessoal de Nível Superior. Orientador: Carlos Roberto de Souza Filho.
- Reyes A.G. 1990. Petrology of Philippine geothermal system and the application of alteration mineralogy to their assessment. *Journal of Volcanology and Geothermal Research* 43: 279-304.
- Ridley J.R., Diamond L.W. 2000. Fluid chemistry of orogenic lode-gold deposits and implications for genetic models: *Reviews in Economic Geology*, v. 13, p. 141–162.
- Roache T.J., Walshe J.L., Huntington J.F., Quigley M.A., Yang K., Bil B.W., Blake K.L., Hyvärinen T. 2011. Epidote-clinzoisite as hyperspectral tool in exploration for Archean gold. *Australian Journal of Earth Sciences*, v. 58, p. 813–822.
- Rodrigues R.M. 2012. Caracterização geológica e metalogenética do Depósito X1 – Província Aurífera de Alta Floresta, Região de Matupá (MT). Dissertação de Mestrado, Instituto de Geociências, Universidade Estadual de Campinas, 70p.
- Sander B. 1911. ijber Zusammenhsnge zwischen Teilbewegungen und Gefüge in Gesteinen. *Tschermaks mineralog. petrog. Mitt.* 30,281-314.

- Santos A.C. 2011. Petrografia e isótopos de chumbo e enxofre de depósitos auríferos da Província Alta Floresta (MT): Implicações Metalogenéticas. Instituto de Geociências, Universidade do Estado do Rio de Janeiro, Trabalho de Conclusão de Curso, 175p.
- Santos J.O.S. 2003. Geotectônica dos escudos das Guianas and Brasil-Central. In: BIZZI, L. A. et al. (Eds). Geologia, Tectônica e Recursos Minerais do Brasil. CPRM: Brasília, 2003. p.169-226.
- Santos J.O.S. 2000. Os terrenos Paleoproterozóicos da Província do Tapajós e as mineralizações de ouro associadas. Tese de Doutorado, Universidade Federal do Rio Grande do Sul, v.1, 208 p.
- Santos J.O.S., Hartmann L.A., Faria M.S.G., Riker S.R., Souza M.M., Almeida M.E., McNaughton N.J. 2006. Acompartimentação do Cráton Amazonas em províncias: avanços ocorridos no período 2000-2006. In: SBG-NO, Simp. Geol. Amaz., 9, Belém, CD-Rom.
- Santos J.O.S., Groves D.I., Hartmann A., Moura M.A., McNaughton N.J. 2001. Gold deposits of the Tapajós and Alta Floresta domains, Tapajós-Parima orogenic belt, Amazon Craton, Brazil. *Mineralium Deposita*, 36:278-299.
- Santos J.O.S., Hartmann L.A., Gaudette H.E., Groves D.I., McNaughton N.J., Fletcher I.R. 2000. New understanding of the Amazon Craton provinces, based on field work and radiogenic isotope data. *Gondwana Research*, 3(4):453-486.
- Santos J.O.S., Silva L.C., Faria M.S.G., Macambira M. 1997. Pb-Pb single crystal evaporation isotopic study of the post-tectonic, sub-alkaline, A-type moderna granite (Mapuera Intrusive Granite), State of Roraima, northern Brazil. In: International Symposium on granites and associated mineralizations (ISGAM), 2, Salvador, Bahia, Extended abstracts and program, p. 273-275.
- Scott K.M., and Yang K. 1997. Spectral reflectance studies of white micas: AMIRA P435. CSIRO Investigation Report 439R.
- Seedofortt E., Dilles J.H., Proffett Jr J.M., Einaudi M.T., Zurcher L., Stavast W.J.A., Johnson D.A., Barton M.D. 2005. Porphyry deposits: characteristics and origin of hypogene features. *Economic Geology* 110tg Anniversary volume, p. 251-298.

- Sibson R.H. 1977. Fault rocks and fault mechanisms. *J. geo. Soc.Lond.* 133,191-213.
- Sillitoe R.H. 2010. Porphyry copper systems. *Economic Geology*, v. 105, p. 3–41.
- Sillitoe R.H. 1991. Intrusion-related gold deposits. In: Foster R.P. (ed.) *Metallurgy and exploration of gold*. Ed.Blackie, London, pp. 164-209.
- Sillitoe R.H., Thompson J.F.H. 1998. Intrusion-related vein gold deposits: Types, tectono-magmatic settings, and difficulties of distinction from orogenic gold deposits: *Resource Geology*, v. 48, p. 237–250.
- Silva F.R. 2014. Geoquímica e geocronologia U-Pb (SHRIMP) de granitos da região de Peixoto deAzevedo – Província Aurífera de Alta Floresta – MT. Dissertação de Mestrado, Universidade Federal de Mato Grosso, Cuiabá, Brasil, 82p.
- Silva M.G., Abram M.B. 2008. *Projeto metalogenia da Província Aurífera Juruena-Teles Pires, Mato Grosso*. Goiânia, Serviço Geológico Brasileiro, CPRM, 212p.
- Souza Filho C. R.; Passos R. V. Spectro-Mineral Mapping Using Field Spectroscopy and the Geometry Of Hydrothermal Alteration Zones Associated with Mesothermal Gold Mineralization: A Case Study in the Brumal Deposit, Quadrilátero Ferrífero, Brazil. In: *ERIM -13th International Conference on Applied Geologic Remote Sensing, 1999, Vancouver. Proceedings of the 13th International Conference on Applied Geologic Remote Sensing (ERIM)*. Michigan: Environmental Research Institute of Michigan, 1999. v. 1. p. 73-80.
- Souza J.P., Frasca A.A.S., Oliveira C.C. 2005. *Geologia e Recursos Minerais da Província Mineral de Alta Floresta. Relatório Integrado*. Brasília, Serviço Geológico Brasileiro, CPRM, 164p.
- Tamizel I., Mehmet A., Emel A.Y., Cem Y. 2014. Mineral chemistry and thermobarometry of Eocene monzogabbroic stocks from the Bafra (Samsun) area in Turkey: implications for disequilibrium crystallization and emplacement conditions. *International Geology Review*, July 56(10):1226-1245.
- Tappert M. C., Rivard B., Giles D., Tappert R., Mauger A.J. 2013. The mineral chemistry, near-infrared, and mid-infrared reflectance spectroscopy of phengite from the Olympic Dam IOCG deposit, South Australia. *Ore Geology Reviews* 53:26-38.

- Tappert M., Rivard B., Giles D. Tappert, R. Mauger, A. 2011. Automated drill core logging using visible and near-infrared reflectance spectroscopy: a case study from the Olympic Dam IOCG deposit, South Australia. *Econ. Geol.* 106, 289–296, <http://dx.doi.org/10.2113/econgeo.106.2.289>.
- Tassinari C.C.G. and Macambira M.J.B. 1999. Geochronological Provinces of the Amazonian Craton. *Episodes*, 22(3):174-182.
- Thompson J.H.F., Newberry R.J. 2000. Gold deposits related to reduced granitic intrusions: *Reviews in Economic Geology*, v. 13, p. 377–400.
- Travers S.J. and Wilson C.J.L., 2015. Reflectance spectroscopy and alteration assemblages at the Leven Star gold deposit, Victoria, Australia. *Australian Journal of Earth Sciences*, 62(7):873-882.
- Trevisan V.G. 2015. Estudo comparativo entre mineralizações filonares de Au ± Cu e Au + metais de base do setor leste da Província de Alta Floresta (MT), Cráton Amazônico (Master thesis), Instituto de Geociências, Universidade Estadual de Campinas, 129 p.
- Trevisan V.G. 2012a. Regime de fluidos em depósitos de Au-(Cu) associados a intrusões graníticas da Província de Alta Floresta (MT). Instituto de Geociências, Universidade Estadual de Campinas; Relatório PIBIC/CNPq; Relatório Final de Atividades, 30p.
- Trevisan V.G. 2012b. Metalogênese do ouro no Granito Novo Mundo, setor leste da Província Aurífera de Alta Floresta (MT), Cráton Amazônico: alteração hidrotermal e petrografia do minério. Trabalho de Conclusão de Curso, Instituto de Geociências, Universidade Estadual de Campinas, 110p.
- Velde B., 1985. Possible chemical control illite/smectite composition during diagenesis. *Mineral Magazine* 49, 387–391.
- Velde B. 1965. Phengite micas: synthesis, stability and natural occurrences. *American Journal of Science*, v.263,p 886-913.
- Wiewiora A., Weiss, Z. 1990. Crystallochemical classifications of phyllosilicates based on the unified system of projection of chemical composition: II The chlorite group. *Clay Miner.*, 25, 83–92.

Zang W., Fyfe W. S. 1995. Chloritization of the hydrothermally altered bedrocks at the Igarapé Bahia gold deposit, Carajás, Brazil. Mineral Deposit, ATAS, p.30, 30-38. Berlin.

# APPENDIX 1: White mica electron microprobe chemical data

Lithotype	Breccia												Tonalite	
Thin sample	BH041-012												BH059-009	
White mica group	White mica 4												White mica 3	
Analysis n°	Ms-1	Ms-2	Ms-3	Ms-4	Ms-5	Ms-6	Ms-7	Ms-8	Ms-9	Ms-10	Ms-11	Ms-12	Ms-13	Ms-14
SiO <sub>2</sub>	47.45	47.80	45.35	46.66	47.14	47.51	48.09	49.80	47.21	46.92	47.56	48.58	46.07	46.22
TiO <sub>2</sub>	0.25	0.38	0.32	0.40	0.49	0.49	0.38	0.51	0.52	0.40	0.28	0.00	0.61	0.54
Al <sub>2</sub> O <sub>3</sub>	30.95	28.25	26.71	28.68	29.12	30.37	31.13	30.81	29.51	27.80	30.93	30.24	28.71	29.37
Cr <sub>2</sub> O <sub>3</sub>	0.00	0.01	0.04	0.05	0.25	0.09	0.09	0.02	0.03	0.00	0.00	0.00	0.04	0.04
Fe <sub>2</sub> O <sub>3</sub>	2.46	3.41	3.85	3.62	3.55	2.72	2.76	2.38	2.65	3.17	2.53	3.02	4.99	4.53
FeO	0.00	0.00	0.00	0.00	0.00	0.00	0.00	0.00	0.00	0.00	0.00	0.00	0.00	0.00
MnO	0.02	0.07	0.13	0.11	0.07	0.04	0.07	0.07	0.06	0.07	0.04	0.08	0.15	0.12
MgO	2.43	3.88	4.36	4.01	2.51	2.61	2.38	3.20	3.42	4.40	2.42	2.47	2.33	2.09
CaO	0.00	0.00	0.00	0.00	0.00	0.00	0.00	0.00	0.00	0.00	0.00	0.00	0.00	0.00
Na <sub>2</sub> O	0.25	0.25	0.17	0.21	0.16	0.18	0.26	0.28	0.22	0.23	0.25	0.21	0.18	0.17
K <sub>2</sub> O	10.37	10.58	9.91	10.39	10.44	10.55	10.65	10.55	10.61	10.50	10.49	10.69	10.50	10.41
Totals	94.18	94.63	90.84	94.13	93.73	94.56	95.81	97.62	94.23	93.49	94.50	95.29	93.58	93.49

## based on 11O

Si	3.20	3.23	3.20	3.17	3.21	3.20	3.19	3.23	3.20	3.21	3.20	3.24	3.17	3.17
Ti	0.01	0.02	0.02	0.02	0.03	0.03	0.02	0.03	0.03	0.02	0.01	0.00	0.03	0.03
Al IV	0.80	0.77	0.80	0.83	0.79	0.80	0.81	0.77	0.81	0.79	0.80	0.76	0.83	0.83
Cr	0.00	0.00	0.00	0.00	0.01	0.01	0.01	0.00	0.00	0.00	0.00	0.00	0.00	0.00
Al VI	1.66	1.48	1.42	1.47	1.55	1.61	1.63	1.59	1.55	1.45	1.65	1.62	1.50	1.55
Fe <sub>3</sub>	0.13	0.17	0.20	0.19	0.18	0.14	0.14	0.12	0.14	0.16	0.13	0.15	0.26	0.23
Fe <sub>2</sub>	0.00	0.00	0.00	0.00	0.00	0.00	0.00	0.00	0.00	0.00	0.00	0.00	0.00	0.00
Mn	0.00	0.00	0.01	0.01	0.00	0.00	0.00	0.00	0.00	0.00	0.00	0.01	0.01	0.01
Mg	0.24	0.39	0.46	0.41	0.26	0.26	0.24	0.31	0.35	0.45	0.24	0.25	0.24	0.21
Ca	0.00	0.00	0.00	0.00	0.00	0.00	0.00	0.00	0.00	0.00	0.00	0.00	0.00	0.00
Na	0.03	0.03	0.02	0.03	0.02	0.02	0.03	0.04	0.03	0.03	0.03	0.03	0.02	0.02
K	0.89	0.91	0.89	0.90	0.91	0.91	0.90	0.87	0.92	0.92	0.90	0.91	0.92	0.91
Sum	6.96	7.01	7.03	7.03	6.96	6.97	6.97	6.96	7.01	7.04	6.97	6.96	6.98	6.96

Geom. Mean Si+(Fe + Mg)	3.73					3.62				3.67			3.62	
Geom. Mean Al(t)	2.31					2.39				2.36			2.36	
Wavelength (nm)	2221					2213				2217			2215	



Phyllonite							Tonalite							
BH020-019							BH041-003							
White mica 2							White mica 3				White mica 5			
Ms-30	Ms-31	Ms-32	Ms-33	Ms-34	Ms-35	Ms-36	Ms-37	Ms-38	Ms-39	Ms-40	Ms-41	Ms-42	Ms-43	Ms-44
46.95	48.26	47.97	47.93	48.19	48.00	48.72	45.85	45.54	44.36	46.17	45.22	45.90	45.96	45.36
0.23	0.04	0.03	0.21	0.15	0.26	0.22	0.52	0.37	0.77	0.93	0.48	0.45	0.43	0.45
28.82	29.68	28.61	27.86	28.38	27.75	28.03	29.45	29.55	29.35	29.79	29.48	29.68	29.00	29.42
0.03	0.00	0.00	0.01	0.02	0.06	0.06	0.00	0.00	0.00	0.00	0.00	0.00	0.00	0.00
3.54	2.60	3.22	2.21	2.56	3.13	2.05	4.75	5.06	4.84	4.78	5.07	3.89	4.44	5.18
0.00	0.00	0.00	0.00	0.00	0.00	0.00	0.00	0.00	0.00	0.00	0.00	0.00	0.00	0.00
0.09	0.04	0.08	0.04	0.05	0.08	0.04	0.04	0.05	0.03	0.05	0.06	0.05	0.03	0.05
2.61	2.71	2.92	4.68	3.52	3.37	3.62	2.33	2.43	2.29	2.16	2.54	2.59	2.62	2.78
0.00	0.00	0.00	0.00	0.00	0.00	0.00	0.00	0.00	0.00	0.00	0.00	0.00	0.00	0.00
0.10	0.15	0.10	0.14	0.09	0.08	0.11	0.20	0.20	0.22	0.24	0.20	0.22	0.19	0.25
10.35	10.16	10.26	10.51	10.30	10.29	10.46	10.36	10.32	9.81	10.26	10.25	10.49	10.19	10.34
92.72	93.64	93.19	93.59	93.26	93.02	93.31	93.50	93.52	91.67	94.38	93.30	93.27	92.86	93.83
based on 110														
3.23	3.26	3.27	3.26	3.28	3.28	3.31	3.15	3.13	3.11	3.14	3.12	3.15	3.17	3.11
0.01	0.00	0.00	0.01	0.01	0.01	0.01	0.03	0.02	0.04	0.05	0.03	0.02	0.02	0.02
0.77	0.74	0.73	0.74	0.72	0.72	0.69	0.85	0.87	0.90	0.86	0.88	0.85	0.83	0.89
0.00	0.00	0.00	0.00	0.00	0.00	0.00	0.00	0.00	0.00	0.00	0.00	0.00	0.00	0.00
1.57	1.63	1.57	1.49	1.56	1.52	1.56	1.53	1.52	1.53	1.53	1.51	1.56	1.53	1.49
0.18	0.13	0.17	0.11	0.13	0.16	0.11	0.25	0.26	0.26	0.24	0.26	0.20	0.23	0.27
0.00	0.00	0.00	0.00	0.00	0.00	0.00	0.00	0.00	0.00	0.00	0.00	0.00	0.00	0.00
0.01	0.00	0.01	0.00	0.00	0.01	0.00	0.00	0.00	0.00	0.00	0.00	0.00	0.00	0.00
0.27	0.27	0.30	0.47	0.36	0.34	0.37	0.24	0.25	0.24	0.22	0.26	0.27	0.27	0.28
0.00	0.00	0.00	0.00	0.00	0.00	0.00	0.00	0.00	0.00	0.00	0.00	0.00	0.00	0.00
0.01	0.02	0.01	0.02	0.01	0.01	0.01	0.03	0.03	0.03	0.03	0.03	0.03	0.03	0.03
0.91	0.88	0.89	0.91	0.89	0.90	0.91	0.91	0.91	0.88	0.89	0.90	0.92	0.90	0.91
6.96	6.94	6.95	7.02	6.96	6.96	6.96	6.98	6.99	6.97	6.96	6.99	7.00	6.98	7.01
3.69			3.80				3.62				3.65			
2.33			2.25				2.40				2.38			
2219			2225				2212				2213			

Tonalite					
BH041-003					
White mica 3					
Ms-45	Ms-46	Ms-47	Ms-48	Ms-49	Ms-50
44.67	46.58	45.58	46.13	44.14	45.78
0.91	1.35	0.10	0.09	0.76	0.35
29.71	30.13	29.68	30.60	29.24	29.54
0.00	0.00	0.00	0.00	0.03	0.00
4.68	4.40	4.42	4.23	4.89	4.85
0.00	0.00	0.00	0.00	0.00	0.00
0.04	0.04	0.03	0.03	0.07	0.03
2.11	1.87	2.43	1.89	2.38	2.51
0.00	0.00	0.00	0.00	0.00	0.00
0.24	0.23	0.20	0.23	0.18	0.23
10.10	10.18	10.22	10.32	10.27	10.14
92.46	94.78	92.66	93.52	91.96	93.43
based on 110					
3.10	3.14	3.15	3.15	3.09	3.14
0.05	0.07	0.01	0.01	0.04	0.02
0.90	0.86	0.85	0.85	0.91	0.86
0.00	0.00	0.00	0.00	0.00	0.00
1.54	1.54	1.57	1.62	1.51	1.53
0.25	0.22	0.23	0.22	0.26	0.25
0.00	0.00	0.00	0.00	0.00	0.00
0.00	0.00	0.00	0.00	0.00	0.00
0.22	0.19	0.25	0.19	0.25	0.26
0.00	0.00	0.00	0.00	0.00	0.00
0.03	0.03	0.03	0.03	0.02	0.03
0.90	0.88	0.90	0.90	0.92	0.89
6.98	6.93	6.99	6.97	7.00	6.98
3.58					
2.43					
2209					

**APPENDIX 2: Chlorite electron microprobe chemical data.**

Lithotype	Breccia								Phyllonite					
Chlorite group	Chlorite 3								Chlorite 3					
Thin sample	BH041-012								BH059-041					
Analysis n°	Chl-1	Chl-2	Chl-3	Chl-4	Chl-5	Chl-6	Chl-7	Chl-8	Chl-9	Chl-10	Chl-11	Chl-12	Chl-13	Chl-14
SiO <sub>2</sub>	28.09	29.11	29.22	28.87	27.79	28.86	27.91	29.14	28.28	28.29	28.60	28.09	27.56	27.76
TiO <sub>2</sub>	0.00	0.00	0.00	0.00	0.02	0.00	0.00	0.01	0.01	0.01	0.00	0.01	0.00	0.00
Al <sub>2</sub> O <sub>3</sub>	17.46	18.38	17.93	17.04	18.19	17.17	16.94	17.94	17.90	18.22	18.45	18.47	19.22	19.85
Cr <sub>2</sub> O <sub>3</sub>	0.00	0.00	0.00	0.00	0.00	0.00	0.00	0.00	0.00	0.00	0.00	0.00	0.00	0.00
Fe <sub>2</sub> O <sub>3</sub>	0.00	0.00	0.00	0.00	0.00	0.00	0.00	0.00	0.00	0.00	0.00	0.00	0.00	0.00
FeO	16.40	17.18	17.54	16.37	16.64	15.60	16.36	16.28	15.48	15.46	15.65	15.88	16.65	16.74
MnO	0.75	0.91	0.77	0.83	1.33	0.78	0.81	0.91	0.49	0.47	0.44	0.53	0.55	0.55
MgO	20.97	21.15	21.73	21.86	21.10	21.97	20.82	22.03	21.86	22.08	22.27	22.05	21.31	21.43
CaO	0.05	0.03	0.04	0.00	0.01	0.02	0.04	0.00	0.04	0.01	0.03	0.01	0.01	0.00
Na <sub>2</sub> O	0.10	0.10	0.03	0.07	0.05	0.09	0.09	0.08	0.02	0.03	0.03	0.01	0.02	0.01
K <sub>2</sub> O	0.12	0.10	0.05	0.09	0.08	0.09	0.10	0.08	0.05	0.03	0.06	0.04	0.04	0.01
Totals	83.94	86.96	87.31	85.13	85.21	84.58	83.07	86.47	84.13	84.60	85.53	85.09	85.36	86.35

based on 14O

Si	2.96	2.96	2.97	3.00	2.90	3.00	2.97	2.97	2.95	2.93	2.93	2.90	2.85	2.84
Ti	0.00	0.00	0.00	0.00	0.00	0.00	0.00	0.00	0.00	0.00	0.00	0.00	0.00	0.00
Al IV	1.04	1.04	1.04	1.01	1.11	1.00	1.03	1.03	1.05	1.07	1.07	1.10	1.15	1.16
Cr	0.00	0.00	0.00	0.00	0.00	0.00	0.00	0.00	0.00	0.00	0.00	0.00	0.00	0.00
Al VI	1.13	1.17	1.11	1.08	1.13	1.10	1.10	1.13	1.15	1.16	1.16	1.15	1.20	1.23
Fe <sub>3</sub>	0.00	0.00	0.00	0.00	0.00	0.00	0.00	0.00	0.00	0.00	0.00	0.00	0.00	0.00
Fe <sub>2</sub>	1.45	1.46	1.49	1.42	1.45	1.36	1.46	1.39	1.35	1.34	1.34	1.37	1.44	1.43
Mn	0.07	0.08	0.07	0.07	0.12	0.07	0.07	0.08	0.04	0.04	0.04	0.05	0.05	0.05
Mg	3.29	3.21	3.29	3.38	3.28	3.40	3.31	3.35	3.40	3.41	3.40	3.40	3.29	3.26
Ca	0.01	0.00	0.00	0.00	0.00	0.00	0.01	0.00	0.00	0.00	0.00	0.00	0.00	0.00
Na	0.02	0.02	0.01	0.01	0.01	0.02	0.02	0.02	0.00	0.01	0.01	0.00	0.00	0.00
K	0.02	0.01	0.01	0.01	0.01	0.01	0.01	0.01	0.01	0.00	0.01	0.01	0.01	0.00
Sum	9.98	9.95	9.97	9.98	10.00	9.96	9.98	9.97	9.96	9.96	9.96	9.98	9.98	9.97

#Fe	0.30	0.31	0.31	0.30	0.31	0.28	0.31	0.29	0.28	0.28	0.28	0.29	0.30	0.30
#Mg	0.70	0.69	0.69	0.70	0.69	0.72	0.69	0.71	0.72	0.72	0.72	0.71	0.70	0.70
Geometric mean #Fe	0.30								0.29					
Geometric mean #Mg	0.70								0.71					
Wavelength position	2336								2334					

Phyllonite								Tonalite				Phyllonite			
Chlorite 3								Chlorite 2				Chlorite 1			
BH059-041			BH059-046					BH041-003				BH020-027			
Chl-15	Chl-16	Chl-17	Chl-18	Chl-19	Chl-20	Chl-21	Chl-22	Chl-23	Chl-24	Chl-25	Chl-26	Chl-27	Chl-28	Chl-29	Chl-30
28.98	28.97	28.98	27.77	28.63	28.87	28.75	28.50	25.61	28.47	28.27	26.14	26.84	26.26	26.48	26.54
0.01	0.00	0.00	0.00	0.00	0.02	0.00	0.00	0.12	0.09	0.04	0.07	0.03	0.04	0.02	0.02
18.55	17.59	18.18	18.68	17.93	17.93	17.70	17.49	20.71	20.62	17.49	19.27	20.17	20.43	20.65	20.37
0.00	0.00	0.00	0.00	0.00	0.00	0.00	0.00	0.00	0.00	0.00	0.00	0.00	0.00	0.00	0.00
0.00	0.00	0.00	0.00	0.00	0.00	0.00	0.00	0.00	0.00	0.00	0.00	0.00	0.00	0.00	0.00
15.60	15.63	15.87	18.21	18.07	17.29	16.82	17.24	20.47	18.65	19.47	19.76	16.32	15.70	16.57	15.51
0.54	0.45	0.51	0.56	0.54	0.55	0.46	0.54	0.60	0.48	0.51	0.56	1.15	1.08	1.13	0.55
22.41	22.83	22.88	19.90	21.06	21.06	21.47	21.02	17.44	18.94	19.07	17.98	20.48	20.87	20.19	20.83
0.06	0.03	0.04	0.02	0.01	0.03	0.02	0.00	0.08	0.00	0.00	0.06	0.04	0.02	0.00	0.01
0.03	0.04	0.02	0.04	0.02	0.05	0.04	0.02	0.02	0.06	0.03	0.02	0.03	0.02	0.05	0.04
0.05	0.08	0.07	0.14	0.04	0.10	0.06	0.04	0.05	1.25	0.40	0.15	0.03	0.03	0.04	0.04
86.23	85.62	86.55	85.32	86.30	85.90	85.32	84.85	85.10	88.56	85.28	84.01	85.09	84.45	85.13	83.91
based on 140															
2.94	2.97	2.94	2.90	2.95	2.97	2.97	2.97	2.72	2.88	2.98	2.81	2.79	2.75	2.76	2.78
0.00	0.00	0.00	0.00	0.00	0.00	0.00	0.00	0.01	0.01	0.00	0.01	0.00	0.00	0.00	0.00
1.06	1.03	1.06	1.10	1.05	1.03	1.03	1.03	1.28	1.13	1.02	1.19	1.21	1.26	1.24	1.22
0.00	0.00	0.00	0.00	0.00	0.00	0.00	0.00	0.00	0.00	0.00	0.00	0.00	0.00	0.00	0.00
1.17	1.09	1.11	1.20	1.12	1.15	1.13	1.13	1.32	1.33	1.15	1.24	1.26	1.26	1.29	1.29
0.00	0.00	0.00	0.00	0.00	0.00	0.00	0.00	0.00	0.00	0.00	0.00	0.00	0.00	0.00	0.00
1.33	1.34	1.35	1.59	1.56	1.49	1.46	1.50	1.82	1.58	1.72	1.77	1.42	1.37	1.44	1.36
0.05	0.04	0.04	0.05	0.05	0.05	0.04	0.05	0.05	0.04	0.05	0.05	0.10	0.10	0.10	0.05
3.39	3.49	3.46	3.10	3.23	3.23	3.31	3.27	2.76	2.85	2.99	2.88	3.17	3.25	3.13	3.25
0.01	0.00	0.00	0.00	0.00	0.00	0.00	0.00	0.01	0.00	0.00	0.01	0.00	0.00	0.00	0.00
0.01	0.01	0.00	0.01	0.00	0.01	0.01	0.00	0.00	0.01	0.01	0.00	0.01	0.00	0.01	0.01
0.01	0.01	0.01	0.02	0.01	0.01	0.01	0.01	0.01	0.16	0.05	0.02	0.00	0.00	0.01	0.01
9.95	9.98	9.98	9.96	9.97	9.95	9.96	9.96	9.98	9.98	9.96	9.98	9.98	10.00	9.98	9.97
0.28	0.28	0.28	0.34	0.33	0.32	0.31	0.32	0.40	0.36	0.36	0.38	0.31	0.30	0.32	0.29
0.72	0.72	0.72	0.66	0.67	0.68	0.69	0.68	0.60	0.64	0.64	0.62	0.69	0.70	0.68	0.71
			0.32					0.38		0.37		0.30			
			0.68					0.62		0.63		0.70			
			2340					2345		2344		2338			

Phyllonite							
Chlorite 1							
BH020-027							
Chl-31	Chl-32	Chl-33	Chl-34	Chl-35	Chl-36	Chl-37	Chl-38
26.34	26.81	26.78	26.24	26.62	26.42	26.29	26.49
0.02	0.05	0.03	0.07	0.05	0.06	0.02	0.06
20.48	20.09	20.83	20.64	20.63	20.88	20.67	20.46
0.00	0.00	0.00	0.00	0.00	0.00	0.00	0.00
0.00	0.00	0.00	0.00	0.00	0.00	0.00	0.00
15.40	16.70	16.68	16.75	16.14	16.47	16.86	16.50
1.03	1.28	0.94	1.01	0.54	0.69	1.31	0.97
20.20	20.14	20.43	20.01	20.53	20.74	19.74	19.88
0.00	0.04	0.01	0.00	0.03	0.00	0.00	0.01
0.02	0.00	0.02	0.03	0.02	0.01	0.01	0.02
0.03	0.09	0.03	0.05	0.03	0.01	0.02	0.08
83.52	85.20	85.75	84.80	84.59	85.28	84.92	84.47
based on 140							
2.78	2.79	2.76	2.75	2.77	2.74	2.75	2.78
0.00	0.00	0.00	0.01	0.00	0.01	0.00	0.01
1.22	1.21	1.24	1.26	1.23	1.26	1.25	1.22
0.00	0.00	0.00	0.00	0.00	0.00	0.00	0.00
1.32	1.26	1.30	1.29	1.31	1.29	1.30	1.30
0.00	0.00	0.00	0.00	0.00	0.00	0.00	0.00
1.36	1.46	1.44	1.47	1.41	1.43	1.48	1.45
0.09	0.11	0.08	0.09	0.05	0.06	0.12	0.09
3.17	3.13	3.14	3.12	3.19	3.20	3.08	3.11
0.00	0.00	0.00	0.00	0.00	0.00	0.00	0.00
0.00	0.00	0.00	0.01	0.00	0.00	0.00	0.00
0.00	0.01	0.00	0.01	0.00	0.00	0.00	0.01
9.95	9.98	9.97	9.98	9.96	9.99	9.98	9.96
0.30	0.32	0.31	0.32	0.31	0.31	0.32	0.32
0.70	0.68	0.69	0.68	0.69	0.69	0.68	0.68
	0.32						
	0.68						
	2339						

**APPENDIX 3: Biotite electron microprobe chemical data.**

Lithotype	Phyllonite															
Thin sample	BH041-016															
Analysis n°	Bt-1	Bt-2	Bt-3	Bt-4	Bt-5	Bt-6	Bt-7	Bt-8	Bt-9	Bt-10	Bt-11	Bt-12	Bt-13	Bt-14	Bt-15	Bt-16
SiO <sub>2</sub>	42.69	41.84	40.21	40.73	40.92	43.91	43.31	45.18	40.47	44.56	40.67	41.05	39.85	40.22	39.43	41.01
TiO <sub>2</sub>	0.06	0.03	0.03	0.04	0.03	0.00	0.05	0.17	0.48	0.16	0.43	0.34	0.40	0.36	0.33	0.48
Al <sub>2</sub> O <sub>3</sub>	13.37	13.67	12.51	12.66	12.54	10.80	11.03	9.94	13.23	10.34	13.16	13.79	13.52	12.97	13.53	12.54
Cr <sub>2</sub> O <sub>3</sub>	0.00	0.00	0.00	0.00	0.00	0.00	0.00	0.00	0.00	0.00	0.00	0.00	0.00	0.00	0.00	0.00
Fe <sub>2</sub> O <sub>3</sub>	1.11	1.10	1.12	1.13	1.08	0.97	0.94	0.81	1.26	0.69	1.23	1.26	1.32	1.26	1.34	1.23
FeO	5.65	5.58	5.69	5.74	5.50	4.94	4.79	4.58	6.41	4.81	6.26	6.43	6.74	6.40	6.85	6.25
MnO	0.45	0.42	0.45	0.42	0.43	0.37	0.35	0.31	0.45	0.30	0.45	0.44	0.46	0.45	0.52	0.44
MgO	23.48	22.17	21.71	21.97	22.07	23.21	22.96	23.07	20.62	22.81	20.76	20.83	20.36	21.03	20.15	21.40
CaO	0.00	0.00	0.00	0.00	0.00	0.00	0.00	0.00	0.00	0.00	0.00	0.00	0.00	0.00	0.00	0.00
Na <sub>2</sub> O	0.07	0.08	0.06	0.05	0.05	0.03	0.05	0.05	0.05	0.06	0.07	0.06	0.05	0.06	0.05	0.04
K <sub>2</sub> O	9.27	9.98	9.81	9.78	9.81	8.80	9.13	8.76	9.66	9.01	9.65	9.36	9.95	9.82	9.97	9.80
Totals	96.15	94.87	91.58	92.51	92.43	93.03	92.61	92.87	92.63	92.74	92.67	93.57	92.65	92.57	92.17	93.18

**based on 110**

Si	3.00	3.00	3.00	3.00	3.01	3.16	3.14	3.24	2.99	3.21	2.99	2.99	2.95	2.98	2.94	3.01
Ti	0.00	0.00	0.00	0.00	0.00	0.00	0.00	0.01	0.03	0.01	0.02	0.02	0.02	0.02	0.02	0.03
Al IV	1.00	1.01	1.00	1.00	0.99	0.84	0.86	0.76	1.02	0.79	1.01	1.02	1.05	1.03	1.06	0.99
Cr	0.00	0.00	0.00	0.00	0.00	0.00	0.00	0.00	0.00	0.00	0.00	0.00	0.00	0.00	0.00	0.00
Al VI	0.11	0.15	0.10	0.10	0.10	0.08	0.08	0.09	0.14	0.09	0.14	0.17	0.13	0.11	0.13	0.09
Fe <sub>3</sub>	0.06	0.06	0.06	0.06	0.06	0.05	0.05	0.04	0.07	0.04	0.07	0.07	0.07	0.07	0.08	0.07
Fe <sub>2</sub>	0.33	0.33	0.35	0.35	0.34	0.30	0.29	0.28	0.40	0.29	0.39	0.39	0.42	0.40	0.43	0.38
Mn	0.03	0.03	0.03	0.03	0.03	0.02	0.02	0.02	0.03	0.02	0.03	0.03	0.03	0.03	0.03	0.03
Mg	2.46	2.37	2.41	2.41	2.42	2.49	2.48	2.47	2.27	2.45	2.28	2.26	2.25	2.32	2.24	2.34
Ca	0.00	0.00	0.00	0.00	0.00	0.00	0.00	0.00	0.00	0.00	0.00	0.00	0.00	0.00	0.00	0.00
Na	0.01	0.01	0.01	0.01	0.01	0.00	0.01	0.01	0.01	0.01	0.01	0.01	0.01	0.01	0.01	0.01
K	0.83	0.91	0.93	0.92	0.92	0.81	0.85	0.80	0.91	0.83	0.91	0.87	0.94	0.93	0.95	0.92
Sum	7.83	7.86	7.89	7.88	7.88	7.76	7.79	7.71	7.84	7.74	7.84	7.81	7.87	7.87	7.89	7.85

Phyllonite				Phyllonite							Phyllonite	Phyllonite				
BH041-016				BH059-041							BH059-046	BH020-027				
Bt-17	Bt-18	Bt-19	Bt-20	Bt-21	Bt-22	Bt-23	Bt-24	Bt-25	Bt-26	Bt-27	Bt-28	Bt-29	Bt-30	Bt-31	Bt-32	Bt-33
40.22	43.83	45.41	40.17	40.00	40.70	40.28	39.29	40.95	39.46	39.61	38.43	36.98	37.37	36.93	37.43	37.25
0.58	0.27	0.14	0.62	0.15	0.07	0.08	0.26	0.29	0.20	0.13	0.15	0.80	0.66	0.90	0.82	1.90
13.10	10.08	9.49	13.31	13.00	13.24	12.94	13.68	14.15	13.45	13.01	13.96	15.85	15.50	15.85	15.74	16.10
0.00	0.00	0.00	0.00	0.00	0.00	0.00	0.00	0.00	0.00	0.00	0.00	0.00	0.00	0.00	0.00	0.00
1.19	0.90	0.66	1.17	1.78	1.75	1.74	1.88	1.87	1.83	1.83	2.14	1.57	2.04	2.18	1.98	0.00
6.04	4.58	4.33	5.98	9.10	8.91	8.87	9.57	9.55	9.33	9.35	10.92	11.26	10.41	11.09	10.73	13.33
0.46	0.34	0.33	0.43	0.25	0.27	0.23	0.27	0.27	0.27	0.22	0.30	0.85	0.81	0.91	0.83	0.83
21.16	22.61	23.28	20.73	18.91	19.64	19.51	18.47	19.28	18.52	19.16	16.73	15.34	15.96	15.30	15.69	14.14
0.00	0.00	0.00	0.00	0.00	0.00	0.00	0.00	0.00	0.00	0.00	0.00	0.00	0.00	0.00	0.00	0.00
0.11	0.06	0.03	0.07	0.08	0.06	0.06	0.06	0.06	0.08	0.06	0.09	0.06	0.06	0.05	0.04	0.04
9.96	8.57	8.68	9.82	9.36	9.31	9.32	9.55	9.66	9.44	9.36	9.38	9.67	9.43	9.26	9.49	9.50
92.82	91.24	92.36	92.30	92.63	93.95	93.02	93.03	96.09	92.58	92.73	92.10	92.38	92.24	92.47	92.75	93.09

based on 110

2.96	3.21	3.27	2.97	2.99	2.99	2.99	2.94	2.95	2.96	2.96	2.92	2.82	2.84	2.81	2.83	2.83
0.03	0.02	0.01	0.03	0.01	0.00	0.00	0.02	0.02	0.01	0.01	0.01	0.05	0.04	0.05	0.05	0.11
1.04	0.79	0.73	1.03	1.01	1.01	1.01	1.06	1.05	1.04	1.04	1.08	1.18	1.16	1.19	1.17	1.17
0.00	0.00	0.00	0.00	0.00	0.00	0.00	0.00	0.00	0.00	0.00	0.00	0.00	0.00	0.00	0.00	0.00
0.10	0.08	0.08	0.13	0.13	0.13	0.12	0.14	0.15	0.15	0.11	0.18	0.25	0.23	0.23	0.24	0.27
0.07	0.05	0.04	0.07	0.10	0.10	0.10	0.11	0.10	0.10	0.10	0.12	0.09	0.12	0.13	0.11	0.00
0.37	0.28	0.26	0.37	0.57	0.55	0.55	0.60	0.58	0.59	0.59	0.70	0.72	0.66	0.71	0.68	0.85
0.03	0.02	0.02	0.03	0.02	0.02	0.01	0.02	0.02	0.02	0.01	0.02	0.06	0.05	0.06	0.05	0.05
2.32	2.47	2.50	2.29	2.11	2.15	2.16	2.06	2.07	2.07	2.14	1.90	1.74	1.81	1.74	1.77	1.60
0.00	0.00	0.00	0.00	0.00	0.00	0.00	0.00	0.00	0.00	0.00	0.00	0.00	0.00	0.00	0.00	0.00
0.02	0.01	0.00	0.01	0.01	0.01	0.01	0.01	0.01	0.01	0.01	0.01	0.01	0.01	0.01	0.01	0.01
0.94	0.80	0.80	0.93	0.89	0.87	0.88	0.91	0.89	0.90	0.89	0.91	0.94	0.92	0.90	0.92	0.92
7.88	7.72	7.70	7.85	7.83	7.83	7.84	7.85	7.83	7.84	7.86	7.84	7.85	7.83	7.82	7.82	7.81

Phyllonite			Tonalite	Phyllonite					Phyllonite
BH020-027			BH041-003	BH059-041					BH020-019
Bt-34	Bt-35	Bt-36	Bt-37	Bt-38	Bt-39	Bt-40	Bt-41	Bt-42	Bt-43
36.62	36.47	37.96	38.00	38.89	41.28	40.80	40.73	40.90	38.10
1.20	1.07	0.66	2.33	0.38	0.18	0.25	0.14	0.26	0.35
16.08	15.83	15.32	16.09	14.05	12.80	13.06	14.02	13.82	14.59
0.00	0.00	0.00	0.00	0.13	0.06	0.07	0.00	0.14	0.00
2.24	1.80	1.93	0.00	2.24	1.97	2.00	2.07	1.95	1.38
11.42	11.28	10.29	16.28	11.42	10.06	10.18	10.53	9.95	11.20
0.88	0.80	0.73	0.32	0.26	0.23	0.23	0.25	0.26	0.98
15.04	15.05	16.25	13.35	17.88	19.77	19.04	19.27	19.21	16.48
0.00	0.00	0.00	0.00	0.00	0.00	0.00	0.00	0.00	0.00
0.04	0.07	0.02	0.07	0.07	0.06	0.05	0.07	0.03	0.05
9.39	9.45	9.54	9.46	9.47	9.45	9.46	9.63	8.97	9.45
92.91	91.82	92.70	95.90	94.79	95.86	95.14	96.71	95.50	92.59

based on 110

2.78	2.80	2.87	2.83	2.88	2.99	2.98	2.93	2.96	2.89
0.07	0.06	0.04	0.13	0.02	0.01	0.01	0.01	0.01	0.02
1.22	1.20	1.14	1.17	1.12	1.01	1.02	1.07	1.04	1.11
0.00	0.00	0.00	0.00	0.01	0.00	0.00	0.00	0.01	0.00
0.22	0.23	0.23	0.24	0.11	0.08	0.11	0.12	0.14	0.20
0.13	0.10	0.11	0.00	0.13	0.11	0.11	0.11	0.11	0.08
0.73	0.73	0.65	1.01	0.71	0.61	0.62	0.63	0.60	0.71
0.06	0.05	0.05	0.02	0.02	0.01	0.01	0.02	0.02	0.06
1.70	1.72	1.83	1.48	1.98	2.13	2.07	2.07	2.07	1.86
0.00	0.00	0.00	0.00	0.00	0.00	0.00	0.00	0.00	0.00
0.01	0.01	0.00	0.01	0.01	0.01	0.01	0.01	0.00	0.01
0.91	0.93	0.92	0.90	0.90	0.87	0.88	0.89	0.83	0.92
7.82	7.84	7.82	7.79	7.87	7.84	7.83	7.86	7.79	7.86

**APPENDIX 4: Epidote electron microprobe chemical data.**

Lithotype	Tonalite		Breccia						Filonite	
Thin sample	DH041-L003		DH041-L012						DH059-046	
Alteration type	Propilitica		Epidotization						Epidotization	
Analysis n°	Ep-1	Ep-2	Ep-3	Ep-4	Ep-5	Ep-6	Ep-7	Ep-8	Ep-9	Ep-10
SiO2	37.13	37.42	37.14	37.43	36.54	36.97	37.32	36.87	37.81	37.03
TiO2	0.01	0.07	0.01	0.12	0.03	0.03	0	0.08	0.04	0
Al2O3	22.59	23.37	23.72	22.12	22.2	22.54	22.59	21.95	25.6	21.74
Cr2O3	0	0	0	0	0	0	0	0	0	0
Fe2O3	14.57	13.4	12.54	14.31	13.34	14.4	13.58	15.03	11.14	15.84
FeO	0	0	0	0	0	0	0	0	0	0
MnO	0.24	0.21	0.65	0.29	0.57	0.11	0.51	0.25	0.06	0.35
MgO	0.01	0.02	0.47	0.19	0.02	0.02	0	0.03	0	0.02
CaO	22.21	22.65	20.67	21.48	21.51	22.38	22.43	22.76	23.6	22.64
Na2O	0	0.02	0	0.01	0.02	0.01	0	0	0.01	0.01
K2O	0	0	0	0	0	0	0	0	0	0
Totals	96.76	97.16	95.2	95.95	94.23	96.46	96.43	96.97	98.26	97.63

based on 12.50

Si	3	3	3.019	3.041	3.024	2.997	3.022	2.987	2.975	2.987
Ti	0.001	0.004	0.001	0.007	0.002	0.002	0	0.005	0.002	0
Al	2.152	2.209	2.273	2.119	2.166	2.154	2.156	2.097	2.375	2.067
Cr	0	0	0	0	0	0	0	0	0	0
Fe3	0.886	0.809	0.767	0.875	0.831	0.878	0.827	0.916	0.66	0.961
Fe2	0	0	0	0	0	0	0	0	0	0
Mn	0.016	0.014	0.045	0.02	0.04	0.008	0.035	0.017	0.004	0.024
Mg	0.001	0.002	0.057	0.023	0.002	0.002	0	0.004	0	0.002
Ca	1.923	1.946	1.8	1.87	1.908	1.944	1.946	1.976	1.99	1.957
Na	0	0.003	0	0.002	0.003	0.002	0	0	0.002	0.002
K	0	0	0	0	0	0	0	0	0	0
Sum	7.98	7.99	7.96	7.96	7.98	7.99	7.99	8.00	8.01	8.00

Filonite	
DH059-046	
Epidotization	
Ep-11	Ep-12
37.41	37.09
0.02	0.04
24.19	22.59
0	0
12.22	14.83
0	0
0.14	0.32
0.07	0.02
23.08	22.55
0	0
0	0
97.13	97.44
based on 12.50	
2.99	2.984
0.001	0.002
2.28	2.142
0	0
0.735	0.898
0	0
0.009	0.022
0.008	0.002
1.977	1.944
0	0
0	0
8.00	8.00